Autonomous Aerobatic Maneuvering of Miniature Helicopters

by

Vladislav Gavrilets

Submitted to the Department of Aeronautics and Astronautics
in partial fulfillment of the requirements for the degree of

Doctor of Philosophy

at the

MASSACHUSETTS INSTITUTE OF TECHNOLOGY

May 2003

Author .....
Department of Aeronautics and Astronautics
May 2, 2003

Certified by .....
Eric Feron
Associate Professor of Aeronautics and Astronautics
Thesis Supervisor

Certified by .....
Munther Dahleh
Professor of Electrical Engineering
Thesis Supervisor

Certified by .....
David Vos
Chief Technology Officer, Athena Technologies
Thesis Supervisor

Certified by .....
Carlos Cesnik
Associate Professor of Aerospace Engineering, University of Michigan
Thesis Supervisor

Accepted by .....
Edward Greitzer
Slater Professor of Aeronautics and Astronautics
Chairman, Department Committee on Graduate Students

Autonomous Aerobatic Maneuvering of Miniature Helicopters

by

Vladislav Gavrilets

Submitted to the Department of Aeronautics and Astronautics
on May 2, 2003, in partial fulfillment of the
requirements for the degree of
Doctor of Philosophy

Abstract

In this thesis, I present an experimentally proven control methodology for the autonomous execution of aerobatic maneuvers with small-scale helicopters, and a low-order dynamic model which adequately describes a miniature helicopter in a wide range of flight conditions, including aerobatics. The control laws consist of steady-state trim trajectory controllers, used prior to, and upon exit from the maneuvers; and a maneuver execution logic inspired by human pilot strategies. In order to test the control laws, a miniature helicopter was outfitted with a custom digital avionics system, and a hardware-in-the-loop simulation was developed. The logic was tested with several aerobatic maneuvers and maneuver sequences, which demonstrated smooth maneuver entry, automatic recovery to a steady-state trim trajectory, and robustness of the trim-trajectory control system toward measurement and modeling errors. Based on these results, I further propose a simplified hybrid model for a helicopter under such closed loop control. The model can be utilized in the development of computationally tractable motion-planning algorithms for agile vehicles.

Thesis Supervisor: Eric Feron
Title: Associate Professor of Aeronautics and Astronautics

Thesis Supervisor: Munther Dahleh
Title: Professor of Electrical Engineering

Thesis Supervisor: David Vos
Title: Chief Technology Officer, Athena Technologies

Thesis Supervisor: Carlos Cesnik
Title: Associate Professor of Aerospace Engineering, University of Michigan

Acknowledgments

First of all, I would like to thank my advisors Eric Feron and David Vos for their constant support, and infinitely many insights, technical and beyond, they gave me over the years.

I am happy to credit Eric with the idea that started this thesis: to demonstrate that aerobatic maneuvers can be performed fully autonomously by an aerial robot, in a manner similar to the way human pilots perform them. Eric has been an incredibly enthusiastic supporter, and at the same time steered the course of the project with great wisdom. I have greatly enjoyed our many irreverent conversations; his house, full of kids, was always warm with hospitality.

Dave Vos largely shaped me as an engineer while I worked under his guidance at Aurora Flight Sciences, and later, when he generously agreed to volunteer his precious time to advise me in the Ph.D. program. I can not overestimate the value of his expert advice throughout the course of the project. His ability to see through seemingly complicated engineering problems is truly unique. One winter day I spent at Dave's house on Cape Cod, discussing approaches to modeling and control of aerobatic helicopters, gave me the roadmap for the rest of the project.

I was lucky to have a chance to interact with Prof. Munther Dahleh, who served on my thesis committee. Munther is a great teacher, being his teaching assistant in the class on dynamic systems was intellectually stimulating, and truly enjoyable.

Prof. John Hansman has kindly provided technical advice in the design of helicopter ground station display, and offered useful critical feedback for this manuscipt.

Prof. Carlos Cesnik, currently of University of Michigan, gave an excellent introduction to structures in his class, and effectively steered my program of studies in this area.

During both my Master's and Ph.D. program I got invaluable knowledge and inspiration from M.I.T. faculty. I am happy to acknowledge professors John Deyst, Dave Trumper, Jim Paduano, Mark Drela, Sanjoy Mitter, Dimitri Bertsekas, Marthinus Van Schoor and Klaus-Jurgen Bathe, for providing me with world-class education and making the process of acquiring it enjoyable.

I would like to thank Dr. Bernard Mettler, my colleague at M.I.T. and frequent co-author, for sharing his expertise in helicopter dynamics and his infinite patience in teaching me a proper style of technical writing.

I would like to acknowledge Prof. Emilio Frazzoli, currently of University of Illinois at Urbana-Champaign, who provided many insights during our discussions while he was a student at M.I.T. and afterwards.

This work would be impossible without the contributions of several M.I.T. students who worked with me on this hard project. I am very thankful to Ioannis Martinos, Kara Sprague, Alex Shterenberg, Rodin Lyasoff, David Dugail, and Allen Wu for contributing countless hours, frequently during week-ends and well into the nights.

My experience at M.I.T. was especially enjoyable thanks to many other interesting people, among them LIDS students Jan DeMot, Masha Ishutkina and Tom Schovenaars.

I owe infinite gratitude to my family, especially to my mother Elizaveta and my sister Evgenia, for their unconditional love and support.

Contents

1 Introduction **13**
- 1.1 Motivation, research contribution and prior work . . . 13
- 1.2 Thesis outline . . . 16

2 Experimental setup **17**
- 2.1 Airframe and avionics payload suspension system . . . 17
- 2.2 Avionics system . . . 19
- 2.3 State estimation algorithm . . . 22
- 2.4 Hardware-in-the-loop simulation . . . 28

3 Dynamic model of a miniature helicopter **31**
- 3.1 Overview of Modeling Approaches . . . 31
- 3.2 Helicopter parameters . . . 32
- 3.3 Equations of motion . . . 33
- 3.4 Component forces and moments . . . 33
  - 3.4.1 Main rotor forces and moments . . . 33
  - 3.4.2 Engine, governor and rotorspeed model . . . 44
  - 3.4.3 Fuselage forces . . . 46
  - 3.4.4 Vertical fin forces and moments . . . 47
  - 3.4.5 Horizontal stabilizer forces and moments . . . 48
  - 3.4.6 Tail rotor . . . 48
- 3.5 Actuator models . . . 52
- 3.6 Sensor models . . . 52
  - 3.6.1 Inertial measurement unit . . . 52
  - 3.6.2 Global Positioning System Receiver . . . 54
  - 3.6.3 Barometric altimeter . . . 54

4 Control system design for autonomous aggressive maneuvering **55**
- 4.1 Control approach and autopilot modes . . . 55
- 4.2 Longitudinal-vertical trim trajectory controller . . . 61
  - 4.2.1 Linearized longitudinal-vertical dynamics . . . 61
  - 4.2.2 Model reduction for control system design . . . 62
  - 4.2.3 Control system design . . . 62
- 4.3 Lateral-directional trim trajectory controller . . . 65
  - 4.3.1 Linear model and control design . . . 66
- 4.4 Human-inspired logic for automatic maneuvering . . . 69
  - 4.4.1 Axial roll maneuver . . . 70

4.4.2 Split-S maneuver 71
4.4.3 Autonomous airshow routine 72
4.5 Simplified hybrid model for motion planning 73

5 Conclusions and future work **79**
5.1 Summary 79
5.2 Future research 81

List of Figures

1-1 Miniature helicopter undergoing a Split-S maneuver. The same maneuver was performed fully autonomously using the control methods developed in this thesis. Drawing courtesy of Popular Mechanics magazine. 14

2-1 Instrumented X-Cell helicopter in flight 18
2-2 Transmissibility function for different materials 19
2-3 Vibration-isolated avionics assembly 20
2-4 Hardware-in-the-loop simulation 28

3-1 Moments and forces acting on helicopter 35
3-2 Modeling vertical acceleration response at hover 38
3-3 Rotor moments acting on the helicopter fuselage 40
3-4 Actual and model roll rate response during axial roll maneuver 42
3-5 Actual and model pitch rate response in low-speed flight 43
3-6 (top) Two frequency bands in the engine noise spectrum; (bottom) Simulated response to rotorspeed step command 46
3-7 Linearized tail rotor sideforce due to side velocity 50
3-8 Linearized tail rotor sideforce due to tail rotor pitch 50

4-1 Recorded state and input time histories for multiple axial roll maneuvers. The variables of interest are the pilot lateral cyclic control (δ_a), the helicopter roll angle (ϕ), and the pilot collective controll (coll) 57
4-2 Recorded state trajectory during a manual axial roll 58
4-3 Recorded state trajectory during an axial roll with rate tracking controllers 59
4-4 Comparing pilot rate command with a piece-wise linear approximation . . . 60
4-5 Longitudinal cyclic to pitch rate transfer function approximations 63
4-6 Longitudinal-vertical control architecture 64
4-7 Forward velocity and altitude time histories during rapid acceleration and deceleration 65
4-8 Lateral-directional controller structure 66
4-9 Lateral-directional gain variation with forward speed 67
4-10 Bank angle response 68
4-11 Phases of an autonomous aerobatic maneuver 69
4-12 Reference roll rate trajectory for axial roll maneuver 70
4-13 Recorded state trajectory during an autonomous axial roll 71
4-14 Pitch and roll rate reference trajectories for split-S maneuver 72
4-15 Recorded state trajectory during an autonomous split-S 73
4-16 Figure-8 waypoint route for the autonomous airshow routine 74

4-17 A state machine for the autonomous airshow routine 75
4-18 Flight data for the autonomous split-S - hammerhead sequence 76
4-19 A state machine representation of helicopter behavior. Dashed lines are used to indicate that certain transitions may not be allowed depending on vehicle state 76
4-20 First-order approximation of the closed-loop velocity response 77
4-21 First-order approximation of the closed-loop yaw rate response 77
4-22 First-order approximation of the closed-loop altitude rate response 78

List of Tables

3.1 Parameters of MIT Instrumented X-Cell 60 SE Helicopter 34

4.1 Autopilot Modes for MIT X-Cell Helicopter 61

Chapter 1

Introduction

1.1 Motivation, research contribution and prior work

Unmanned aerial vehicles came to play a critical role in surveillance applications in the past decade. Such vehicles usually are stable, non-agile, fixed-wing platforms, flown well above ground to collect imagery. As surveillance in a hostile urban environment becomes a necessity, so does the need for agile miniature rotorcraft with a sufficient degree of autonomy for a safe remote operation. Historically, nap-of-the-earth flying was essential for survival of helicopter crews in hostile environments [42], the same agility-enabled tactic can be envisaged for unmanned rotorcraft in an urban or mountain canyon.

Miniature helicopters with stiff hub retention and high thrust-to-weight ratio possess natural agility required for such tasks [37]. Following physical scaling rules, as the vehicle size decreases, the moments of inertia decrease with the fifth power of the scale factor, while the rotor thrust nominally decreases proportionally to the vehicle mass, i.e., to the third power. Some miniature helicopters can develop thrust 2-3 times higher than their weight, which accentuates the scaling effects. Moreover, the rotor heads of miniature rotorcraft are relatively more rigid than those in full-scale helicopters, allowing for large rotor control moments. These traits enable fast time response and high angular rates, allowing these vehicles to perform tasks that are impossible for full-scale helicopters. Many such vehicles can fly with a negative thrust, providing for sustained inverted flight. For example, expert R/C pilots perform negative-g maneuvers like the split-S, shown in Figure 1-1. Most full-scale helicopters can not sustain negative loading due to flexibility of the blades and hub retention, those few helicopters with hingeless rotors and stiff blades usually do not have high enough negative collective range.

Remotely controlled miniature helicopters equipped with film and video cameras were used in cities and mountain canyons to shoot birds-eye footage for documentaries, car commercials and action movies. This particular application requires not only agile, but also smooth maneuvering between obstacles like skyscrapers, in order to produce a high-quality footage. Such a task requires an exceptionally skilled pilot.

To enable a broader use of these extremely agile vehicles, a control methodology for an autonomous execution of aggressive maneuvers is proposed in this thesis. The resulting control laws consist of a maneuver execution logic inspired by human pilot strategies, and steady-state trim trajectory controllers, which enable safe recovery from the maneuvers. The key enabling step was the study and mathematical modeling of pilot's feedback and feedforward strategies for maneuver execution, and finding an appropriate feedback

Figure 1-1: Miniature helicopter undergoing a Split-S maneuver. The same maneuver was performed fully autonomously using the control methods developed in this thesis. Drawing courtesy of Popular Mechanics magazine.

structure, which provided repeatable execution of the maneuvers.

This control approach was tested on a 5 ft rotor diameter helicopter designed for competition aerobatics [41], which performed several aerobatic maneuvers, including a split-S, under exclusive computer control [15]. The helicopter was instrumented with a custom-designed avionics box [47], and control logic was implemented in software.

To enable the development of model-based control laws, we developed a unique nonlinear simulation model [17], which adequately represents a miniature hingeless rotor helicopter in aerobatic flight. Miniature helicopters are dominated by the strong moments produced by the rotor, which relieves the need for complicated models of secondary effects usually found in the literature on full-scale helicopters. We demonstrated that a simple physics-based model captures salient dynamics for the miniature helicopters in a wide range of flight conditions. Previously developed modeling techniques for small-scale helicopters relied on a frequency-domain system identification [40, 28]. The linear models obtained with these techniques show that a relatively low order of the state vector is sufficient for an adequate description of the helicopter dynamics around trim conditions. However, the accuracy of the frequency domain identification methods reduces in the presence of feedback [31], which is necessary in the case of an open-loop unstable system, such as a helicopter. While a

good accuracy can be achieved for higher frequency modes, the methods are unreliable for describing low-frequency modes, primarily because of the pilot feedback. The modeling framework suggested here relies on simple flight test responses such as steps and pulses to estimate those parameters that can not be measured in the lab. The resulting model is not computationally intensive, and was used in a real-time hardware-in-the-loop simulator [47], developed for exhaustive testing of the digital control system in the conditions close to those in the actual flights.

Applications of control systems to full-scale helicopters primarily dealt with improving handling qualities via limited-authority control augmentation systems [50, 9]. These systems were designed with classical control methods, sometimes using an optimization routine to match specifications [7]. Some of the recently developed attack helicopters (e.g. Boeing's Apache or Eurocopter's Tiger helicopters) featuring rotors without a flapping hinge have demonstrated an axial roll maneuver, while flown by a pilot with the assistance of a control augmentation system (apparently using angular rate feedback). Full-scale airframe manufacturers have recognized that aerobatic capability in itself is frequently an attractive feature of a vehicle, as it is used in airshows to promote sales. However, full scale helicopter aerobatics remains largely esoteric, being extremely dangerous and demanding for a pilot. To our knowledge, until now there were no reports of aerobatic maneuvers performed entirely under computer control with either full scale or miniature helicopters.

The first fully integrated autopilot for helicopters was developed in the late sixties-early seventies for CH-53A helicopter used by the Marines [42]. It was capable of waypoint navigation and automatic terrain following at low altitude. The autopilot was developed using classical techniques with sequential loop closures, which impose well-known bandwidth constraints because of the frequency separation requirement. The use of classical, decoupled feedback loops was probably driven by the available hardware, i.e. analog circuits used to implement control laws. The advent of digital control systems enabled the use of model-following controllers on US Army RAH-66 Comanche helicopter [9], first flown in the late nineties. It is interesting to note that while digital fly-by-wire systems, and hence, modern control methods (which have the potential to provide better performance than the classical control methods at a higher computational cost), found widespread use in the fixed-wing aircraft, helicopter manufacturers have been rather slow to follow the trend. This is despite the fact that flying a helicopter is, generally, much more demanding and fatiguing than flying an airplane.

Previous experimental work on autonomous control of miniature helicopters concentrated on tracking non-agile trajectories. LaCivita et al. [27] have tested an H-infinity loop shaping controller on a Yamaha R-50 helicopter. Johnson and Kannan [24] have implemented a neural network-based adaptive controller on an improved version of the R-50, the Yamaha RMAX helicopter. In both cases, an accurate tracking of simple trajectories at moderate speeds was achieved. The Yamaha helicopters are an order of magnitude heavier than the X-Cell, feature a relatively flexible hub, and are not capable of extremely agile maneuvering.

The method developed in this thesis can be used in a higher-level motion planning algorithm to utilize the agility of a vehicle. For example, Frazzoli et al. [13] developed a motion planning method based on a maneuver automaton, where vehicle motion is described by trim trajectories and discrete finite-time transitions between trim trajectories, or maneuvers. By discretizing the set of states describing the trim trajectories, and enumerating all allowable maneuvers it is possible to reduce a problem of optimal path planning for a vehicle to a tractable optimization problem [13]. To use the method in practice, the maneuvers

need to be executed in a repeatable fashion, with a guaranteed quick recovery. This calls for feedback control laws for maneuver execution, and trim trajectory controllers with fast response, examples of which are presented here.

Here we suggest another hybrid model for motion planning, which describes vehicle dynamics under the control laws developed in this thesis. It is shown here that the closed-loop dynamics under the trim-trajectory tracking controllers can be approximated by a set of decoupled first-order models (in velocity, turn rate, and altitude rate). Furthermore, vehicle behavior can be represented as a state machine, with the states being either trim trajectory control mode, or one of the maneuvers in the assembled library of maneuvers. Each maneuver has a predefined set of entry conditions (e.g. speed and altitude), and if these conditions are met for each successive maneuver, sequences of maneuvers can be performed. This connectivity property was demonstrated in flight, when the helicopter performed a hammerhead maneuver immediately after completing a split-S.

To summarize, the main contributions of the thesis are: a human-inspired control logic which enabled for the first time a fully automatic execution of aerobatic maneuvers; high-bandwidth trim trajectory controllers, which provide a smooth recovery from the maneuvers; a modeling framework for hingeless rotor miniature helicopters, which yields accurate and simple simulation models for aerobatic helicopters; and a simplified hybrid model for motion planning, which describes closed-loop helicopter dynamics under the control laws developed in this thesis.

1.2 Thesis outline

We start with describing the experimental setup used in this work in Chapter 2. First, we briefly describe the custom avionics [47] and vibration isolation mount [18] designed for a miniature aerobatic helicopter. Next, we summarize the state estimation algorithm used for modeling work in post-processing and for feedback control in real-time, and an improved measurement update algorithm, which avoids the need for normalization of attitude representation. Section 2.4 covers the hardware-in-the-loop simulation developed and used for testing the algorithms.

Chapter 3 contains a complete self-contained description of the nonlinear dynamic model for a hingeless rotor miniature helicopter. It contains equations of motion, identified and measured parameter values, as well as flight test data used for derivation of the model. For completeness we also provide dynamic models for the actuators, and error models for the sensors.

Chapter 4 describes the control logic for automatic execution of aerobatic maneuvers. Sections 4.2 and 4.3 cover the design of and flight test data for the trim trajectory controllers, which provide smooth exit from the maneuvers. Section 4.4 describes the human-inspired logic for a fully autonomous execution of aerobatic maneuvers. Section 4.5 describes the simplified hybrid model of closed loop dynamics.

The thesis concludes with Chapter 5, where we suggest further avenues of research.

Chapter 2

Experimental setup

2.1 Airframe and avionics payload suspension system

An X-Cell 60 hobby helicopter [41] was chosen as the platform for testing the autonomous aerobatics algorithms. The helicopter weighs close to 10 lbs empty, carries a 7 lb avionics payload and 1 lb of fuel, which lasts for about 9 minutes. A hingeless main rotor is equipped with a Bell-Hiller stabilizer bar [2], which provides lagged rate feedback and augments the servo torque with aerodynamic moment to change the cyclic pitch of the blades. The helicopter is powered by a piston engine running on a mixture of methanol, nitromethane and oil. In the course of the project we replaced the original engine (engine capacity .6 cubic inches, or 10 cc, with maximum horsepower of approximately 2.2) with a more powerful one (.9 cubic inches, or 15 cc, 3 horsepower maximum) to retain more maneuver margin. The helicopter is equipped with an electronic governor, an off-the-shelf device which measures rotorspeed with a magnetic sensor and adjusts throttle setting to maintain the setpoint (1600 rpm). The detailed specifications for dynamic response of the governor were not available. Based on the flight data analysis shown in Chapter 3 we concluded that the governor acts as a proportional-integral controller, and estimated the feedback gains.

Figure 2-1 shows the helicopter in flight carrying the avionics box mounted on a custom suspension system to attenuate vibration inputs. High vibration levels significantly degrade performance of inertial sensors leading to high drift rates. Vibration also makes electronics more prone to failures, such as broken solder joints or loose connectors. There are several sources of vibration on a helicopter: the main rotor, the engine, the tail rotor, all of which can excite lightly damped structural modes, e.g. first bending mode of the tail boom. Data from an experiment with hard mounted inertial sensors have shown that the most important vibration source is the one-per-rev component from the main rotor, with the nominal frequency of 26.7 Hz. The suspension system consists of four neoprene isolators, located in the corners of a rectangle. The center of gravity of the suspended assembly is located at the center of the rectangle, which serves to decouple the translational modes and the rotational ones [10]. Neoprene has a low damping ratio $\zeta = 0.05$, which leads to fast decay of the transmissibility function, at the cost of a high peak at resonance ($\times 10$). The transmissibility function, depicted in Figure 2-2 for neoprene and another material with a higher damping ratio ($\zeta = 0.15$), shows the ratio of the vibration amplitude of the suspended assembly to that of the base (airframe), given as a function of the ratio of the base vibration frequency to the natural frequency of the suspension system. According to Figure 2-2, for a low-damping material the airframe vibration inputs are attenuated

Figure 2-1: Instrumented X-Cell helicopter in flight

roughly by the square of the ratio, for a wide range of these ratios (e.g. 2-10). The choice of natural frequencies represents a tradeoff: the suspension should be flexible enough to provide adequate vibration isolation, but stiff enough to avoid coupling with the modes of interest for vehicle control. Note also that high transmissibility at resonance may lead to insufficient gain margin in a closed loop system. The gain margin problem can be alleviated by using digital notch filters at the resonant frequencies, but this leads to phase lag at lower frequencies, thereby reducing available bandwidth of the controllers. As a result, we chose desired frequencies to be in the range of 9 to 13 Hz. An additional requirement on the minimum stiffness is posed by aerobatics: the suspension system was designed to withstand 3 g's normal acceleration without bottoming out. The translational frequencies are set by the radial and axial spring stiffness ratings of the isolators given the mass of the assembly. The frequencies of the rotational modes are proportional to the distance between the isolators (and inversely proportional to the respective radii of inertia, determined with the effective torsional pendulum tests [10]). The isolators had to be located inside the box (see Figure 2-3) to achieve the desired frequencies.

For certain applications, like aerial imaging, superior vibration isolation can be achieved by using vibration mounts made of viscoelastic materials (Sorbothane, Barry-LT compound, etc), which feature higher damping ratios than neoprene. As can be seen in Figure 2-2, for a material with a damping ratio of 0.15, representative of a number of such materials, the transmissibility at resonance is reduced significantly (by a factor of 3), while it is increased only slightly at higher frequencies (e.g. at a frequency ratio of 3:1 the increase is by a factor of 1.28). Even in the absence of periodic inputs, the resonant frequency will be occasionally excited by step-like inputs from the pilot, or other disturbances (e.g. occasional engine sputtering), in which case the higher-damping materials will provide much better isolation.

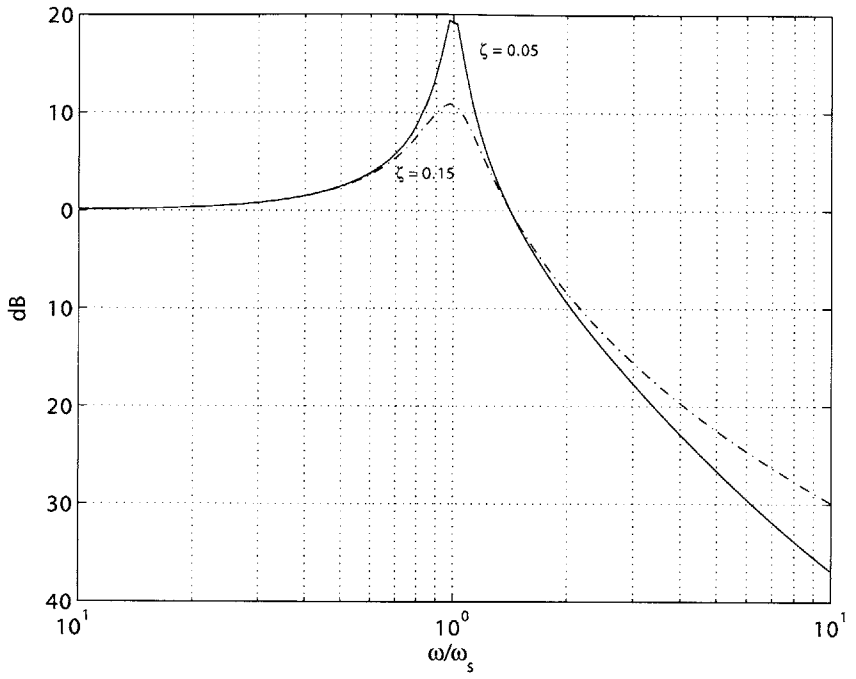

Figure 2-2: Transmissibility function for different materials

2.2 Avionics system

Autonomous aerobatics calls for a high-bandwidth control system, which in turn necessitates fast servomechanisms, low latencies in the computers, and fast sensor response. The fastest actuator response is required for modulating the tail rotor pitch. We used a newly available digital servo, Futaba S9450, which features 7 Hz no-load small-signal bandwidth (i.e. frequency at which phase lag reaches 90 degrees). The torque on the tail rotor servo is small compared to the torque rating of the servo (105 oz.-in.), pitching inertia of the tail rotor blades is almost negligible, therefore the no-load bandwidth test is representative of its performance in flight. The main rotor actuators are older analog servos Futaba S9402. These servos were tested with a mean torque load of 35 oz.-in. (stall torque 111 oz.-in.) and a small inertial load. These tests resulted in an estimate of small-signal bandwidth of 5 Hz.

The core of the sensor suite was an inertial measurement unit (IMU) from Inertial Science [23]. It contains three gyroscopes and three accelerometers. The range of gyroscopes was set at ± 300 deg/sec, and the range of accelerometers at ± 5 g's. The helicopter with the payload is capable of achieving roll rates of 200 deg/sec, and yaw rates in excess of 1,000 deg/sec. The yaw rate command was limited in software to avoid sensor saturation and ensuing instability. The IMU had an internal power regulation, temperature compensation, serial output at 100 Hz and internal first order analog anti-aliasing filters, with the corner frequency set at 9 Hz. In hindsight, the frequency of the anti-aliasing filters should have been set higher, around 20 Hz, to reduce the phase lag at lower frequencies. The drift

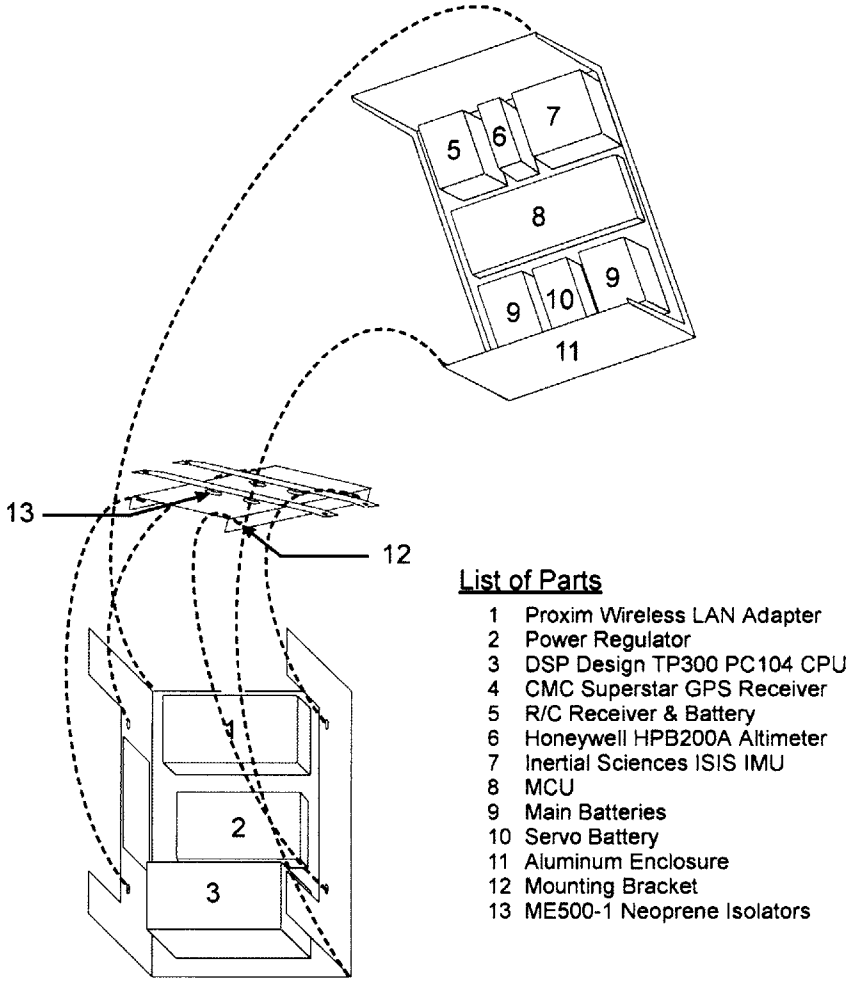

Figure 2-3: Vibration-isolated avionics assembly

rates of the gyroscopes were on the order of 0.02 deg/sec, and for accelerometers 0.02 g's for the duration of flight. To compensate for these low-frequency errors of the gyros and accelerometers, several more sensors were used to provide Kalman filter measurement updates.

A barometric altimeter, HPA200 from Honeywell, featured 2 ft resolution (0.001 psi), and excellent stability. Since the duration of flight was short, ambient pressure changes were negligible. The altimeter has an internal power regulation, temperature compensation and serial output, which was sampled at 5 Hz. Internally, pressure was sampled at 120 Hz, and averaged for 200 msec to produce the output. Since the altimeter is used to provide low-frequency updates, this effective delay was deemed tolerable. The altimeter and its pressure port were housed inside the avionics box, which shields the measurement from the pressure changes in the main rotor wake and from dynamic pressure induced by the vehicle motion and wind. It provides a reliable altitude measurement out of ground effect (about 2 rotor diameters, or 3 meters).

A Global Positioning System (GPS) receiver was used to provide 2-D (North and East) position and velocity updates. In the beginning a low-cost receiver with 1 Hz sampling period and 1 sec latency was used. A system of gravity-aiding complementary filters [47] was used to estimate vehicle attitude, and velocity estimates were re-set each time a new GPS measurement was available. A triaxial magnetic compass was used to provide heading updates. An autonomous axial roll was performed with this suite, however the attitude and velocity estimates were rather crude. A high-end receiver, G12 from Ashtech, was installed. This receiver features 10 Hz update rate and maximum 50 msec latency. An Extended Kalman Filter (EKF), described in the next section, was implemented to provide a more accurate state estimate.

A low-cost triaxial magnetic compass, used for heading updates in the original sensor suite, was discarded. The magnetoresistive sensor required an external in-flight temperature and offset compensation provided by short duration high amplitude current pulses. The sensor provided analog outputs, and highly accurate voltage reference was used. Still, after the compensation and hard-iron calibration of the compass, the heading accuracy was around 15 degrees. The EKF with the updates from the low-latency receiver provided heading accuracy on the order of 6 degrees.

It is interesting to note that the development of a sensor suite in the university environment is best implemented with smart sensors, i.e. temperature compensated, with precise internal voltage reference, and providing a digital output. To develop a highly integrated, high performance sensor suite from low-cost components requires a significant investment into laboratory equipment, and development time. For a custom one-of-a-kind, or even a low-volume-production research unit it makes economic sense to pay extra for smart sensors. The best solution would be to use an off-the-shelf miniature avionics suite with adequate performance characteristics, however such a device has not been available on the market during the project.

Other avionic devices included a flight control computer (TP400 from DSP design, with a Pentium MMX 300 MHz compatible processor, ample random access and non-volatile memory and I/O), a wireless LAN transceiver, a remote-control (R/C) receiver for pilot commands, and a custom-designed servo board for sampling pilot commands and driving the servomechanisms at 50 Hz. The flight control processor ran the QNX 4.25 real-time operating system (RTOS) [25]. The software was implemented in the C programming language with multiple processes for modularity and, hence, ease of development and testing. QNX RTOS features short context switching times, on the order of microseconds (the

context switching time is the time it takes for the processor to switch from one process, or task, to another one). The most time-critical, and therefore the highest priority software process consisted of sampling the IMU (arrival of each serial port data packet triggered a hardware interrupt), running the estimation and control logic, and sending a serial message to the servo board to drive the actuators. Since the IMU sent data at 100 Hz, and the servos were driven at 50 Hz, this sequence was performed every second IMU message. A single execution of the estimation and control logic took less than 2 msec, thereby leaving roughly 18 msec out of each 20 msec interval for the lower-priority processes (measurement updates from GPS and altimeter, sampling battery voltage, telemetry, etc). In addition, it is beneficial to minimize the time lag from sampling the IMU to driving the servos to reduce phase lag. The IMU data transfer took 1.4 msec, servo command data transfer 2.6 msec, and all the servos were commanded in parallel for 2 milliseconds (the angle of a servo deflection is proportional to a commanded pulse width, which ranges from 1 to 2 msec). Therefore the pure time delay amounted to 8 msec, well below the servo control interval of 20 msec.

Radio frequency (RF) interference was addressed in the design. An aluminum box housing the avionics provided partial protection for the RF interference; and a semi-flexible antenna guide pointing downwards was used to put the antenna in the experimentally determined most favorable location. The guide was flexible enough to land on, and at the same time kept the antenna wire away from the main rotor blades during inverted flight.

By design the servo board, R/C receiver and the servos were electrically isolated from the rest of the avionics so that the pilot still could control the servos in case of the main computer failure. However, a small-scale helicopter like X-Cell is hard to fly at low speed without the yaw rate feedback to tail rotor pitch, because of the large tail rotor control sensitivity and small natural yaw damping. In moderately fast forward flight the helicopter becomes more manageable because of the weathercocking provided by the fin and the tail rotor, and the pilot could attempt a run-in landing.

The wireless datalink was used only to download telemetry information to the ground station, where the operator monitored the status of various indicators, such as the number of GPS satellites, battery voltage, attitude indicator, etc. No information was uploaded to the helicopter after the start of the program.

2.3 State estimation algorithm

Accurate state estimation was essential for modeling work, and the Extended Kalman Filter (EKF) is a commonly used means to achieve it by blending information from various sensors. The EKF used for helicopter state estimation employed a novel representation of attitude error, suggested by Frazzoli [12]. A robust and efficient numerical implementation of the filter is described below.

The nonlinear navigation equations contain sixteen states: north-east-down position ($\hat{p}$), north-east-down velocity ($\hat{v}$), a 4-state quaternion representation of attitude ($\hat{q}$), and 3D vectors of acceleration biases ($\hat{a}_b$) and gyro biases ($\hat{\omega}_b$). The quaternion is free of singularities associated with the attitude representation based on the three Euler angles, but is subject to a unit norm constraint [46]. Denote accelerometer readings by a_m and gyro readings ω_m. Then the navigation equations are:

$$\dot{\hat{p}} = \hat{v} \tag{2.1}$$

$$\dot{\hat{v}} = \hat{C}\left(a_m - \hat{a}_b\right) + \begin{bmatrix} 0 \\ 0 \\ 1 \end{bmatrix} g \tag{2.2}$$

$$\dot{\hat{q}} = -\frac{1}{2}\left(\Omega_m - \hat{\Omega}_b\right)\hat{q} + k\lambda\hat{q} \tag{2.3}$$

$$\dot{\hat{a}}_b = 0 \tag{2.4}$$

$$\dot{\hat{\omega}}_b = 0 \tag{2.5}$$

where C is the direction cosine matrix transforming body axis coordinates to the North-East-Down (NED) system, Ω_m and $\hat{\Omega}_b$ are 4×4 skew-symmetric matrices [48] composed of the gyro measurements and gyro bias estimates, $\lambda = 1 - \|q\|_2^2$ is a deviation of the square of the quaternion norm from unity due to numerical integration errors, and k is the factor that determines the convergence speed of the numerical error. These factors serve the role of Lagrange multipliers ensuring that the norm of the quaternion remains close to unity [46]. The constraint on the speed of convergence for stability of the numerical solution is $k \cdot dt < 1$, where dt is the integration time step. The quaternion propagation equation can be discretized with an analytical computation of the exponent of the skew-symmetric matrix, given by Stevens [48]. The discrete-time attitude update can be written as:

$$q(t + dt) = \exp\left(-\frac{1}{2}\Omega \cdot dt\right) q(t) \tag{2.6}$$

Denote $\phi = \omega \cdot dt$ - an effective rotation, undergone by the body during the time period of dt, assuming that the angular rate ω remained constant during the interval. Accordingly, introduce the 4×4 skew-symmetric matrix $\Phi_4 = \Omega \cdot dt$:

$$\Phi_4 = \begin{bmatrix} 0 & \phi_x & \phi_y & \phi_z \\ -\phi_x & 0 & -\phi_z & \phi_y \\ -\phi_y & \phi_z & 0 & -\phi_x \\ -\phi_z & -\phi_y & \phi_x & 0 \end{bmatrix} \tag{2.7}$$

Then, using the idempotent property of the 4×4 skew symmetric matrices, we get:

$$\exp\left(-\frac{1}{2}\Phi_4\right) = I\cos s - \frac{1}{2}\Phi_4\frac{\sin s}{s} \tag{2.8}$$

where $s = \frac{1}{2}\|\phi\|$. Eqs. (2.6) and (2.8) ensure in theory that the updated quaternion $q(t + dt)$ has a unit norm. However, a small Lagrange multiplier term was added to Eq. (2.8) to maintain numerical stability. The use of the Lagrange multiplier term relaxes the requirement on the accuracy of computation of the trigonometric functions, and allows us to use truncated series for $\cos(s)$ and $\sin(s)/s$.

$$q(t + dt) = \left[I\left(\cos s + k \cdot dt \cdot \lambda\right) - \frac{1}{2}\Phi_4\frac{\sin s}{s}\right] q(t) \tag{2.9}$$

Eq. (2.9) and discrete-time counterparts of the velocity and position propagation equations ((2.1) and (2.2)) were integrated each time a new IMU measurement arrived, i.e. every 10 msec.

The differential equations for the state estimation error are obtained by linearizing Eqs. (2.1)-(2.5) around the current state estimate [45]. The resulting Jacobian matrix is used to

propagate the covariance matrix. The upper-triangular square root time update algorithm based on Householder orthogonalization procedure was used for higher precision [34]. The algorithm was optimized to gain speed from the sparseness of the Jacobian matrix, and the time to run the time update (by far the most expensive computation in the entire flight software) took less than 2 msec during each 20 msec control cycle.

The linear error model contains 15 states: 3D position (p), 3D velocity (v), 3D attitude error representation (ϕ), and 3D vectors for bias estimation errors for accelerometers (κ) and gyros (μ). Note that whereas the attitude vector is represented by a 4-dimensional quaternion with the unit norm constraint, the attitude error vector is three dimensional. This allows us to perform an unconstrained estimation of the attitude error. A number of 3D attitude error representations have been suggested, and a survey can be found in ref. [29]. A commonly used attitude error representation [45] is given first in the following. Let C be the true direction cosine matrix, and Φ be a 3×3 skew-symmetric matrix, whose components ϕ_x, ϕ_y, and ϕ_z represent small rotations around each of the body axis. Note also that Φ, given in Eq. (2.10), represents a vector product matrix, such that for a vector $a \in R^3$ we have $\Phi a = (\phi\times)a = -(a\times)\phi$.

$$\Phi = \begin{bmatrix} 0 & -\phi_z & \phi_y \\ \phi_z & 0 & -\phi_x \\ -\phi_y & \phi_x & 0 \end{bmatrix} \tag{2.10}$$

Then the relation between the true and estimated direction cosine matrices is represented as

$$C \approx \hat{C}\,(I + \Phi) \tag{2.11}$$

The measurement update step provides an estimate of the attitude error vector ϕ. Eq. (2.11) is then used to generate a new estimate of the direction cosine matrix, and, hence, the quaternion. However, the orthogonality property of the direction cosine matrix is lost in the update given by Eq. (2.11). An explicit orthogonalization step is required [45], introducing another source of error, and increasing computational burden. The errors introduced by the orthogonalization step grow with the magnitude of the correction, and will be most noticeable in tasks such as an in-flight alignment (attitude determination after a crude initialization). Another common 3D attitude error representation is the Gibbs vector [20], based directly on the variation of the attitude quaternion, rather than the direction cosine matrix. It also requires a normalization step after the measurement update to preserve the unit norm of the quaternion [33].

Following Frazzoli [12], instead of Eq. (2.11), the attitude error can be represented by Eq. (2.12).

$$C = \hat{C} \exp(\Phi) \tag{2.12}$$

This is equivalent to

$$q = \exp\left(-\frac{1}{2}\Phi_4\right)\hat{q} \tag{2.13}$$

given that the same 3D attitude error vector (ϕ) is used for the elements of matrix Φ_4 (Eq. (2.7)). To see the equivalence, consider attitude propagation equations based on the direction cosine and quaternion representations.

$$\dot{C} = C\Omega \tag{2.14}$$

$$\dot{q} = -\frac{1}{2}\Omega_4 q \tag{2.15}$$

Assume that the angular rate vector ω is constant during a time interval t, and denote $\phi = \omega t$. Then, provided the initial attitude represented by C_0 or q_0, the solutions of the differential equations (2.14) - (2.15) are:

$$\begin{aligned} C(t) &= C_0 \exp(\Phi) \\ q(t) &= \exp\left(-\frac{1}{2}\Phi_4\right) q_0 \end{aligned}$$

Clearly, $C(t)$ and $q(t)$ represent the same attitude.

The attitude error representation in Eq. (2.12) maintains the orthogonality of the direction cosine matrix:

$$CC^T = \hat{C}\exp(\Phi)\left(\exp(\Phi)\right)^T\hat{C}^T = \hat{C}\exp(\Phi)\exp(-\Phi)\hat{C}^T = \hat{C}\exp(\Phi-\Phi)\hat{C}^T = I \tag{2.16}$$

At the same time the linearization of Eq. (2.12) leads to Eq. (2.11), therefore the linear equations for time propagation of the state estimation error do not change. They are given in Eqs. (2.17)-(2.19).

$$\dot{p} = v \tag{2.17}$$
$$\dot{v} = \hat{C}(\hat{a}\times)\phi - \hat{C}\kappa + \hat{C}\eta \tag{2.18}$$
$$\dot{\phi} = -(\hat{\omega}\times)\phi + \mu + \gamma \tag{2.19}$$

Here $\hat{a} = (a_m - \hat{a}_b)$ and $\hat{\omega} = (\omega_m - \hat{\omega}_b)$ are accelerometer and gyro measurements with the current bias estimates subtracted, η and γ are random noise components of accelerometer and gyro measurement errors, κ and μ are bias estimate errors, modeled as random walks [19] according to the linearization of Eqs. (2.4) and (2.5).

Let us provide the derivations for velocity and attitude error propagation equations, given in Eqs. (2.18) and (2.19), respectively. Denote by V the true inertial velocity vector, the differential equation for which is:

$$\dot{V} = C(a_m - a_b - \eta) \tag{2.20}$$

Subtract Eq. (2.20) from Eq. (2.2), and neglecting second order terms with respect to the error vector we obtain:

$$\begin{aligned} \dot{v} &= \dot{\hat{v}} - \dot{V} = \hat{C}(a_m - \hat{a}_b) - C(a_m - a_b - \eta) \\ &= \hat{C}(a_m - \hat{a}_b) - C(a_m - \hat{a}_b) + C(a_m - \hat{a}_b) - C(a_m - a_b - \eta) \\ &= \left(\hat{C} - C\right)(a_m - \hat{a}_b) - C\kappa + C\eta \\ &\approx -\hat{C}\Phi a - \hat{C}\kappa + \hat{C}\eta \\ &= \hat{C}(a\times)\phi - \hat{C}\kappa + \hat{C}\eta \end{aligned}$$

Attitude propagation can be alternatively expressed with the derivative of the direction cosine matrix, resulting in the counterpart of Eq. (2.3):

$$\dot{\hat{C}} = \hat{C}\left(\Omega_m - \hat{\Omega}_b\right) \tag{2.21}$$

Similarly, we can express the derivative of the true direction cosine matrix:

$$\dot{C} = C\left(\Omega_m - \Omega_b + \Gamma\right) \tag{2.22}$$

where Γ is a skew symmetric matrix composed of the elements of the gyro noise vector (γ). Next, subtract Eq. (2.22) from Eq. (2.21), and neglect second-order terms:

$$\begin{aligned}
\dot{\hat{C}} - \dot{C} &= \hat{C}\left(\Omega_m - \hat{\Omega}_b\right) - C\left(\Omega_m - \Omega_b + \Gamma\right) \Rightarrow \\
\frac{d}{dt}\left[-\hat{C}\Phi\right] &= \hat{C}\left(\Omega_m - \hat{\Omega}_b\right) - C\left(\Omega_m - \hat{\Omega}_b\right) + C\left(\Omega_m - \hat{\Omega}_b\right) - \\
&- C\left(\Omega_m - \Omega_b\right) - C\,\Gamma \Rightarrow \\
-\hat{C}\left(\Omega_m - \hat{\Omega}_b\right)\Phi - \hat{C}\dot{\Phi} &= -\hat{C}\Phi\left(\Omega_m - \hat{\Omega}_b\right) - CM - C\,\Gamma \Rightarrow \\
\dot{\Phi} &\approx \Phi\left(\Omega_m - \hat{\Omega}_b\right) - \left(\Omega_m - \hat{\Omega}_b\right)\Phi + M + \Gamma \Rightarrow \\
\dot{\phi} &= -\left(\hat{\omega}\times\right)\phi + \mu + \gamma
\end{aligned}$$

Here M is a skew symmetric matrix composed of the elements of the gyro bias estimation error (μ).

The measurement update step remains the same until the incorporation of the computed attitude correction. Pressure altitude, 2D GPS position and 2D GPS velocity measurements were used. The updates were implemented with a fast upper triangular square root algorithm developed by Carlson [5, 34]. The method improves numerical stability of the classical measurement update step by substituting the inversion of a potentially ill-conditioned symmetric matrix with the inversion of its square root. The method maintains the square root of the covariance matrix in the upper triangular form, and was shown to incur small computational penalty compared with the original algorithm [5].

After the state error vector is calculated, the navigation filter states from the Eqs. (2.1)-(2.5) are updated. To incorporate the attitude correction (ϕ) into the quaternion estimate, we use Eq. (2.13), calculating the skew-symmetric matrix exponent analytically according to Eq. (2.8). This algorithm ensures that the quaternion norm remains equal to unity without an additional normalization step. It is also computationally more efficient than first calculating an updated direction cosine matrix from Eq. (2.12) and then finding the quaternion vector that corresponds to it.

The source of attitude updates comes from the 2D GPS position and velocity measurements. Note that the heading error becomes unobservable when the resultant of the non-gravity forces acting on the body (measured by accelerometers) is aligned with the local vertical [51]. To show this, let us rearrange the velocity error propagation equation in Eq. (2.18):

$$\dot{v} = \hat{C}\left(\hat{a}\times\right)\phi - \hat{C}\kappa + \hat{C}\eta = \left(\hat{C}\hat{a}\right) \times \left(\hat{C}\phi\right) - \hat{C}\kappa + \hat{C}\eta = \hat{a}^n \times \phi^n - \hat{C}\kappa + \hat{C}\eta \tag{2.23}$$

where $\hat{a}^n$ represents a vector of forces acting on the body in the NED coordinate frame, and $\phi^n = \begin{bmatrix} \delta\phi & \delta\theta & \delta\psi \end{bmatrix}^T$ is the attitude error vector expressed in the NED frame. From the vector product in Eq. (2.23) it follows that if $\hat{a}^n$ is aligned with the local vertical, $\delta\psi$ becomes unobservable. Therefore, some maneuvering is required for convergence of the heading error. This constraint did not represent a problem for the particular task at hand (autonomous aggressive maneuvering), however for applications requiring a prolonged

continuous hover or flight along a straight line an additional source of heading measurement would be needed.

Such a source is usually provided by a magnetometer, which measures a projection of the Earth magnetic field vector on the body axes. The measurement equation for a magnetometer with three sensitive axes is:

$$Z = \hat{C}b + \nu \quad , \tag{2.24}$$

where b represents a known local magnetic field vector, and ν is the measurement noise. Therefore the error equation for the measurement is

$$z = \left(\hat{C} - C\right) b + \nu = -\hat{C}\left(\phi\times\right) b + \nu \tag{2.25}$$

From Eq. (2.25) we can see that the rotation angle around the magnetic field vector does not contribute to the measurement. In the absence of the gyro and numerical errors an initial error rotation angle around the magnetic vector will remain constant. To show this, consider propagation of the attitude error under these conditions. Denote an initial attitude error vector by ϕ_0. Then

$$C(t_0) \;=\; \hat{C}(t_0)\exp(\Phi_0)$$

Since ideal gyro measurements are assumed, the estimate of the direction cosine matrix is propagated according to the same differential equation as the true one, with different initial conditions:

$$\dot{\hat{C}} \;=\; \hat{C}\Omega$$

Integrating the attitude matrix propagation equations

$$\begin{aligned}
\hat{C}(t) &= \hat{C}(t_0)F(t,t_0) \\
C(t) &= C(t_0)F(t,t_0) = \hat{C}(t_0)\exp(\Phi_0)F(t,t_0) \quad \text{where} \\
F(t,t_0) &= \exp\left(\int_{t_0}^{t}\Omega(\tau)d\tau\right)
\end{aligned}$$

At the same time:

$$C(t) \;=\; \hat{C}(t)\exp(\Phi(t))$$

Hence, observing that $F(t,t_0)$ is an orthogonal matrix:

$$\exp(\Phi(t)) \;=\; F^T(t,t_0)\exp(\Phi_0)F(t,t_0) \tag{2.26}$$

Eq. (2.26) shows that the attitude error follows coordinate transformation rules, therefore ϕ_0 and $\phi(t)$ represent the same attitude error vector, expressed in the original and current coordinate systems. Therefore, if ϕ_0 represents a rotation around the magnetic field vector, this error will not be changed by the magnetometer measurement updates.

Thus a magnetometer, like a star-tracker in a satellite, provides effectively two attitude angles (albeit not aligned with any of the Euler angles). Obviously, the utility of the magnetometer measurement udpate for estimating attitude depends highly on the accuracy of the local magnetic field measurement. Prominent factors affecting the accuracy are

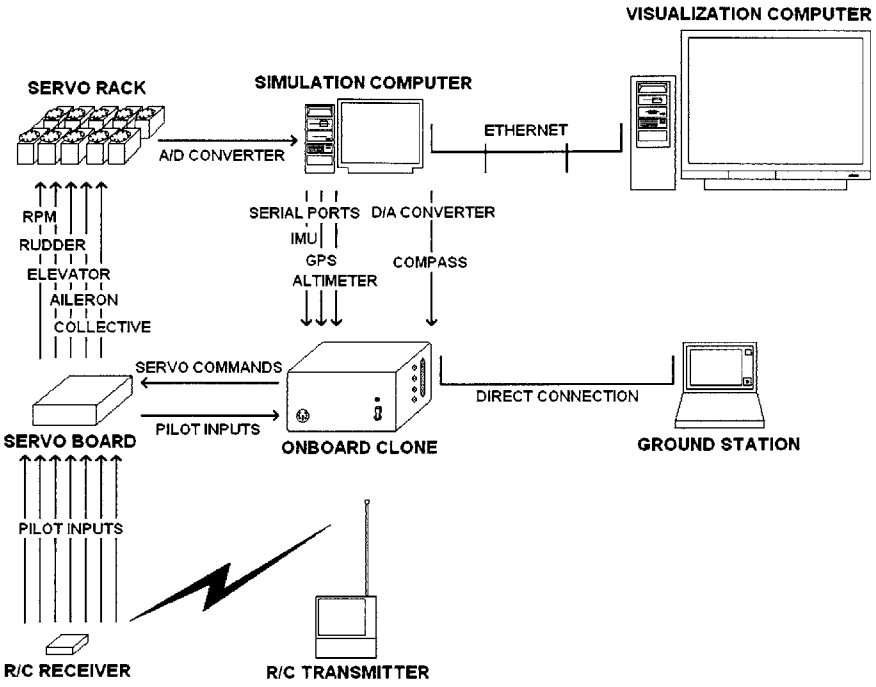

Figure 2-4: Hardware-in-the-loop simulation

temperature drifts and the magnetic field imposed by the helicopter and its payload. A combination of hardware solutions and hard-iron calibration, applied to a high-end magnetic sensor can result in accurate two-component attitude updates.

2.4 Hardware-in-the-loop simulation

An essential tool in the development of a real-time control system is a hardware-in-the-loop simulation (HILSim). It allows the engineer to test the actual software running on the target hardware in conditions as close to a real flight as is achievable in the lab.

Figure 2-4 presents a diagram of the HILSim. The so-called "clone" computer is a copy of the flight control computer running the same software; the servo board, R/C receiver and servomechanisms are also exact copies of their counterparts on the helicopter. The commands coming from the pilot get delivered to the clone via the servo board. The control logic in the clone generates servo commands based on the pilot commands and modeled sensor inputs from the simulation computer, and delivers them back to the servo board. The servo board drives the servos, their positions are sampled at 100 Hz by the simulation computer via potentiometers. In the servo rack the second row of servos represents the potentiometers (low-cost servos with the electric motors removed). The simulation computer interprets servo deflections as corresponding actuator commands, and integrates equations

of motion accordingly. It then generates sensor models based on the computed state vector and a priori models of sensor errors, and feeds these data to the clone via the interfaces the latter expects. The HILSim captures the latencies inherent in the system, an essential feature for testing real-time software.

Ideally, the servomechanisms should be appropriately spring- and inertia- loaded to simulate the effect of these factors on bandwidth. As was mentioned earlier, the actuator with the most stringent requirement for bandwidth is the tail rotor pitch, which is very lightly loaded. Therefore, we did not use loading to extend the lifetime of the servos. This deficiency of the HILSim was taken into account when the control system was designed: additional phase margin was built in.

Chapter 3

Dynamic model of a miniature helicopter

3.1 Overview of Modeling Approaches

There exists an extensive body of literature on the dynamics of full-scale helicopters. Step-by-step procedures for developing first-principles dynamic models have been devised and published [44, 2, 49, 22]. The models used in full-scale helicopter simulators typically are high-order and contain a large number of parameters that often cannot be measured directly. Moreover, once developed, models require extensive validation and refinement until they can predict the vehicle dynamic behavior accurately. Applying detailed modeling techniques is therefore not a trivial task, and may not be warranted given the differences between full-scale and miniature helicopters. Helicopters evolve in a wide range of aerodynamic conditions. Complex interactions take place between the rotor wake and the fuselage or tail. In miniature helicopters, these subtle effects tend to be "overpowered" by the large rotor forces and moments that follow quasi-instantaneously the rotor control inputs. To the author's knowledge, no examples of helicopter models covering aerobatic conditions have been published prior to this work.

Modeling techniques based on system identification have been used to derive linear models for control design, study the vehicle flying qualities, and for the validation and refinement of detailed non-linear first-principle models. Frequency domain identification methods such as CIFER [43, 50], were used to derive relatively simple linear parameterized models that capture high-frequency range of the vehicle dynamics around specific operating points. These models poorly describe lower-frequency modes because of necessary pilot's feedback during data gathering flights. Linear models are also inadequate for simulating many aspects of aerobatic flight because of the large deviations of state variables (attitudes, angular rates, and velocities) from the trim conditions.

Mettler [37] applied frequency-domain systems identification methods (CIFER) to study the characteristics of small-scale helicopters. He developed and identified parameterized linear models for hover and cruise flight conditions for the Yamaha R-50 (a 10 ft rotor diameter, 150 lb helicopter). He later applied the same parameterized model to MIT's X-Cell .60, validating and extending the observation that the rotor forces and moments largely dominate the dynamic response of small-scale helicopters. This significantly simplifies the modeling task. Both flight conditions are accurately modeled by a rigid-body model augmented with the first-order rotor and stabilizer bar dynamics; no inflow dynamics were necessary. The

coupled rotor and stabilizer bar equations can be lumped into one first-order effective rotor equation of motion (for both the lateral and longitudinal tip-path-plane flapping). The linear models accurately capture the vehicle dynamics for a relatively large region around the nominal operating point. The model accurately predicts the vehicle angular rate response for aggressive control inputs.

Following the work by Mettler, LaCivita *et al.* [28] developed a technique that makes use of the frequency responses identified from multiple operating points, for the identification of key parameters of a more broadly descriptive non-linear model. He applied the technique to Yamaha R-50 helicopter using the hover and cruise data collected in [37]. The nonlinear model with 30 states is linearized to permit a fit with the local frequency responses. It was also shown that the reduced-order linearized model, similar to the one proposed by Mettler [37], provides practically the same level of accuracy, further validating proposed simple structure of a dynamic model for miniature helicopters.

The model has typical rigid body states with the quaternion attitude representation used in order to enable simulation of extreme attitudes [46], two states for the lateral and longitudinal flapping angles, one for the rotorspeed, and one for the integral of the rotorspeed tracking error. This last state comes from the governor action, modeled with a proportional-integral feedback from the rotorspeed tracking error to the throttle command. The model covers a large portion of the X-Cell's natural flight envelope: from hover flight to about 20 m/sec forward flight. The maximum forward speed corresponds to an advance ratio $\mu = 0.15$, which is considered as relatively low [44], and permits a number of assumptions (e.g. thrust perpendicular to the rotor disk, see [6]). The cross-coupling effects in the rotor hub were also shown to be negligible for this helicopter, which further simplified model development. The mathematical model was developed using basic helicopter theory, accounting for the particular characteristics of a miniature helicopter. Most of the parameters were measured directly, several were estimated using data collected from simple flight-test experiments, involving step and pulse responses in various actuator inputs. No formal system identification procedures are required for the proposed model structure. The model's accuracy was verified using comparison between model predicted responses and responses collected during flight test data. The model was also "flown" by an expert RC pilot to determine how well it reproduces the piloted flying qualities.

Analytical linearization of the model with respect to forward speed was used to derive simple linear models. These were subsequently used for a model-based design of the controllers used for the automatic execution of aerobatic maneuvers. The actual aggressive trajectories flown by the helicopter were adequately predicted by the simulation based on the developed nonlinear model.

In the remainder of the chapter we provide a full list of model parameters with the numerical values, dynamics equations of motion, and expressions for forces and moments exerted on the helicopter by its components. Throughout the chapter we provided flight test data to validate the model for various flight regimes, including aerobatics.

3.2 Helicopter parameters

The physical helicopter parameters used for our model are given in Table 3.1. The moments of inertia around the aircraft body axes passing through the vehicle center of gravity were determined using torsional pendulum tests [10]. The cross-axis moments of inertia are hard to measure without a balancing device; and since they are usually small they were

neglected. The X-Cell main and tail rotors, as well as the stabilizer bar, have symmetric airfoils. The lift curve slopes of these surfaces were estimated according to their respective aspect ratios [26]. The effective torsional stiffness in the hub was estimated from angular rate responses to step commands in cyclic, as described in Section 3.4.1.

Note that in the table "m.r." stands for the main rotor, "t.r." stands for the tail rotor.

3.3 Equations of motion

The rigid body equations of motion for a helicopter are given by the Newton-Euler equations shown below. Here the cross products of inertia are neglected.

$$\begin{aligned}
\dot{u} &= vr - wq - g\sin\theta + (X_{mr} + X_{fus})/m \\
\dot{v} &= wp - ur + g\sin\phi\cos\theta + (Y_{mr} + Y_{fus} + Y_{tr} + Y_{vf})/m \\
\dot{w} &= uq - vp + g\cos\phi\cos\theta + (Z_{mr} + Z_{fus} + Z_{ht})/m \\
\dot{p} &= qr(I_{yy} - I_{zz})/I_{xx} + (L_{mr} + L_{vf} + L_{tr})/I_{xx} \\
\dot{q} &= pr(I_{zz} - I_{xx})/I_{yy} + (M_{mr} + M_{ht})/I_{yy} \\
\dot{r} &= pq(I_{xx} - I_{yy})/I_{zz} + (-Q_e + N_{vf} + N_{tr})/I_{zz}
\end{aligned}$$

The set of forces and moments acting on the helicopter are organized by components: $()_{mr}$ for the main rotor; $()_{tr}$ for the tail rotor; $()_{fus}$ for the fuselage (includes fuselage aerodynamic effects); $()_{vf}$ for the vertical fin and $()_{ht}$ for the horizontal stabilizer. These forces and moments are shown along with the main helicopter variables in Fig. 3-1. Q_e is the torque produced by the engine to counteract the aerodynamic torque on the main rotor blades. The helicopter blades rotate clockwise when viewed from above, therefore $Q_e \geq 0$. In the above equations we assumed that the fuselage center of pressure coincides with the c.g., therefore the moments created by the fuselage aerodynamic forces were neglected. The rotational kinematic equations were mechanized using quaternions [46]. The inertial velocities are derived from the body-axis velocities by a coordinate transformation (flat Earth equations are used), and integrated to obtain inertial position. A 4^{th} order Runge-Kutta integration method is used, with an integration step of 0.01 seconds.

3.4 Component forces and moments

3.4.1 Main rotor forces and moments

Thrust

For the main rotor thrust we assumed that the inflow is steady and uniform. According to Padfield [44, p. 126], the time constant for settling of the inflow transients at hover is given by

$$\tau_\lambda = \frac{0.849}{4\lambda_{trim}\Omega_{mr}} \tag{3.1}$$

For our helicopter the induced velocity at hover trim condition can be determined from simple momentum theory:

$$V_{imr} = \sqrt{\frac{mg}{2\rho\pi R_{mr}^2}} = 4.2 \text{ m/sec} \tag{3.2}$$

Table 3.1: Parameters of MIT Instrumented X-Cell 60 SE Helicopter

Parameter	**Description**
$m = 8.2$ kg	helicopter mass
$I_{xx} = 0.18$ kg m^2	rolling moment of inertia
$I_{yy} = 0.34$ kg m^2	pitching moment of inertia
$I_{zz} = 0.28$ kg m^2	yawing moment of inertia
$K_\beta = 54$ N·m/rad	hub torsional stiffness
$\gamma_{fb} = 0.8$	stabilizer bar Lock number
$B_{\delta_{lat}}^{nom} = 4.2$ rad/rad	lateral cyclic to flap gain at nominal rpm
$A_{\delta_{lon}}^{nom} = 4.2$ rad/rad	longitudinal cyclic to flap gain at nominal rpm
$K_\mu = 0.2$	scaling of flap response to speed variation
$\Omega_{nom} = 167$ rad/sec	nominal m.r. speed
$R_{mr} = 0.775$ m	m.r. radius
$c_{mr} = 0.058$ m	m.r. chord
$a_{mr} = 5.5$ rad^{-1}	m.r. blade lift curve slope
$C_{D_0}^{mr} = 0.024$	m.r. blade zero lift drag coefficient
$C_{T_{max}}^{mr} = 0.0055$	m.r. max thrust coefficient
$I_{\beta_{mr}} = 0.038$ kg m^2	m.r. blade flapping inertia
$R_{tr} = 0.13$ m	t.r. radius
$c_{tr} = 0.029$ m	t.r. chord
$a_{tr} = 5.0$ rad^{-1}	t.r. blade lift curve slope
$C_{D_0}^{tr} = 0.024$	t.r. blade zero lift drag coefficient
$C_{T_{max}}^{tr} = 0.05$	t.r. max thrust coefficient
$n_{tr} = 4.66$	gear ratio of t.r. to m. r.
$n_{es} = 9.0$	gear ratio of engine shaft to m. r.
$\delta_r^{trim} = 0.1$ rad	t.r. pitch trim offset
$S_{vf} = 0.012$ m^2	effective vertical fin area
$C_{L_\alpha}^{vf} = 2.0$ rad^{-1}	vertical fin lift curve slope
$\epsilon_{vf}^{tr} = 0.2$	fraction of vertical fin area exposed to t.r. induced velocity
$S_{ht} = 0.01$ m^2	horizontal fin area
$C_{L_\alpha}^{ht} = 3.0$ rad^{-1}	horizontal tail lift curve slope
$P_{eng}^{idle} = 0.0$ Watts	engine idle power
$P_{eng}^{max} = 2000.0$ Watts	engine max power
$K_p = 0.01$ sec/rad	proportional governor gain
$K_i = 0.02$ 1/rad	integral governor gain
$f_p^s = 12.5$ Hz	rolling resonance frequency of the suspension system
$f_q^s = 9.0$ Hz	pitching resonance frequency of the suspension system
$f_r^s = 9.6$ Hz	yawing resonance frequency of the suspension system
$\xi^s = 0.05$	damping ratio of the suspension system material
$S_x^{fus} = 0.1$ m^2	frontal fuselage drag area
$S_y^{fus} = 0.22$ m^2	side fuselage drag area
$S_z^{fus} = 0.15$ m^2	vertical fuselage drag area
$h_{mr} = 0.235$ m	m.r. hub height above c.g.
$l_{tr} = 0.91$ m	t.r. hub location behind c.g.
$h_{tr} = 0.08$ m	t.r. height above c.g.
$l_{ht} = 0.71$ m	stabilizer location behind c.g.

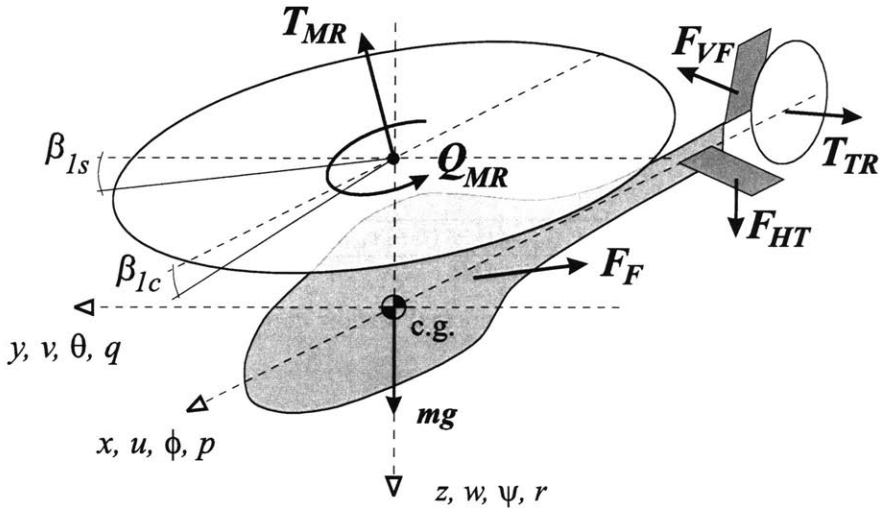

Figure 3-1: Moments and forces acting on helicopter

The tip speed of the main rotor is $V_{mr}^{tip} = \Omega_{mr} R_{mr} = 125.7$ m/sec, from which the inflow ratio is $\lambda_{imr} = V_{imr}/V_{mr}^{tip} = 0.033$. Therefore the time it takes for the inflow to settle is $\tau_\lambda = 0.038$ sec, which is significantly faster than the rigid body dynamics. During the maneuvers requiring large thrust variations the time constant may change substantially. However, as shown in the section on the main rotor flapping dynamics, the X-Cell cyclic control authority is dominated by the hub torsional stiffness, which makes the modeling of the inflow transients less critical.

A momentum theory based iterative scheme given by Padfield [44, p. 123] was adapted to compute the thrust coefficient and inflow ratio as a function of airspeed, rotor speed and collective setting. We neglect the flapping angles in the computation of the rotor thrust. The blades of the main rotor have no twist. The influence of the cyclics and the roll rate on thrust are of second order for our advance ratio range $\mu < 0.15$, and were neglected as well. We also introduced an empirically determined maximum thrust coefficient, since momentum theory does not take into account the effect of blade stall.

The thrust coefficient is given by (omitting the "mr" index):

$$C_T = \frac{T}{\rho \left(\Omega R\right)^2 \pi R^2} \tag{3.3}$$

where T is the main rotor thrust. Then the following system of equations can be solved iteratively:

$$\lambda_0 = \frac{C_T}{2\eta_w \sqrt{\mu^2 + \left(\lambda_0 - \mu_z\right)^2}} \tag{3.4}$$

$$C_T^{ideal} = \frac{a\sigma}{2}\left(\theta_0 \left(\frac{1}{3} + \frac{\mu^2}{2}\right) + \frac{\mu_z - \lambda_0}{2}\right) \tag{3.5}$$

$$C_T = \begin{cases} C_T^{ideal} & \text{if } -C_T^{\max} \le C_T^{ideal} \le C_T^{\max} \\ -C_T^{\max} & \text{if } C_T^{ideal} < -C_T^{\max} \\ C_T^{\max} & \text{if } C_T^{\max} < C_T^{ideal} \end{cases} \tag{3.6}$$

$$C_T^{\max} = \frac{T^{\max}}{\rho (\Omega R)^2 \pi R^2} \tag{3.7}$$

Here

$$\begin{aligned} \mu &= \frac{\sqrt{(u-u_{wind})^2 + (v-v_{wind})^2}}{\Omega R} \text{ - advance ratio} \\ \mu_z &= \frac{w - w_{wind}}{\Omega R} \text{ - normal airflow component} \\ \sigma &= \frac{2c}{\pi R} \text{ - solidity ratio} \\ a &- \text{ lift curve slope} \\ \theta_0 &- \text{ commanded collective angle} \\ \eta_w &- \text{ coefficient of non-ideal wake contraction} \\ T^{\max} &= 2.5 \text{ mg - maximum rotor thrust} \end{aligned}$$

Based on momentum theory, the rotor wake far downstream contracts by a factor of two [44, p. 116]. We introduced a coefficient η_w to account for non-ideal wake contraction and the power lost due to the non-uniform velocity and pressure distribution in the wake. We have approximated this coefficient to be $\eta_w = 0.9$. Hence, the iterative scheme given in [44, p. 123] is modified as follows. First, define the zero function:

$$\begin{aligned} g_0 &= \lambda_0 - \frac{C_T}{2\eta_w \Lambda^{1/2}} \text{ ,where} \\ \Lambda &= \mu^2 + (\lambda_0 - \mu_z)^2 \end{aligned}$$

and thrust coefficient C_T is given by Eq. (3.5). Apply Newton's iterative scheme:

$$\begin{aligned} \lambda_{0_{j+1}} &= \lambda_{0_j} + f_j h_j \left(\lambda_{0_j}\right) \\ h_j &= -\left(\frac{g_0}{dg_0/d\lambda_0}\right)_{\lambda_0 = \lambda_{0_j}} \end{aligned}$$

An explicit expression for h_j:

$$h_j = -\frac{\left(2\eta_w \lambda_{0_j} \Lambda^{1/2} - C_T\right)\Lambda}{2\eta_w \Lambda^{3/2} + \frac{a\sigma}{4}\Lambda - C_T\left(\mu_z - \lambda_{0_j}\right)}$$

Padfield [44, p. 123] suggests a constant value of the convergence rate coefficient $f_j = 0.6$.

Note that at hover the denominator of Eq. (3.4) is zero when the vertical velocity is equal to the inflow velocity. This condition corresponds to a vortex-ring state, which can not be modeled adequately by the momentum theory. Instead, the denominator is numerically separated from zero. In general, this condition is avoided in flight because it leads to a loss

of control. We have to keep in mind that the simulation does not adequately represent the helicopter dynamics when vortex-ring conditions exist on either the main or the tail rotor. Furthermore, strictly speaking the momentum theory applies only to a fully developed steady state flow in ascending flight. Empirical corrections for descending flight, cited by Padfield [44, p. 118], could be used to make thrust prediction somewhat more accurate.

The momentum theory approach was previously shown to be adequate for estimating steady state main rotor thrust both at hover and in fast forward flight. Results of the wind tunnel tests with a 5 ft diameter rotor are given by Harris [21] and summarized by Bramwell [2, pp. 109-114]. It was shown that the blade lift curve slope coefficient a can be determined from experiments such that the momentum theory accurately predicts thrust for a wide range of advance ratios and collective pitch angles. To test the applicability of momentum theory-based thrust calculation to transient response, we gathered flight data for collective pitch pulse responses at hover. At hover, the vertical acceleration can be represented by a linear relation:

$$a_z = Z_w w + Z_{col}\delta_{col} \tag{3.8}$$

The vertical speed damping stability derivative Z_w and the collective pitch control derivative Z_{col} can be obtained analytically by linearization of the momentum theory equations [44, pp. 219, 229]. For hover:

$$Z_w = -\frac{\rho(\Omega R)\pi R^2}{m}\frac{2a\sigma\lambda_0}{16\lambda_0 + a\sigma} \tag{3.9}$$

$$Z_{col} = -\frac{\rho(\Omega R)^2\pi R^2}{m}\frac{8}{3}\frac{a\sigma\lambda_0}{16\lambda_0 + a\sigma} \tag{3.10}$$

We used the same value for the blade lift curve slope as determined for the particular airfoil used in the tests summarized by Harris [21], $a = 5.5$. This value is consistent with the high aspect ratio of the main rotor blades, if the blades are considered as a wing [26]. The mean values were subtracted from the collective command and the vertical acceleration measurement; the signals were filtered with a first order low-pass filter with time constant of 0.2 seconds. The digital models of the analog low-pass filter and the servomechanism were applied to the collective command for consistency. Figure 3-2 shows the comparison of the computed vertical acceleration from Eq. (3.8) and actual acceleration. As can be seen, the model, based on linearization of the momentum theory, agrees well with flight data.

Torque

The main rotor torque can be approximated as a sum of induced torque due to generated thrust, and torque due to profile drag on the blades [44, p. 116]:

$$C_Q = \frac{Q}{\rho(\Omega R)^2\pi R^3} = C_T(\lambda_0 - \mu_z) + \frac{C_{D_0}\sigma}{8}\left(1 + \frac{7}{3}\mu^2\right) \tag{3.11}$$

where C_Q is the torque coefficient, C_{D_0} is the profile drag coefficient of the main rotor blade. The profile drag is not significantly affected by changes in the collective setting. Thus, the

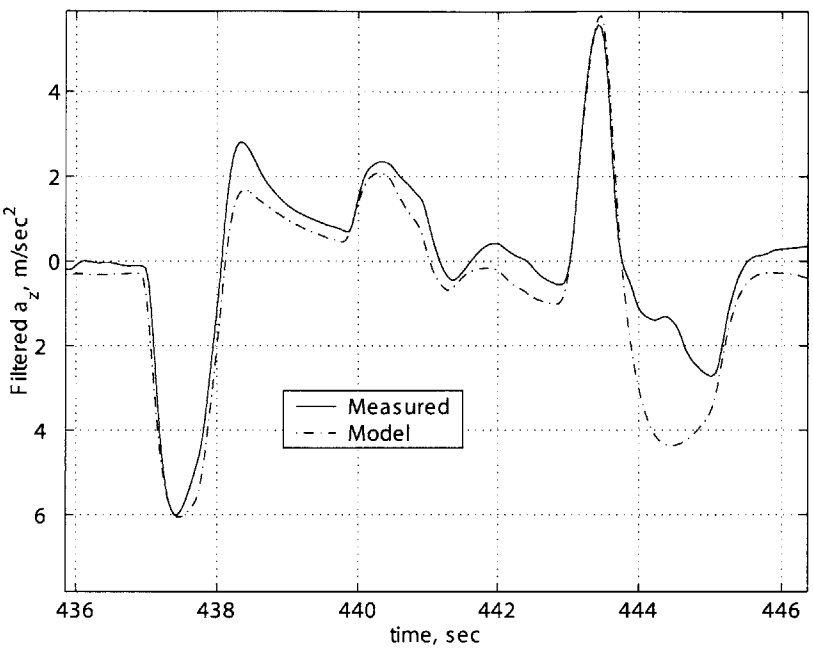

Figure 3-2: Modeling vertical acceleration response at hover

yawing moment produced by the main rotor is given by

$$Q_{mr} = C_Q \rho (\Omega R)^2 \pi R^3 \tag{3.12}$$

Our estimate for profile drag coefficient of the main rotor blade is $C_{D_0} = 0.024$. Underestimation of the profile drag coefficient would lead to overprediction of the main rotor speed in windmilling flight conditions, which occur during autorotation and some agile maneuvers.

Except for the hover condition, the rotor in-plane force, which contributes to the drag and sideforce, is substantially smaller than the drag provided by the fuselage and the sideforce from the fuselage and the empennage. This force was neglected in the calculations; effectively it was lumped with the fuselage forces, estimated in Section 3.4.3. The moments due to the in-plane force are much smaller than those due to the blade flapping, since the torsional stiffness of the hub retention is high on the X-Cell.

Main rotor moments and flapping dynamics

The main rotor flapping angle β can be represented as a Fourier series of the blade azimuth angle ψ, with only the first three coefficients retained [44, p. 32]:

$$\beta(\psi) = a_0 + a_1 \cos\psi + b_1 \sin\psi \tag{3.13}$$

Flapping of the teetering stabilizer bar can be represented by a similar equation without the constant term since no coning takes place:

$$\beta_s(\psi) = a_{1s} \sin\psi + b_{1s} \cos\psi \tag{3.14}$$

Stabilizer bar flapping contributes to the change of the main rotor blade pitch angle through a mechanical linkage:

$$\theta(\psi) = \theta_0 + \theta_{lon} \sin\psi + \theta_{lat} \cos\psi + k_s \beta_s \tag{3.15}$$

The swashplate deflections change the cyclic pitch angle of both the main rotor and the stabilizer bar. Coupled second-order differential equations can be developed for Fourier coefficients of the main rotor and stabilizer bar flapping. It can be shown [44, pp. 33-35] that the undamped natural frequency of the flapping motion is close to the rotorspeed Ω_{mr}, and the damping ratio can be approximated by $\gamma/8$, where γ is the Lock number of the blades being considered (main rotor or stabilizer bar). The Lock number represents the ratio of aerodynamic to inertial forces and is defined as

$$\gamma = \frac{\rho c a R^4}{I_\beta} \tag{3.16}$$

For the main rotor blades the Lock number is relatively high, $\gamma_{mr} \approx 3.7$, therefore the flapping motion is well damped. For a step response this corresponds to the settling time (to within 5 percent of the steady state value) of $24/\gamma\Omega = 0.039$ seconds. For the stabilizer bar, with its small aerodynamic surfaces, the Lock number is low, $\gamma_{fb} \approx 0.8$, and the corresponding settling time is 0.144 seconds. Earlier work on modeling of small-scale rotorcraft with Bell-Hiller stabilizer bars [40, 37, 28] showed that the main rotor and stabilizer bar flapping dynamics can be lumped and represented by tip-path plane (TPP) flapping dynamics with only two states. This result was based on frequency-domain identification and comparison of reduced and full order transfer functions for attitude dynamics. Furthermore, coupling of the lumped flapping dynamics and rigid body pitch and roll motions leads to pronounced second-order characteristics [52, 49, 37, 28]. These modes are lightly damped, and should be explicitly accounted for in designing high-bandwidth attitude or rate control systems [39, 38]. We represented the lateral and longitudinal flapping dynamics by the first-order equations:

$$\dot{b}_1 = -p - \frac{b_1}{\tau_e} - \frac{1}{\tau_e}\frac{\partial b_1}{\partial \mu_v}\frac{v - v_w}{\Omega R} + \frac{B_{\delta_{lat}}}{\tau_e}\delta_{lat} \tag{3.17}$$

$$\dot{a}_1 = -q - \frac{a_1}{\tau_e} + \frac{1}{\tau_e}\left(\frac{\partial a_1}{\partial \mu}\frac{u - u_w}{\Omega R} + \frac{\partial a_1}{\partial \mu_z}\frac{w - w_w}{\Omega R}\right) + \frac{A_{\delta_{lon}}}{\tau_e}\delta_{lon}, \tag{3.18}$$

where $B_{\delta_{lat}}$ and $A_{\delta_{lon}}$ are effective steady-state lateral and longitudinal gains from the cyclic inputs to the main rotor flap angles; δ_{lat} and δ_{lon} are the lateral and longitudinal cyclic control inputs (pilot stick or control system outputs); u_w, v_w and w_w are the wind components along, respectively, X, Y and Z helicopter body axes; τ_e is the effective rotor time constant for a rotor with the stabilizer bar. Frequency-domain identification showed that the pitch and roll cross-coupling flapping coefficients are approximately an order of magnitude less than the direct coefficients for the X-Cell [37], and were neglected. This result holds for large-amplitude inputs as well. For example, during an axial roll maneuver the pitch rate remains close to zero with no pilot compensation, similarly to the roll rate during a loop. This natural decoupling of the cyclic responses makes the X-Cell a particularly attractive helicopter for aerobatics.

The dominant rotor moments are the control moments produced by the rotor flapping. In the following we describe the moments in the roll direction (resulting from the lateral

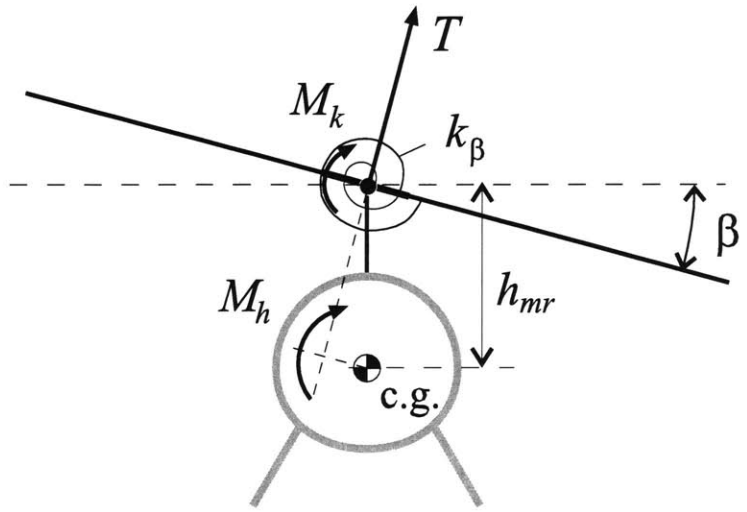

Figure 3-3: Rotor moments acting on the helicopter fuselage

TPP flapping b_1). Figure 3-3 shows the rotor moments that are acting on the fuselage. The first contribution results from the restraint in the blade attachment to the rotor head. The restraint can be approximated using a linear torsional spring with a constant stiffness coefficient K_β; resulting in a roll moment $M_{k,lat} = K_\beta b_1$. The second contribution results from the tilting of the thrust vector. Assuming that the thrust vector is perpendicular to the TPP, the thrust vector will tilt proportionally to the rotor flapping angles. The moment arm is the distance h_{mr} between the rotor head and the helicopter center of gravity; resulting in a lateral moment $M_{h,lat} = T h_{mr} b_1$. The total main rotor rolling moment, entering the rigid body equations of motion, is represented by Eq. (3.19).

$$L_{mr} = (K_\beta + T h_{mr})\, b_1 \tag{3.19}$$

Similarly, the pitching moment is given by Eq. (3.20).

$$M_{mr} = (K_\beta + T h_{mr})\, a_1 \tag{3.20}$$

To determine the parameters entering the flapping equations, we can split up the problem into "slow" and "fast" dynamics. First, we can notice that the dihedral derivatives are important only at the low-frequency spectrum of the dynamics. At high frequencies (above 0.5 Hz) the transfer functions from cyclic inputs to angular rates can be approximated by second-order transfer functions, derived by omitting the translational flapping derivatives

in Eqs. (3.17)-(3.18) and combining it with Eqs. (3.19)-(3.20):

$$\frac{q}{\delta_{lon}} \approx \frac{A_{\delta_{lon}}}{\tau_e} \frac{\omega_{nq}^2}{s^2 + 1/\tau_e s + \omega_{nq}^2} \tag{3.21}$$

$$\frac{p}{\delta_{lat}} \approx \frac{B_{\delta_{lat}}}{\tau_e} \frac{\omega_{np}^2}{s^2 + 1/\tau_e s + \omega_{np}^2} \tag{3.22}$$

Pitching dynamics in fast forward flight is significantly influenced by the horizontal tail, which provides a stabilizing effect, and the main rotor flapping due to vertical speed, which provides a destabilizing effect. Therefore the longitudinal cyclic to pitch rate transfer function given in Eq. (3.21) is valid in low-speed flight only. Here the undamped natural frequencies of the longitudinal and lateral fuselage-rotor modes are:

$$\omega_{nq} = \sqrt{\frac{T_{mr} h_{mr} + K_\beta}{I_{yy}}}$$

$$\omega_{np} = \sqrt{\frac{T_{mr} h_{mr} + K_\beta}{I_{xx}}}$$

Note that for hover and straight and level flight $T_{mr} \approx mg$. The distance between the main rotor hub and the helicopter center of gravity can be measured. The moments of inertia were determined with the torsional pendulum tests [10]. The natural frequencies of the lightly damped second-order systems can be easily determined by counting oscillation periods in a recorded step response, thereby providing an estimate of the hub torsional stiffness. These parameters are given in Table 3.1. An approximate value of the damping time constant for the flapping motion [37] is given in Eq. (3.23)

$$\tau_e = \frac{16}{\gamma_{fb} \Omega_{mr}} \approx 0.1 \text{ sec} \tag{3.23}$$

Note that the damping is proportional to the stabilizer bar Lock number, making it small. The steady-state cyclic to rate gains depend on the swashplate gearing. Experiments have also indicated that the values of $B_{\delta_{lat}}$ and $A_{\delta_{lon}}$ grow with the rotor speed. We approximated this effect as a function of effective dynamic pressure, or square of the rotor speed:

$$B_{\delta_{lat}} = B_{\delta_{lat}}^{nom} \left(\frac{\Omega}{\Omega_{nom}} \right)^2 \text{ rad/rad}$$

$$A_{\delta_{lon}} = A_{\delta_{lon}}^{nom} \left(\frac{\Omega}{\Omega_{nom}} \right)^2 \text{ rad/rad}$$

$$\Omega_{nom} = 167 \text{ rad/sec}$$

These gains were determined by matching DC gain of the angular rate responses to steps in cyclics. Final verification of the derived parameters is provided by simulation of the linear systems described in Eq. (3.21) and (3.22), and comparison with the flight-test data. Figure 3-4 shows the actual and simulated roll rates for a segment including an axial roll maneuver. The helicopter undergoes negative rotor loading during inverted portion of the maneuver, leading to 15 percent lower roll rate in that segment than predicted by the simplified linear model. Figure 3-5 shows the actual and simulated pitch rates for a segment of 15 m/sec forward flight with pulse commands on longitudinal cyclic. Note

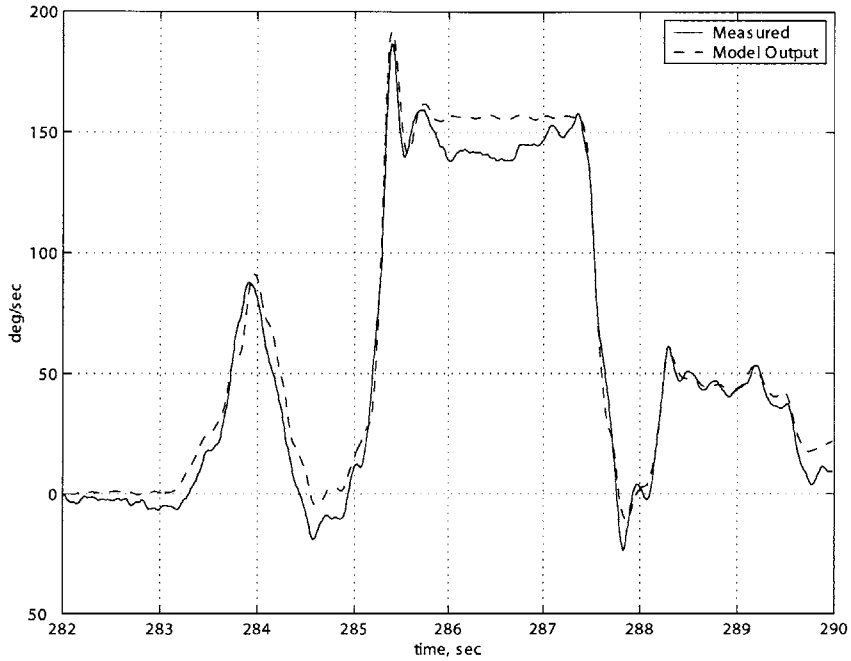

Figure 3-4: Actual and model roll rate response during axial roll maneuver

that the linearized models of angular rate dynamics are adequate for both small and large amplitude motion.

The flapping due to translational velocity is described by the flapping derivatives $\partial a_1/\partial \mu$ and $\partial b_1/\partial \mu_v$. The longitudinal flapping due to the forward speed increase is caused by an increased lift on the advancing blade with respect to the retreating blade, which turns into a flap-back moment on the main rotor due to the 90 degree gyroscopic phase lag. A theoretical value for the steady-state longitudinal flapping for a rotor without a stabilizer bar is given by [2, p. 107]

$$a_1 = \frac{2\mu\,(4\delta_{col}/3 - \lambda_0)}{1 + 3\mu^2/2} \approx 2\mu\,(4\delta_{col}/3 - \lambda_0) \tag{3.24}$$

While this expression is valid for a teetering rotor at hover, theoretical approximation for a hingeless rotor without a stabilizer bar is very close [44]. The stabilizer bar dramatically reduces flapping response to gusts, and Eq. (3.24) can not be used for predicting dihedral effect on a rotor equipped with one. Since this derivative plays a primary role in the frequency and damping of the phugoid mode, which is very slow, it is difficult to estimate with the frequency domain identification methods [37]. An open loop excitation would have to last for much longer than it takes for the helicopter to diverge, therefore the necessary pilot's feedback would bias an estimate of the derivative [31]. We introduced a scaling coefficient in Eq. (3.24), and linearized it to yield

$$\frac{\partial a_1}{\partial \mu} = 2K_\mu \left(\frac{4\delta_{col}}{3} - \lambda_0\right) \tag{3.25}$$

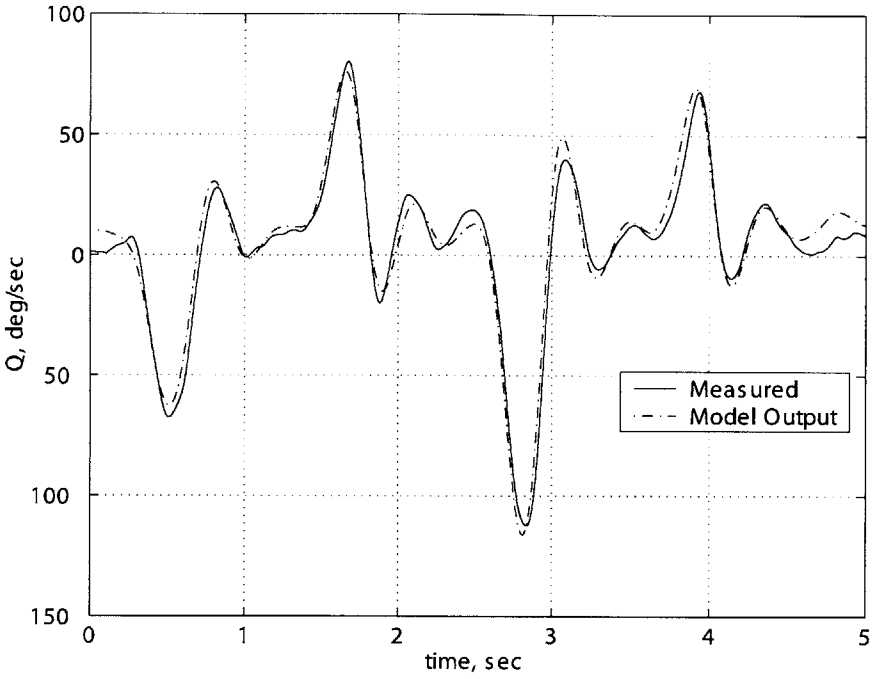

Figure 3-5: Actual and model pitch rate response in low-speed flight

A rough estimate for the scaling coefficient K_μ can be obtained by matching the steady-state cyclic input in forward flight at constant speed (maintained with the velocity-tracking feedback controller) with that predicted by the simulation in the same conditions. Our estimate for X-Cell 60 yielded $K_\mu = 0.2$, which tells us that the stabilizer bar reduces steady-state flapping response to forward speed by a factor of 5. From Eq. (3.24) and the rotor symmetry we conclude that the longitudinal and lateral dihedral derivatives are equal in magnitude, and in both cases cause the rotor to flap away from the incoming air.

$$\frac{\partial b_1}{\partial \mu_v} = -\frac{\partial a_1}{\partial \mu} \tag{3.26}$$

Positive Z-axis velocity causes higher lift on advancing blade, which results in a flap-back of the rotor; this effect is captured by the stability derivative $\partial a_1/\partial \mu_z$ in Eq. (3.17). An analytical estimate of the derivative is adapted [2, p. 159] to accommodate backward flight, and scaled by the same coefficient K_μ to reflect the effect of the stabilizer bar:

$$\frac{\partial a_1}{\partial \mu_z} = K_\mu \frac{16\mu^2}{(1-\mu^2/2)\,(8\,|\mu| + a\sigma)} \operatorname{sign} \mu \approx K_\mu \frac{16\mu^2}{8\,|\mu| + a\sigma} \operatorname{sign} \mu \tag{3.27}$$

Rotor forces

For small advance ration flight ($\mu < 0.15$) we can assume that the thrust vector is perpendicular to the TPP. The small flapping angles (below 10 degrees) allow us to use linear approximation for the main rotor force components along the helicopter body axes. As was stated above, the in-plane rotor force was lumped with the fuselage forces, and is not

accounted for in the equations below.

$$\begin{aligned} X_{mr} &= -T_{mr}a_1 \\ Y_{mr} &= T_{mr}b_1 \\ Z_{mr} &= -T_{mr} \end{aligned}$$

3.4.2 Engine, governor and rotorspeed model

The rotorspeed dynamics is modeled by the following equation:

$$\dot{\Omega} = \dot{r} + \frac{1}{I_{rot}}\left[Q_e - Q_{mr} - n_{tr}Q_{tr}\right] \tag{3.28}$$

where Q_e is the engine torque (positive clockwise), $Q_{mr} = C_Q\rho(\Omega R)^2\pi R^3$ is the main rotor torque (positive counterclockwise), Q_{tr} is the tail rotor torque, n_{tr} is the tail rotor gear ratio, I_{rot} is the total rotating inertia referenced to the main rotor speed, and Ω is the rotorspeed. The engine torque depends on the throttle setting δ_t and rotorspeed, and is usually represented by engine maps, or look-up tables. The maps for the engine were not available, and a simplified representation of the engine torque is suggested. Assume that engine power is proportional to the throttle setting:

$$P_e = P_e^{\max}\delta_t \tag{3.29}$$

where $0 < \delta_t < 1$. Then the torque is

$$Q_e = \frac{P_e}{\Omega} \tag{3.30}$$

The engine torque response to throttle changes can be considered instantaneous, since the time lags associated with air intake, fuel flow and combustion are very small compared to vehicle dynamics.

In the absence of manufacturer data, the governor can be modeled as a proportional-integral feedback controller, maintaining commanded rotorspeed by changing the throttle:

$$\begin{aligned} \delta_t &= K_p \cdot (\Omega_c - \Omega) + K_i \cdot \omega_i \\ \dot{\omega}_i &= \Omega_c - \Omega \end{aligned} \tag{3.31}$$

where Ω_c is the rotorspeed command, K_p and K_i are proportional and integral feedback gains. The anti-windup logic resets the integrator state value ω_i in case computed throttle command is saturated. Throttle servo dynamics is much faster than the rotorspeed dynamics, and was neglected in the model.

To determine the parameters of the given engine/governor model, we analyzed time response to the rotorspeed step command. Let us linearize Eqs. (3.28)-(3.31) around a nominal operating point, for example hovering flight, neglecting the yawing acceleration and the tail rotor torque. The states of the linear system will be the rotorspeed deviation from the nominal ω and an integral of the rotorspeed tracking error ω_i. The inputs are ω_c - a variation of the rotorspeed command, and δ_c - a variation of the collective angle from

the trim setting. The resulting linear system is given in Eq. (3.32).

$$\frac{d}{dt}\begin{bmatrix} \omega \\ \omega_i \end{bmatrix} = \begin{bmatrix} -\frac{1}{\Omega I_{rot}}\left(3Q^0_{mr} + P^{max}_e K_p\right) & \frac{P^{max}_e K_i}{\Omega I_{rot}} \\ -1 & 0 \end{bmatrix}\begin{bmatrix} \omega \\ \omega_i \end{bmatrix} + \\ + \begin{bmatrix} \frac{P^{max}_e K_p}{\Omega I_{rot}} & -\frac{1}{I_{rot} C_Q}\frac{\partial C_Q}{\partial \delta_c} Q^0_{mr} \\ 1 & 0 \end{bmatrix}\begin{bmatrix} \omega_c \\ \delta_c \end{bmatrix} \tag{3.32}$$

From Eq. (3.11) the main rotor torque at hover Q^0_{mr} can be computed, and for the X-Cell with the parameters given in Table 3.1 $Q^0_{mr} \approx 6.3$ Nm. The characteristic polynomial of the system is given in Eq. (3.33).

$$\chi(\lambda) = \lambda^2 + \lambda\frac{3Q^0_{mr} + P^{max}_e K_p}{\Omega I_{rot}} + \frac{P^{max}_e K_i}{\Omega I_{rot}} \tag{3.33}$$

To estimate the coefficients of the characteristic polynomial we performed the following test [47]. The helicopter was kept at hover at 1600 rpm, and a 100 rpm step input in rotorspeed was commanded to the governor from a remote control. The rotorspeed measurement was not available directly in the instrumentation package. Instead, we recorded the sound of the engine with a hand-held camcorder. Next, a time-frequency decomposition analysis [11] was applied to determine frequency content of the engine noise as a function of time. In such an analysis a signal of limited duration and frequency, called a wavelet, defined by its central frequency and width, is convoluted in the time domain with the data. The output in the time domain will have a larger magnitude when the wavelet's central frequency is present in the signal than when the central frequency is missing. The spectral content of the signal as a function of time can then be determined by repeating this computation over a range of frequencies. Many frequency bands appear in the sound spectrum of the engine noise, representing harmonics. Figure 3-6 (top) shows the result of the Morlet wavelet time-frequency analysis performed on the engine noise during a step change in RPM setting; two harmonics are indicated. The same behavior appears on each harmonic, providing the opportunity to fine-tune the model to a number of step-responses, thereby reducing measurement error due to external noise. The governor/engine system was approximated with a second order system, whose response to a commanded RPM step input appears at the bottom of Figure 3-6. The system's damping ratio is $\zeta = 0.63$ and its natural frequency is $\omega_n = 1.3$ rad/sec. By matching the coefficients of the characteristic polynomials we obtain the expressions given in Eq. (3.34).

$$\begin{aligned} 2\zeta\omega_n &= \frac{3Q^0_{mr} + P^{max}_e K_p}{\Omega I_{rot}} \\ \omega_n^2 &= \frac{P^{max}_e K_i}{\Omega I_{rot}} \end{aligned} \tag{3.34}$$

A total kinetic energy of all rotating components is $2I_{\beta_{mr}}\Omega^2 + I_{es}(n_{es}\Omega)^2 + 2I_{\beta_{tr}}(n_{tr}\Omega)^2 = (2I_{\beta_{mr}} + I_{es}n^2_{es} + 2I_{\beta_{tr}}n^2_{tr})\Omega^2$, where $I_{\beta_{mr}}$ and $I_{\beta_{tr}}$ are, respectively, the main and the tail rotor blade inertias, I_{es} is the inertia of the engine shaft and all components rotating at the engine speed, n_{tr} is the tail rotor gear ratio, and n_{es} is the engine gear ratio. Therefore the rotating inertia referenced to the main rotor speed can be represented as $I_{rot} = 2I_{\beta_{mr}} + I_{es}n^2_{es} + 2I_{\beta_{tr}}n^2_{tr}$. The most important contribution comes from the main rotor blades. The

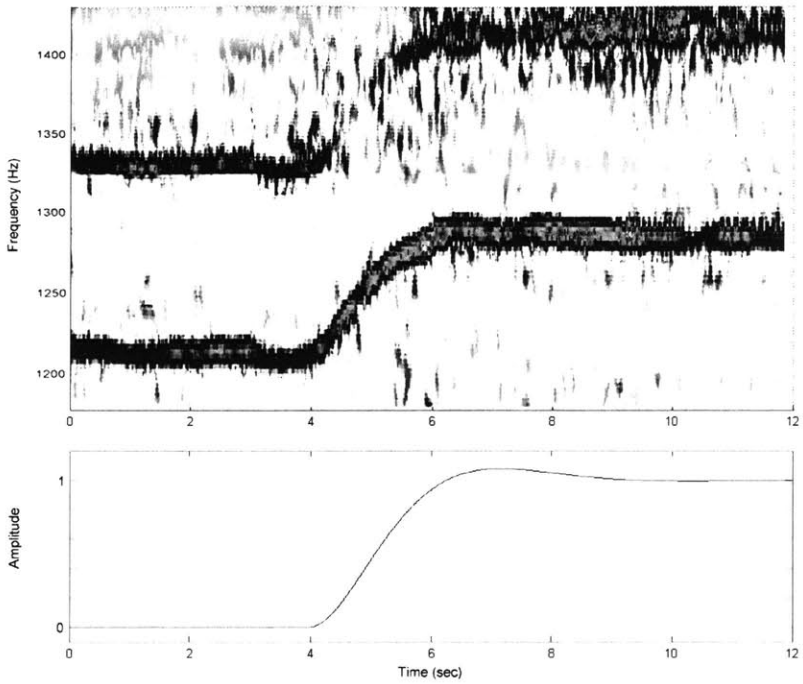

Figure 3-6: (top) Two frequency bands in the engine noise spectrum; (bottom) Simulated response to rotorspeed step command

tail rotor inertia, after scaling with the gear ratio squared, amounts to 5 percent of the main rotor inertia. The rotating inertia referenced to the engine speed is harder to estimate, but an upper bound can be found by estimating the total mass of rotating components (0.2 kg) and its effective radius of inertia (0.04 m). We thus arrived at an estimate for I_{rot} equal to 2.5 inertias of the main rotor blade. Using this value, and matching coefficients of the characteristic polynomial according to Eq. (3.34) we obtained estimates for the proportional and integral governor gains. The model could be further refined if real-time rotorspeed data were available, or the actual governor gain and the engine maps were available from the manufacturer datasheets.

This engine/governor model is simplified. However, it reflects the trends which are important in some very aggressive maneuvers which involve large and rapid variation of the aerodynamic torque on the rotor. First, tight governor feedback keeps the rotorspeed close to the nominal setting. Second, an increase in the aerodynamic torque leads to a temporary decrease in rotorspeed and a lagged application of the yawing torque to the airframe. The reverse is true for windmilling flight, in which the rotor extracts energy from the air, and leads to an increase in rotorspeed, and lagged decrease in torque applied to the airframe. The inaccuracies in the model would probably preclude feedforward compensation of the main rotor torque with the tail rotor; a tight yaw rate feedback to the tail rotor pitch is much more efficient and is routinely used by R/C pilots in the form of a yaw gyro.

3.4.3 Fuselage forces

For hover flight and forward speeds well below the induced velocity at hover ($\approx$ 4.5 m/sec for X-Cell), the rotor downwash is deflected by the forward and side velocity. This deflection creates a force opposing the movement. We can express the X and Y drag forces created

by the fuselage in this flight regime by:

$$\begin{aligned} X_{fus} &= S_x^{fus}\frac{1}{2}\rho V_{imr}^2\frac{u}{V_{imr}} \\ Y_{fus} &= S_y^{fus}\frac{1}{2}\rho V_{imr}^2\frac{v}{V_{imr}} \end{aligned}$$

where S_x^{fus} and S_y^{fus} are effective drag areas of the fuselage in the X and Y directions.

When the forward speed is higher than the rotor induced velocity, the fuselage drag can be modeled as the drag of a flat plate exposed to dynamic pressure. In this case the perturbations to the fuselage forces can be expressed as:

$$\begin{aligned} X_{fus} &= S_x^{fus}\frac{1}{2}\rho U_e^2\frac{u}{U_e} \\ Y_{fus} &= S_y^{fus}\frac{1}{2}\rho U_e^2\frac{v}{U_e} \end{aligned}$$

where U_e is the trim airspeed.

Considering the above equations, fuselage forces can be approximated by

$$\begin{aligned} V_\infty &= \sqrt{u_a^2 + v_a^2 + (w_a + V_{imr})^2} \\ X_{fus} &= -0.5\rho S_x^{fus} u_a V_\infty \\ Y_{fus} &= -0.5\rho S_y^{fus} v_a V_\infty \\ Z_{fus} &= -0.5\rho S_z^{fus}\left(w_a + V_{imr}\right) V_\infty \end{aligned}$$

where S_x^{fus}, S_y^{fus} and S_z^{fus} are effective frontal, side and vertical drag areas of the fuselage, u_a, v_a and w_a are fuselage center of pressure velocities with respect to air (i.e. $u_a = u - u_w$, where u_w is the projection of wind velocity vector on the X body axis). We neglect small moments generated by the fuselage, and assume that the fuselage center of pressure coincides with the helicopter center of gravity. Based on the fuselage projection areas, we can assume that $S_y^{fus} \approx 2.2 S_x^{fus}$, $S_z^{fus} \approx 1.5 S_x^{fus}$. Effective frontal drag area can be determined from the average pitch angle required to maintain a certain forward speed. This is best done under automatic control in velocity hold mode. In a steady trimmed flight $mg\theta \approx -0.5\rho U^2 S_x^{fus}$. A pitch angle of -10 degrees was required to maintain 14.5 m/sec forward speed, which resulted in the estimate $S_x^{fus} = 0.1$ square meters.

3.4.4 Vertical fin forces and moments

We approximated the sideforce produced by the vertical fin by:

$$Y_{vf} = -0.5\rho S_{vf}\left(C_{L_\alpha}^{vf} V_\infty^{tr} + |v_{vf}|\right) v_{vf} \tag{3.35}$$

where S_{vf} is the vertical fin area, $C_{L_\alpha}^{vf}$ is its lift curve slope, $V_\infty^{tr} = \sqrt{u_a \cdot u_a + w_{tr} \cdot w_{tr}}$ is the axial velocity at the location of the tail rotor hub. v_{vf} is the side velocity relative to air at the location of the vertical fin, w_{tr} is the vertical velocity (same as for the tail rotor):

$$v_{vf} = v_a - \epsilon_{vf}^{tr} V_{itr} - l_{tr} r \tag{3.36}$$

$$w_{tr} = w_a + l_{tr} q - K_\lambda \cdot V_{i_{mr}} \tag{3.37}$$

Here V_{itr} is the induced velocity of the tail rotor (see Eq. (3.50)), r is yaw rate, ϵ_{vf}^{tr} is the fraction of the vertical fin area exposed to full induced velocity from the tail rotor, l_{tr} is the vertical distance between the c.g. and tail rotor hub, which is about the same distance to the center of pressure of the vertical fin, $V_{i_{mr}}$ - main rotor induced velocity, K_λ - wake intensity factor, calculated in the tail rotor section.

To accommodate for stall of the vertical fin [35], the absolute value of the vertical fin side force is limited by:

$$|Y_{vf}| \leq 0.5\rho S_{vf}\left(\left(V_\infty^{tr}\right)^2 + v_{vf}^2\right) \tag{3.38}$$

The vertical fin sideforce creates a yawing moment and a small rolling moment due to the offsets from the c.g.:

$$\begin{aligned} N_{vf} &= -Y_{vf} l_{tr} \\ L_{vf} &= Y_{vf} h_{tr} \end{aligned}$$

3.4.5 Horizontal stabilizer forces and moments

The destabilizing effect of the main rotor flapping due to vertical speed is offset by the weathervaning provided by the horizontal tailplane. The horizontal tail produces lift and a stabilizing pitching moment around the center of gravity. An effective vertical speed at the horizontal tail location is determined, assuming that the stabilizer may be fully or partially submerged in the downwash of the main rotor:

$$w_{ht} = w_a + l_{ht} q - K_\lambda \cdot V_{i_{mr}} \tag{3.39}$$

The same wake intensity factor is used for the horizontal fin as for the vertical fin and the tail rotor. Next, the Z-force generated by the horizontal stabilizer is determined according to:

$$Z_{ht} = 0.5\rho S_{ht}\left(C_{L_\alpha}^{ht} |u_a| w_{ht} + |w_{ht}| w_{ht}\right) \tag{3.40}$$

where S_{ht} is the horizontal stabilizer area, $C_{L_\alpha}^{ht} = 3.0$ is its lift curve slope. To accommodate for the stall of the horizontal stabilizer [35], the absolute value of the horizontal stabilizer lift is limited by:

$$|Z_{ht}| \leq 0.5\rho S_{ht}\left(u_a^2 + w_{ht}^2\right) \tag{3.41}$$

Finally, the pitching moment generated by the horizontal stabilizer is

$$M_{ht} = Z_{ht} \cdot l_{ht} \tag{3.42}$$

3.4.6 Tail rotor

The tail rotor is subjected to a wide range of flow conditions, including those where the thrust-inflow iteration algorithm (given for the main rotor in Eqs. (3.4) and (3.5)) would fail (e.g. when the tail rotor operates in its own wake at a low in-plane airspeed). We have linearized the thrust-inflow iteration equations for the tail rotor around the trim conditions corresponding to a no-sideslip flight at a range of forward speeds. The tail rotor thrust at such trim conditions is always non-zero to compensate for the main rotor torque, zero sideslip implies that there is no airflow component normal to the rotor disk, therefore Eqs.

(3.4) and (3.5) are applicable.

$$C^{tr}_{T_{\mu_z^{tr}}} = \frac{\partial C_T^{tr}}{\partial \mu_z^{tr}} \left(|\mu_{tr}|, \mu_z^{tr} = 0, \delta_r^{trim} \right) \tag{3.43}$$

$$C^{tr}_{T_{\delta_r}} = \frac{\partial C_T^{tr}}{\partial \delta_r} \left(|\mu_{tr}|, \mu_z^{tr} = 0, \delta_r^{trim} \right) \tag{3.44}$$

The partial derivatives in Eqs. (3.43) and (3.44) were computed numerically. Simple approximate analytical expressions for the tail rotor coefficients can be obtained by adapting those used for the main rotor coefficients [44, pp. 219, 229]. They fall within 15 percent of those computed via numerical or exact analytical linearization. The resulting non-dimensional coefficients were used to calculate the corresponding dimensional stability derivatives:

$$Y_v^{tr} = -C^{tr}_{T_{\mu_z^{tr}}} \frac{f_t \rho \Omega_{tr} R_{tr} \pi R_{tr}^2}{m} \tag{3.45}$$

$$Y_{\delta_r}^{tr} = -C^{tr}_{T_{\delta_r}} \frac{f_t \rho \left(\Omega_{tr} R_{tr}\right)^2 \pi R_{tr}^2}{m} \tag{3.46}$$

where f_t is the fin blockage factor, as suggested in [44, p. 142]:

$$f_t = 1.0 - \frac{3}{4} \frac{S_{vf}}{\pi R_{tr}^2}$$

The tail rotor speed is given by $\Omega_{tr} = n_{tr} \Omega_{mr}$, where n_{tr} is the gear ratio given in Table 3.1. For reference, the computed dimensional derivatives are provided in Figures 3-7 and 3-8. Finally, the sideforce generated by the tail rotor is given in Eq. (3.47):

$$Y_{tr} = m Y_{\delta_r}^{tr} \delta_r + m Y_v^{tr} \mu_z^{tr} \Omega_{tr} R_{tr} \tag{3.47}$$

In order to calculate Y_{tr}, we need to determine the normal (μ_z^{tr}) and the in-plane (μ_{tr}) tail rotor inflow components. The main rotor wake affects the tail rotor thrust in a complex way; to model this influence accurately an extensive modeling of the wake is required. We decided to approximate just the increase in an apparent in-plane velocity seen by the tail rotor. For this, determine the main rotor wake intensity factor K_λ. The geometry calculations are equivalent to those given in [30], but computationally more efficient since an explicit evaluation of the trigonometric functions is avoided. Calculate the following variables (tangents of the angles determining the geometry):

$$g_i = \frac{l_{tr} - R_{mr} - R_{tr}}{h_{tr}}$$

$$g_f = \frac{l_{tr} - R_{mr} + R_{tr}}{h_{tr}}$$

First, the tail rotor is out of the downwash if $V_{i_{mr}} \leq w_a$, in which case there is an effective upwash. Next, at low enough forward speed with respect to air the tail rotor is out of the wake as well. This can be represented by the condition:

$$\frac{u_a}{V_{i_{mr}} - w_a} \leq g_i$$

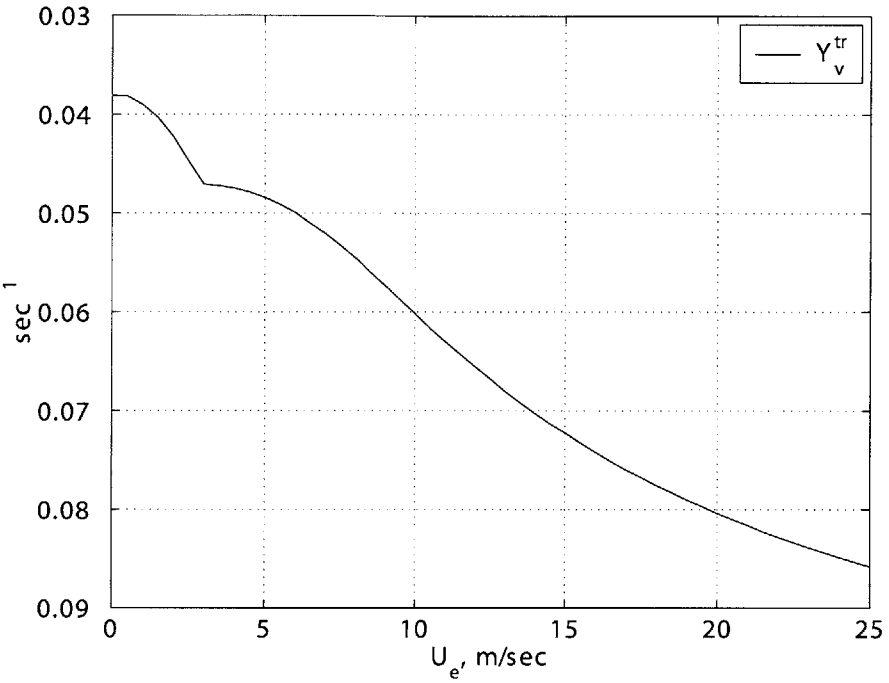

Figure 3-7: Linearized tail rotor sideforce due to side velocity

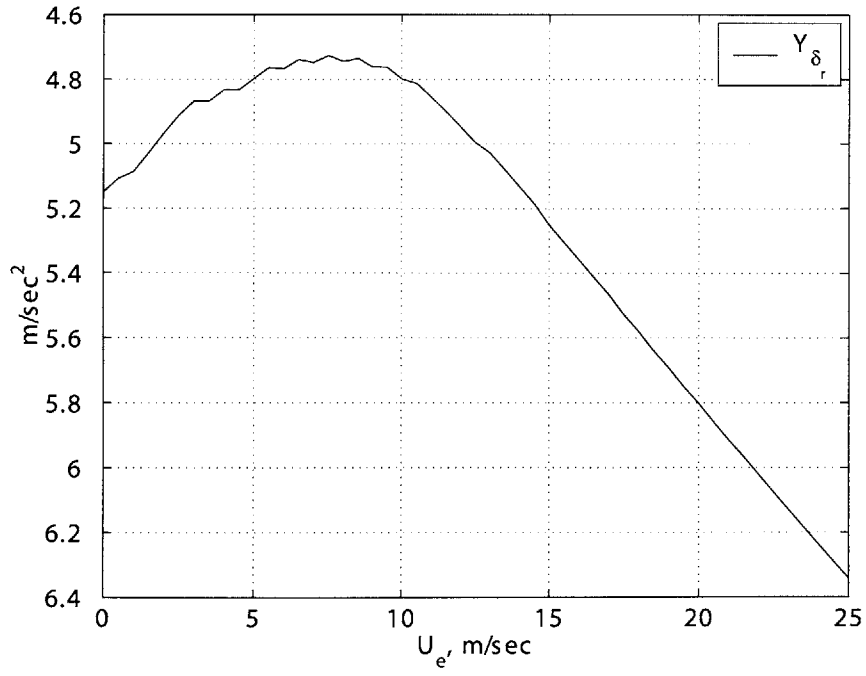

Figure 3-8: Linearized tail rotor sideforce due to tail rotor pitch

In both of these cases $K_\lambda = 0$. The tail rotor is fully in the wake if:

$$\frac{u_a}{V_{imr} - w_a} \geq g_f \tag{3.48}$$

In the far wake the downwash is twice the value at the rotor. We assume that $K_\lambda = 1.5$ when the tail rotor is fully immersed. In the remaining case, when the tail rotor is partially immersed, we assume a linear growth of the wake intensity factor with the forward speed:

$$K_\lambda = 1.5 \frac{\frac{u_a}{V_{imr} - w_a} - g_i}{g_f - g_i} \tag{3.49}$$

The derived expression is used to calculate the vertical component of airspeed at the tail rotor location, as shown in Eq. (3.37). Next, determine an advance ratio for the tail rotor:

$$\mu_{tr} = \frac{u_a^2 + w_{tr}^2}{\Omega_{tr} \cdot R_{tr}}$$

Velocity component normal to the tail rotor is given by:

$$v_{tr} = v_a - l_{tr} \cdot r + h_{tr} \cdot p$$

and in nondimensional form:

$$\mu_{z_{tr}} = \frac{v_{tr}}{\Omega_{tr} \cdot R_{tr}}$$

The magnitude of the resulting tail rotor thrust is limited based on the assumed maximum thrust coefficient to model stall of the blades and other viscous losses.

$$\begin{aligned} Y_{max}^{tr} &= f_t C_{T_{max}}^{tr} \rho \left(\Omega_{tr} R_{tr}\right)^2 \pi R_{tr}^2 \\ |Y_{tr}| &\leq Y_{max}^{tr} \end{aligned}$$

The yawing and small rolling moments due to offsets from the c.g. are computed as follows:

$$\begin{aligned} N_{tr} &= -Y_{tr} l_{tr} \\ L_{tr} &= Y_{tr} h_{tr} \end{aligned}$$

We need to compute the tail rotor induced velocity, used in the calculation of the vertical fin side force (see Eq. (3.36)). Using the same derivation as for the main rotor [44, pp. 115-123], the inflow ratio is approximated by Eq. (3.50).

$$\lambda_0^{tr} = \mu_{z_{tr}} - 2 \left[\frac{2C_T^{tr}}{a_{tr} \sigma_{tr}} - \delta_r \left(\frac{1}{3} + \frac{\mu_{tr}^2}{2} \right) \right] \tag{3.50}$$

where C_T^{tr} is the computed tail rotor thrust coefficient, a_{tr} is the tail rotor blade lift curve slope given in Table 3.1, $\sigma_{tr} = \frac{2c_{tr}}{\pi R_{tr}}$ is the tail rotor solidity ratio.

Finally, the tail rotor torque Q_{tr} is computed similarly to Eq. (3.11) and (3.12) using the tail rotor parameters in place of the main rotor parameters.

3.5 Actuator models

The command ranges for the cyclics and collective blade pitch are symmetric around the center point. The tail rotor blade pitch is offset by the trim value given in Table 3.1, such that the tail rotor pitch is computed as

$$\delta_r = \delta_r^{cmd} + \delta_r^{trim} \tag{3.51}$$

The following maximum commanded deflections were set, in radians:

$$\begin{aligned} \delta_{lat}^{max} &= 0.096 \\ \delta_{lon}^{max} &= 0.096 \\ \delta_{col}^{max} &= 0.183 \\ \delta_{r_{cmd}}^{max} &= 0.38 \end{aligned}$$

Here δ_{lat}^{max} and δ_{lon}^{max} are actual maximum cyclic pitch angles of the main rotor blades, measured statically. The gearing between servos and pitch angles of control surfaces is close to being linear. Linear functions are used to relate servo pulsewidth commands to control surface deflections. Look up tables can be used for a different gearing. Hobby servos and pulsewidth generation electronics used on the helicopter result in significant quantization effects. On average 150 steps were used to encode rail-to-rail deflection of each control surface. This results, for example, in a tail rotor command quantization of 0.3 degrees. Linear transfer functions are used to model the servo dynamics. Futaba S9402 servos, used for collective and cyclic deflections of the main rotor blades, were subjected to small-amplitude frequency sweeps under 35 oz·in mean load and small inertia, which we assume is representative of the actual loads experienced by the servos during the flight. The following transfer function came up as a result:

$$H_{servo}(s) = \frac{s/T_z + 1}{s/T_p + 1} \frac{\omega_n^2}{s^2 + 2\zeta\omega_n s + \omega_n^2}$$

where $T_z = 104$ sec, $T_p = 33$ sec, $\omega_n = 36$ rad/sec, and $\zeta = 0.5$. Note that 90 deg phase lag occurs at roughly 30 rad/sec, which also imposes a limitation on the control system bandwidth. A fast digital servo (Futaba S9450) was used for the tail rotor pitch. Since the torque required from the tail rotor servo is much lower than that required from the swashplate actuators, no-load small-signal bandwidth tests provide an adequate model of the servo. As a result of the tests, the servo transfer function was approximated by a second order system with the undamped natural frequency of 7 Hz and the damping ratio of 0.6.

3.6 Sensor models

3.6.1 Inertial measurement unit

The vast majority of unmanned helicopter control systems use angular rate gyros and accelerometers, with a notable exception of GPS-only control system developed at Stanford University. These sensor readings may include additional lags in the feedback path. The lags are due to analog anti-aliasing filters and suspension system dynamics [47]. A soft suspension system with the center of gravity of the suspended assembly offset from the

elastic center may introduce substantial coupling. The frequency response of antialiasing filters and suspension system can be easily measured. The suspension system rotational dynamics was modeled by decoupled second order transfer functions to accurately represent the resonant modes, which may lead to gain margin deficiency. In the case of the MIT X-Cell helicopter the translational and rotational modes are largely decoupled, and translational resonant frequencies are in the range of 13-18 Hz. The rotational resonant frequencies are: 12.5 Hz in roll, 9.2 Hz in pitch and 9.5 Hz in yaw. The frequencies of the suspension system resonances represent a tradeoff between the vibration isolation requirements, which dictate low frequency resonance, and the requirement for low interference with the rigid body dynamics, which demands high frequencies. The translational dynamics of the helicopter is at least an order of magnitude slower than translational dynamics of the suspension system. On the other hand, rotational dynamics of the helicopter contains modes with natural frequencies of 2-3 Hz (coupled rotor-fuselage pendulum-like mode), which necessitates the modeling of the box rotational dynamics. Note that the rotational box movements relative to the airframe introduce reciprocal moments on the helicopter. However, moments of inertia of the box are two orders of magnitude less than the moments of inertia of the airframe, therefore the reciprocal moments were neglected.

In the case of X-Cell the lowest vibration frequency related to the main rotor is 1 per rev, around 27 Hz. Neoprene isolators were used, which have very low damping ratio (about 0.05), ensuring rapid 40 dB/decade attenuation at the cost of resonance peak amplification factor of 10. For example vibratory input at the 1 per rev frequency in yaw is attenuated by a factor $(27/9.5)^2 = 8$. Additional attenuation of the vibratory input in the measured signal is provided by the first-order analog antialiasing filters with the cut-off set at 9 Hz. In hindsight, the cutoff frequency of the antialiasing filters was chosen unnecessarily low, 20 Hz cutoff would be sufficient to avoid aliasing.

In addition, accelerometer measurements are different from the center of gravity accelerations due to the IMU offset from the c.g.

$$\overline{a}_m = \overline{a}_{cg} + \overline{\omega} \times \overline{\omega} \times \overline{R}_m + \dot{\overline{\omega}} \times \overline{R}_m \tag{3.52}$$

where $\overline{R}_m$ is a vector representing IMU offset from center of gravity in body axes. This vector was determined from the flight data, and is given here in meters: $\overline{R}_m = \begin{bmatrix} 0.07 & 0.025 & 0.11 \end{bmatrix}^T$. The term $\overline{\omega} \times \overline{\omega} \times \overline{R}_m$ containing cross products of angular rates is small, while the term $\dot{\overline{\omega}} \times \overline{R}_m$ involving the derivatives of angular rates contributes substantially to the accelerometer measurements during maneuvers involving rapidly changing angular rates, e.g. frequency sweeps. Note that in Eq. (3.52) $\overline{\omega}$ and $\dot{\overline{\omega}}$ represent vectors of angular rates and angular accelerations of the suspension assembly.

To use the accelerometer readings in modeling, this term should be estimated using pseudoderivatives of the measured angular rates, and subtracted from low-pass filtered accelerometer measurements. Appropriate choice of time constant would result in a near cancellation of the effect.

Both accelerometers and gyroscopes are subject to drift, which is driven primarily by temperature variations and vibration. The drifts can be modeled as random walks or first-order Markov processes. Quantitative characteristics are sensor specific, and can be inferred from manufacturer specifications and flight tests.

3.6.2 Global Positioning System Receiver

A low-latency, high update rate GPS receiver is needed for high-bandwidth helicopter control. The receiver used on the helicopter has 50 millisecond latency, and 10 Hz update rate. Other sources of error include multipath, ionospheric and tropospheric delays, satellite and receiver clock drifts, etc. As a rough approximation, these can be represented by white Gaussian noise, with the standard deviation values determined by ground tests.

Another key requirement for GPS receivers used onboard autonomous aerobatic helicopter is a fast reacquisition time. The helicopter inevitably loses track of satellites during inverted flight, dead-reckoning is used to estimate helicopter position and velocity until satellite tracking is reacquired. A common hot reacquisition time is 3 seconds, sufficiently low to maintain adequate state estimate with dead-reckoning.

3.6.3 Barometric altimeter

Pressure altimeter provides an accurate source of sea-level altitude information out of ground effect. Important sources of error are sensor quantization and measurement noise. We used a high-end altimeter with 10^{-3} psi (0.6 meters) resolution. The measurement noise was assumed to be white Gaussian with a standard deviation of $6 \cdot 10^{-4}$ psi.

Chapter 4

Control system design for autonomous aggressive maneuvering

4.1 Control approach and autopilot modes

Aerobatic flight can be broken down into two distinct flight regimes: following trim trajectories between the maneuvers, and the maneuvers themselves. Between the maneuvers, the pilot uses fine adjustments to maintain or gradually transition between equilibrium trajectories, characterized by forward speed, sideslip angle, climb rate and turn rate. This flight regime is adequately described by linear models, and can be automated using control design methods developed for linear time-invariant systems. Aerobatic portion of the flight imposes a special demand on these trim-trajectory controllers: fast recovery from aggressive maneuvers must be assured. During the development and initial testing phase of the logic for autonomous aerobatics the vehicle may end up in an unusual attitude and with an exceedingly fast forward speed. The trim trajectory controllers represent an essential line of defense in such circumstances. Manual takeover of control by an R/C pilot is the last resort, which may still be unable to recover the vehicle in extreme situations due to pilot's disorientation and lagged reaction time. Since the pilot is not actively controlling the helicopter during an autonomous flight, there is a lag, or an adjustment period, required for the pilot to assess the situation and fully regain control in case of emergency.

Among different linear control design methodologies, the linear quadratic regulator (LQR) provides a degree of robustness to plant uncertainties for systems with full-state feedback [1], and results in easily implementable low-order controllers. Based on flight experiments, longitudinal-vertical and lateral-directional dynamics of the X-Cell in low advance ratio flight (up to $\mu = 0.15$) are sufficiently decoupled [16, 17] to design separate feedback controllers. The LQR approach was adapted for trim trajectory control of the helicopter (see Sections 4.2 and 4.3). Since helicopter dynamics changes significantly between hover and forward flight, the gains were scheduled with forward speed; a novel gain scheduling scheme was utilized (see Section 4.3). Flight tests have demonstrated fast response of the resulting closed loop system, and reliable recovery from the maneuvers.

Maneuvering portion of the flight requires large control inputs. The vehicle state variables, such as angular rates, attitude, and speed, undergo large and rapid variations. A linear model can not adequately describe full vehicle dynamics during aerobatic maneuvers.

During some segments of aerobatic maneuvers the vehicle is uncontrollable in the system-theoretic sense. For example, if the vehicle is banked 90 degrees it can not maintain its altitude. These factors make it difficult, or impossible, to track aerobatic state trajectories with linear control design methods, or with approaches based on feedback linearization.

Frazzoli [12] suggested a nonlinear control design method for helicopters based on a so-called backstepping approach. The central idea in the method is to determine desired main rotor thrust and orientation based on translational commands (velocity or position), and then use the control moments to orient the rotor in the desired direction. The tail rotor thrust is used primarily to counteract the main rotor torque. Using an idealized helicopter model, and a novel representation of attitude error, a control Lyapunov function was constructed for a particular controller, which featured an explicit cancellation of the nonlinear terms with control moments, and proportional-derivative controllers for attitude and position. For the simplified model used, the method was theoretically proved to provide tracking controllers for a wide class of trajectories, including aggressive trajectories involving extreme attitude angles. The mathematical model used for design and evaluation of this controller relied on a number of unrealistic assumptions: exact knowledge of the tail rotor torque and moments of inertia, and instantaneous application of precisely known control moments. While the design approach in its current state is probably not applicable to a real helicopter, the approach may potentially be modified to yield a practical control design method for tracking aerobatic trajectories.

A different approach to autonomous execution of aerobatic maneuvers was used by the author. It was inspired by the observed human pilot's strategy [14]. Based on the input and state time histories recorded during a series of manual aerobatic maneuvers, we made the following observations: each particular type of maneuver is largely repeatable; the pilot uses few continuous feedbacks during the maneuvers; most of the pilot's actions can be described by piece-wise constant or piece-wise linear functions, with the switching times determined by the vehicle attitude. To illustrate the above, consider state and control time histories for multiple axial roll maneuvers, given in Figure 4-1.

During the maneuver, the pilot is using the lateral cyclic and collective pitch control inputs. Proportional yaw rate feedback to the tail rotor pitch is always active during the maneuver. We can see that the commands are either held constant, or changed as linear functions of time. The time for ramp-up or ramp-down of the commands varies between 0.2 and 0.4 seconds. It appears that as soon as the pilot made a decision to change the control input, he performs it in a feedforward fashion, with no apparent continuous feedback. The length of ramp periods is related to a human's neuromuscular response time, which is generally on the order of 0.2 seconds. A pilot probably would not use faster, more step-like commands even if he could, to avoid exciting the lightly damped pendulum-like modes, described in Section 3.4.1, which would put extra stress on the airframe. A question arises, what triggers the command transitions between various portions of the piece-wise linear profiles? At the start of the maneuver, the pilot ramps a particular command to the desired level (e.g. maximum lateral cyclic at the start of an axial roll). Both the level and the time of the ramp are highly repeatable. It is thus reasonable to assume that this portion is entirely feedforward, an automatic movement of the fingers. By analyzing the timing of the start of the ramp down of the lateral cyclic command, we observed that it correlates highly with the bank angle, i.e. the ramp down starts when the helicopter is about 50 degrees away from being level. This matches well the instructions given in handbooks for aerobatics [8]. An analysis of the use of the cyclic and tail rotor commands in other maneuvers (split-S,

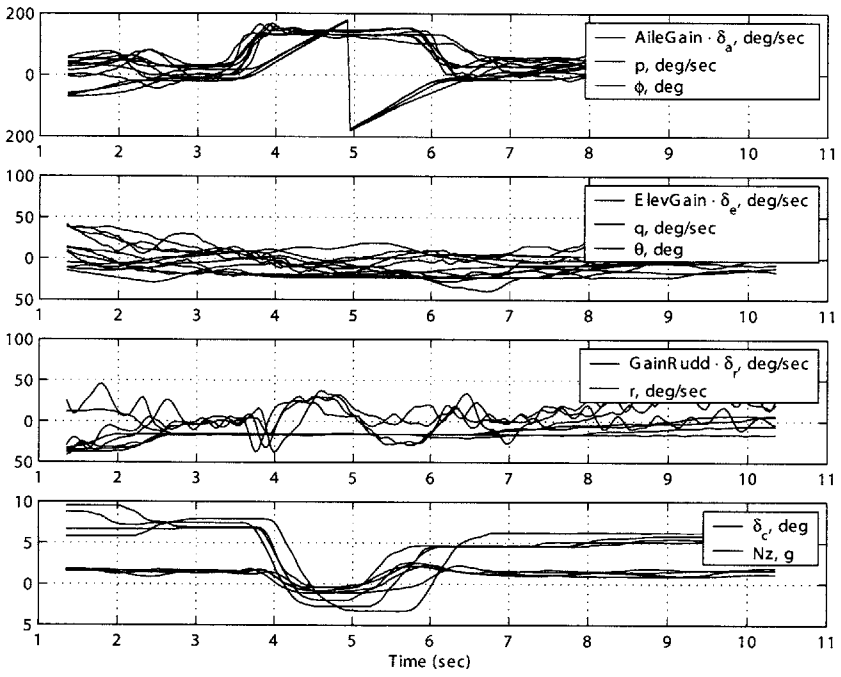

Figure 4-1: Recorded state and input time histories for multiple axial roll maneuvers. The variables of interest are the pilot lateral cyclic control (δ_a), the helicopter roll angle (ϕ), and the pilot collective controll (coll)

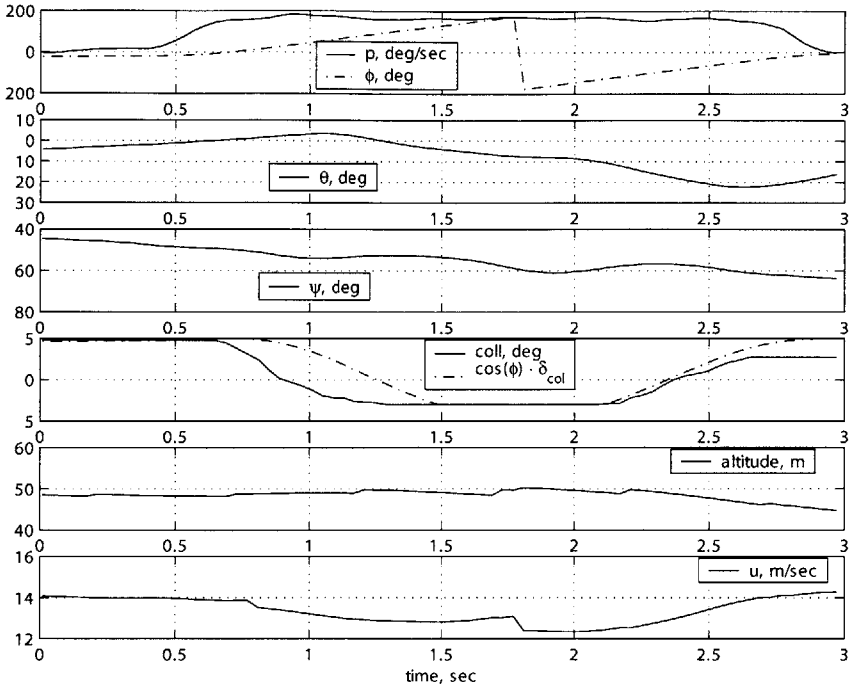

Figure 4-2: Recorded state trajectory during a manual axial roll

hammerhead, loop) shows the same pattern: an attitude-based discrete feedback is used to switch the commands between different portions of piece-wise linear patterns.

In Figure 4-1 we can see that the collective modulation, while also seemingly piece-wise linear, is somewhat less repeatable than the cyclic commands. The timing of the collective command is critical for maintaining altitude and minimizing course changes during the maneuver. Conceivably, by trial and error, the pilot would find a pattern which results in a particularly clean maneuver, and make it repeatable. A good candidate for collective modulation law during aggressive maneuvers can be inferred from the following physics-based reasoning. A trim thrust level is desired during an upright flight (0 degree roll angle), negative thrust of a similar magnitude during an inverted flight (180 degrees), and no thrust is needed when the rotor disc is perpendicular to the horizon (90 and 270 degrees). A cosine function of bank angle meets these conditions. One can assume that the pilot unconsciously tries to approximate the cosine function of bank angle with a piece-wise linear function of time. Figure 4-2 shows the state and control trajectories for a relatively cleanly executed axial roll (small altitude loss, albeit some heading change). Notice the similarity between the actual collective command and a signal proportional to the cosine of bank angle. This physics-based collective modulation law seems applicable to other maneuvers as well: the goal seems to be to modulate the main rotor thrust as a cosine of the angle between the local vertical and body Z-axis.

Despite an apparent simplicity of the pilot's strategies for maneuver execution, recreating them in a completely open-loop fashion (except for the yaw rate feedback, which is a must) can not provide consistent trajectories. The helicopter is an unstable dynamic system, and disturbances will change the trajectories between the runs. The pilot may be making some fine adjustments in the proposed command framework (e.g. in the length of

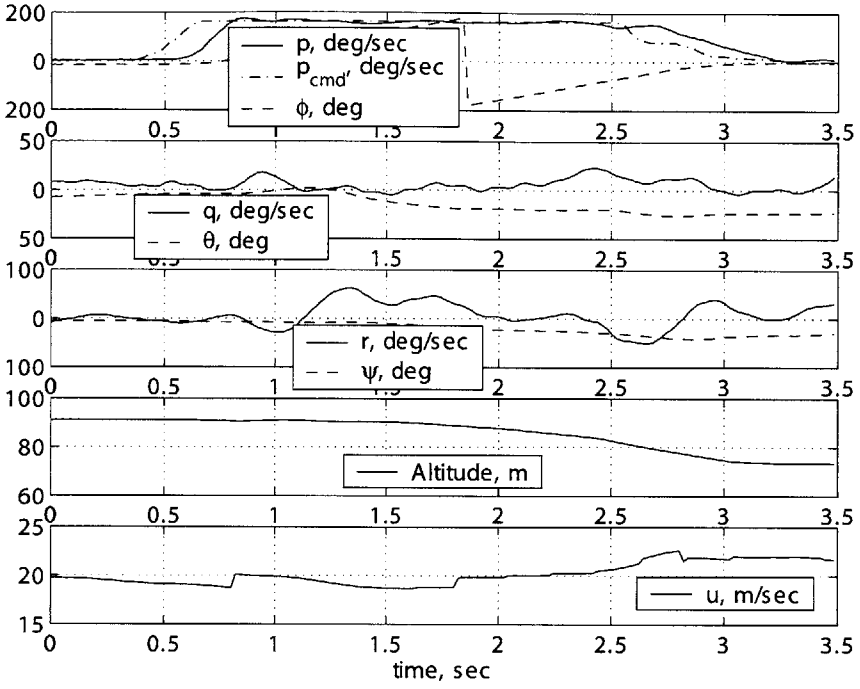

Figure 4-3: Recorded state trajectory during an axial roll with rate tracking controllers

the ramp intervals, levels of commands), which yield a better repeatability of trajectories and a safe execution of the maneuvers.

The desired feedback structure was provided by the angular rate tracking controllers. From the pilot's perspective, a helicopter with a hingeless rotor feels like a rate control system (as opposed to articulated rotors, where the pilot effectively controls angular accelerations with cyclic actuators). We have found that the pilot's strategy remains unchanged when a tight angular rate control augmentation system was used. In this case, the pilot commanded roll, pitch and yaw rates, and collective angle. Compare Figure 4-3, showing the state and control time histories for an axial roll performed with the rate command system, and those for an open-loop execution in Figure 4-2.

Figure 4-4 further illustrates the approximation of the pilot's rate commands with piecewise linear functions. As can be seen, the ramp-up and ramp-down times are on the order of 0.2-0.4 seconds. As is typical for the axial roll maneuver, the ramp down starts when the bank angle reaches -50 degrees (for a roll to the right). Finally, we can see the closed-loop roll rate response is similar to the open loop response from the pilot's perspective: it has a fast rise time (≈ 0.2 sec), and a second-order characteristic, although it is better damped.

The rate tracking loops were single-axis proportional-integral controllers. Notch filters on cyclic commands were used to attenuate the lightly damped fuselage-rotor modes [40] and permit higher controller bandwidth. The pilot performed a number of maneuvers with the rate command system instead of the open-loop commands. The resulting angular rate trajectories for several maneuver types were approximated with piece-wise linear functions, and specific attitudes for switching rate commands were inferred by superimposing the rate commands and attitude time histories. The resulting rate command trajectories were implemented in software as simple state machines. These approximations served as the

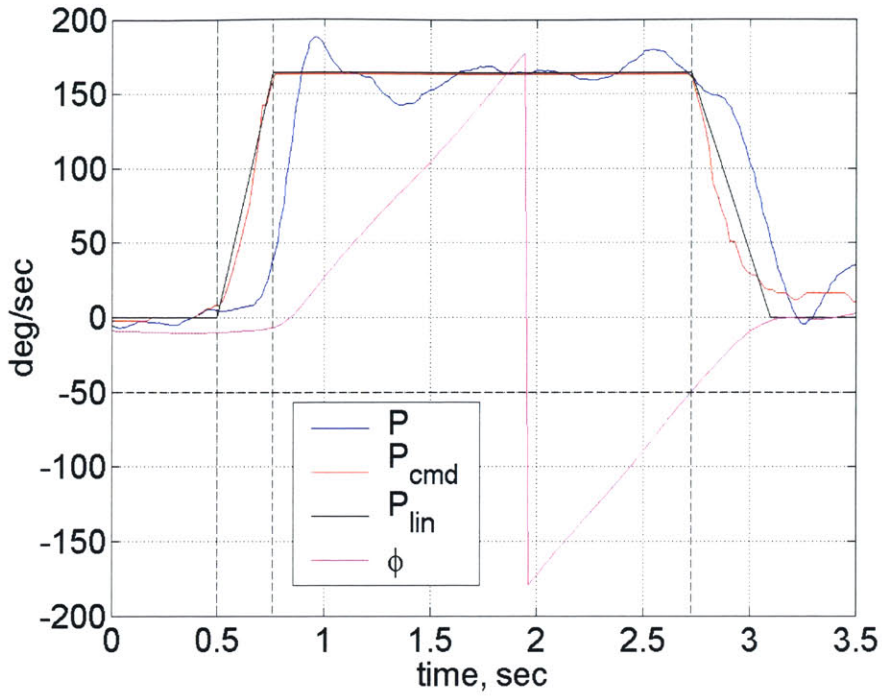

Figure 4-4: Comparing pilot rate command with a piece-wise linear approximation

reference commands for the angular rate tracking loops during completely autonomous execution of the maneuvers. Examples of these commands for several maneuvers are given in Section 4.4. This method relies on a close tracking of the angular rate commands, which is possible for a miniature helicopter with a hingeless rotor, featuring quick response and large control power of the cyclic actuators.

To facilitate with the flight testing of the described control laws, we developed several flight control modes, shown in Table 4.1. A regular two-stick R/C transmitter unit is used to uplink pilot commands to the flight control computer. In the "manual" mode the pilot commands the main rotor collective and cyclic pitch deflections on the transmitter sticks, as well as a setpoint for a yaw rate feedback controller. In the "rate tracking" mode the pilot commands all three angular rates and the collective pitch. In the "velocity/heading rate command - altitude hold" (VHRCAH) mode the pilot commands turn rate, forward, side and vertical velocities (the operator has an option to engage altitude hold). In the "hover hold" mode the helicopter maintains GPS position, pressure altitude, and heading. Finally, the pilot can initiate a pre-programmed sequence by activating a switch on the remote-control transmitter. The sequence can include either a single aerobatic maneuver or an aerobatic routine, where the helicopter follows selected GPS waypoints, performs aerobatic maneuvers at specified locations, and returns to hovering flight at the starting point.

The first flight test of each of the automatic maneuvers proceeds as follows: (1) the pilot takes off manually, and engages the "velocity/heading rate command/altitude hold" mode at a safe maneuver altitude; (2) the pilot commands the forward speed setpoint used for the maneuver execution (12 and 15 m/sec were used). From that point the helicopter is flown with a single left sideways stick - turn rate (or, equivalently, bank angle) command. The autopilot maintains the altitude and forward speed setpoints. (3) After performing a

number of turns to attain the desired course and position, the pilot brings the helicopter to level flight by commanding zero turn rate (releasing the spring-loaded stick). (4) He then engages an entirely automatic maneuver sequence by a switch on the R/C transmitter. The helicopter performs the maneuver, and exits the sequence at a close to level attitude and practically zero angular rate. (5) At this point the controller automatically goes back to the "velocity/heading rate command/altitude hold" mode. The altitude hold acquires a new setpoint, and the forward speed returns to the selected speed setting.

Table 4.1: Autopilot Modes for MIT X-Cell Helicopter

	Manual	Rate Tracking	VHRCAH	Hover hold
Longitudinal	Lon. Cyclic	Pitch rate	Forward velocity	Position
Lateral	Lat. Cyclic	Roll rate	Side velocity	Position
Directional	Yaw rate	Yaw rate	Turn rate	Heading
Vertical	Collective	Collective	Altitude/rate	Altitude

4.2 Longitudinal-vertical trim trajectory controller

The command variables are the body-axis forward and inertial vertical velocities. The pilot commands forward speed in the range of -2 to 15 m/sec by fore-aft deflections of the left stick on the remote control (this stick is used to command collective pitch in the "manual mode"). The stick is not spring-loaded, and the pilot uses it as a trim setting for velocity hold, without actively controlling the speed. Longitudinal deflections of the spring-loaded right stick are used to command altitude rate or to engage altitude hold. This command structure allows changes in speed and altitude, and at the same time relieves the pilot of the tasks of controlling vertical and longitudinal channels for most of the flight.

4.2.1 Linearized longitudinal-vertical dynamics

A linear model of the longitudinal-vertical dynamics was obtained by an analytical linearization of the nonlinear equations of motion around a steady turning flight at a constant altitude.

The state vector of perturbations from the trim conditions is $X_{lon} = \begin{bmatrix} u & a_1 & w & q & \theta \end{bmatrix}^T$, where u is the perturbation in the body axis forward speed from the trim speed U_e, a_1 is the longitudinal flapping angle of the main rotor, w is the body Z-axis velocity, q is the pitch rate and θ is the pitch angle. The vector of control input perturbation values is $U_{lon} = \begin{bmatrix} \delta_{lon} & \delta_{col} \end{bmatrix}^T$, where δ_{lon} is the longidutinal cyclic pitch, and δ_{col} is the collective pitch of the main rotor blades. The equations of motion are:

$$\begin{aligned}
\dot{u} &= X_u (u - u_w) - \frac{g}{\cos \Phi_e} a_1 - U_e \tan \Theta_e q - g \cos \Theta_e \theta \\
\dot{a_1} &= \frac{1}{\tau_e} \frac{\partial a_1}{\partial \mu} \frac{u - u_w}{\Omega R} - \frac{a_1}{\tau_e} + \frac{1}{\tau_e} \frac{\partial a_1}{\partial \mu_z} \frac{w - w_w}{\Omega R} - q + \frac{K_{\delta_{lon}}}{\tau_e} \delta_{lon} + \frac{1}{\tau_e} \frac{\partial a_1}{\partial \delta_{col}} \delta_{col} \\
\dot{w} &= Z_u (u - u_w) + Z_w (w - w_w) + \left(Z_q^{h_t} + U_e \right) q - g \cos \Phi_e \sin \Theta_e \theta + Z_{col} \delta_{col} \quad (4.1)
\end{aligned}$$

$$\begin{aligned}\dot{q} &= M_{a_1} a_1 + M_w^{h_t} (w - w_w) + M_q^{h_t} q \\ \dot{\theta} &= \cos\Phi_e q\end{aligned}$$

Here Φ_e is the trim value of the bank angle; Θ_e - the trim pitch angle, which is determined by the trim solution, ΩR is the main rotor blades tip speed, u_w and w_w are projections of wind speed on body axes. Aerodynamic coefficients, or stability and control derivatives, are obtained by linearization of the nonlinear model near the selected equilibrium point, e.g. $X_u = \frac{1}{m}\frac{\partial X(U_e,\Phi_e)}{\partial U}$. The effective time constant of rotor flapping τ_e is determined by the stabilizer bar aerodynamic and inertial properties [17, 37].

4.2.2 Model reduction for control system design

We based the control system design for trim trajectory tracking on a linear quadratic regulator, which provides excellent robustness properties when a measurement of the full state vector is available [1, 32]. When full state vector is not available, an estimator with a significantly higher bandwidth than the open-loop plant dynamics is known to provide good robustness properties in practice. Forward velocity, ascent rate, pitch angle and pitch rate can be either measured or reasonably accurately estimated in real-time, either by an extended Kalman filter or a combination of complementary filters [47]. Note that the EKF described in Section 2.3 relies on a kinematic model rather than on a full dynamic model of the helicopter, which, intuitively, mitigates the loss of robustness of the closed loop system to modeling errors.

Rotor flapping angles are difficult to measure. We decided to use a rigid body approximation of the longitudinal-vertical dynamics. However, the flapping state participates in a lightly damped fuselage-rotor coupling mode [40, 37]. We used a notch filter on the longitudinal cyclic to eliminate potential gain margin problems with the controller design based on the reduced-order model [38, 44]. With the notch filter the attitude rate dynamics can be approximated by a first order transfer function [38] (Fig. 4-5), which corresponds to a quasi-steady rotor flapping dynamics. The reduced 4^{th} order dynamics should then approximate the plant with the notch filter on the longitudinal cyclic. The equations of motion for the reduced order model can be obtained by replacing the differential equation for the flapping state with an algebraic relationship.

Additional stability derivatives will arise in the process. The effective rate damping due to the main rotor M_q^{mr} can be derived from the quasi-steady approximation, however it would result in a significant phase lead compared to the actual cyclic-to-rate transfer function augmented with the notch filter. Therefore, the damping derivative M_q^{mr} was chosen to match the frequency at which the notched plant achieves 45 degree phase lag [38], as shown in Figure 4-5. The longitudinal cyclic control derivative $M_{\delta_{lon}}^{mr}$ was chosen to produce the same steady state response from the pitch cyclic to the pitch rate as the original plant.

4.2.3 Control system design

To guarantee zero steady state error in tracking forward speed and altitude rate the reduced order state vector was augmented with the integrators, which resulted in a new 6-dimensional state vector and corresponding state and control matrices. The equation for the integral of the forward speed error is:

$$\dot{u}_i = u^{cmd} - u \tag{4.2}$$

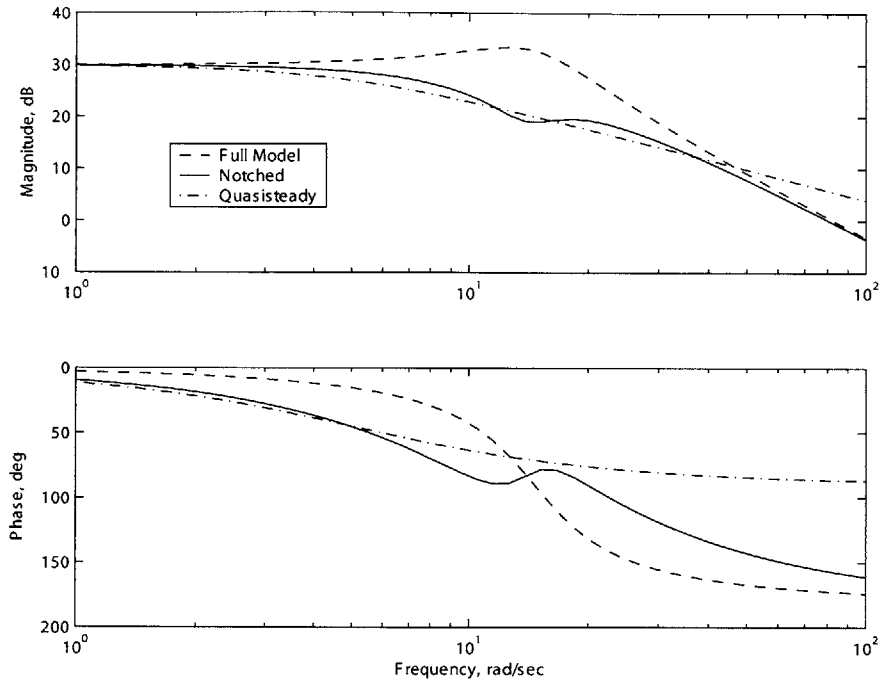

Figure 4-5: Longitudinal cyclic to pitch rate transfer function approximations

The linearized equation for the altitude rate integral error is

$$\dot{V}_{hi} = V_h^{cmd} - u\sin\Theta_e + w\cos\Theta_e\cos\Phi_e - \theta U_e\left(\cos\Theta_e + \frac{\sin^2\Theta_e\cos\Phi_e}{\cos\Theta_e}\right)$$

The feedback gains for this 6×2 system were calculated with a linear quadratic regulator approach. Diagonal Q and R matrices were used in the quadratic cost function.

$$J = \int_0^\infty \left(x^T Q x + u^T R u\right) dt \tag{4.3}$$

The controllers were designed for the following seven trim points: -3, 0, 3, 6, 9, 12 and 15 m/sec body axis forward speed. Linear interpolation was used to obtain the gains for intermediate forward velocities. All design cases were based on a trim bank angle of 45 degrees; which was the maximum commanded bank angle. Banked flight is more challenging for control design because collective control is less efficient in maintaining commanded vertical rate.

Based on simulation studies with the full model, which includes the flapping state and the notch filter, we eliminated several gains. To improve the transient response a feedforward from the forward speed command to the longidutinal cyclic was added. It was implemented as the pitch angle command proportional to the speed command: $\theta^{cmd} = G_1 \cdot u^{cmd}$. Two additional feedforward signals were used to facilitate the enforcement of kinematic constraints. In steady turns the aircraft must maintain body axis pitch rate, proportional to yaw rate:

$$q^{cmd} = r^{cmd}\tan\phi^{cmd} \tag{4.4}$$

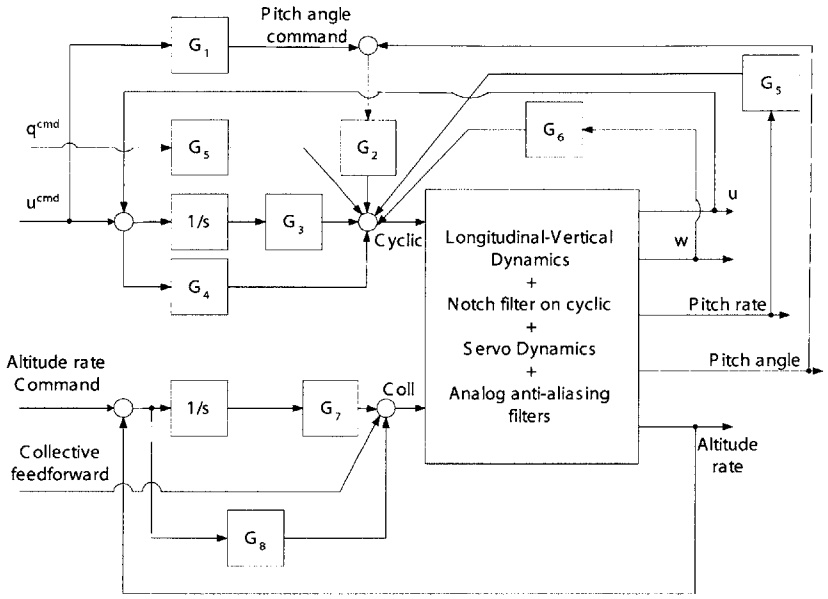

Figure 4-6: Longitudinal-vertical control architecture

The collective pitch was modified as a function of commanded pitch and bank angles to reduce altitude loss during rapid accelerations or hard banks:

$$\delta_{col}^{ff} = \frac{1}{2}\delta_{col}^{ss}\left(\phi_{cmd}^2 + \theta_{cmd}^2\right) \tag{4.5}$$

where δ_{col}^{ss} is the value of the collective angle low-pass filtered with a first order filter with 10 seconds time constant. Figure 4-6 shows the resulting control architecture.

The control laws were designed to the following specifications: the damping ratio of at least 0.5 for the two oscillatory modes with the frequencies of less than 10 rad/sec; rise time for the altitude rate step response of no more than 1 second; rise time for the forward speed step response of no more than 2.5 seconds. Bryson's rule [3] was used for initial guess of diagonal entries of Q and R weighting matrices, which were then tuned to conform to the above specifications. A constant-gain proportional controller was designed for the altitude hold. The requirement for the altitude hold was set to maximum ± 3 meter error during 45 degree banked turns.

The rate of change of the forward speed command was limited to -5 m/sec/sec for deceleration and to 2 m/sec/sec for acceleration to avoid rapid changes in the gains of the lateral-directional controllers, scheduled with forward speed.

Prior to flight tests the controllers were extensively tested in a hardware-in-the-loop simulation [47]. Flight testing showed that the longitudinal-vertical closed loop dynamics were predicted well by the simulation. Figure 4-7 shows the forward velocity and altitude time histories during rapid acceleration and deceleration maneuvers.

In the early version of the avionics package the forward velocity estimate was corrected by the GPS measurements that arrive once a second, with 1 second latency. We also found that there is an additional effective 0.3 second latency contributed by the internal

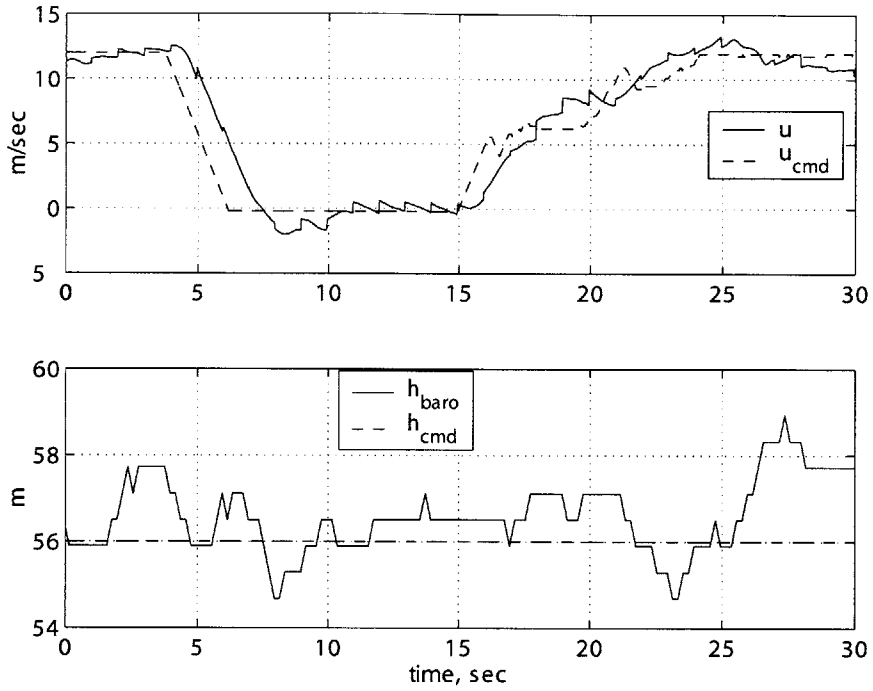

Figure 4-7: Forward velocity and altitude time histories during rapid acceleration and deceleration

estimator used in the particular GPS receiver we used originally. After compensation [47] this resulted in 1 m/sec jumps on average due to corrections. Pressure altitude is measured with a resolution of 2 feet. The pitch angle, estimated through gravity aiding, was within 5 degrees of the true value based on the estimate obtained in data post-processing. During this flight winds up to 10 knots were recorded. The control law experimentally proved to be robust to such measurement errors and disturbances.

4.3 Lateral-directional trim trajectory controller

We chose the yaw rate and the sideslip velocity as the command variables. The yaw rate command is mechanized as a turn rate command such that it acts as the yaw rate command at hover and as an effective bank angle command in forward flight. The control logic uses the tail rotor to turn at hover, and primarily the lateral cyclic in forward flight, utilizing the tail rotor for the turn coordination. The pilot commands turn rate by a sideways deflection of the right stick (lateral cyclic in manual mode), and side velocity by a sideways motion of the left stick (yaw rate command in manual mode). Both stick deflections are spring-loaded. During most of the flight the pilot uses a single left stick sideways motion to control turn rate of the helicopter in cruise flight, while the autopilot performs turn coordination, and maintains altitude and forward speed.

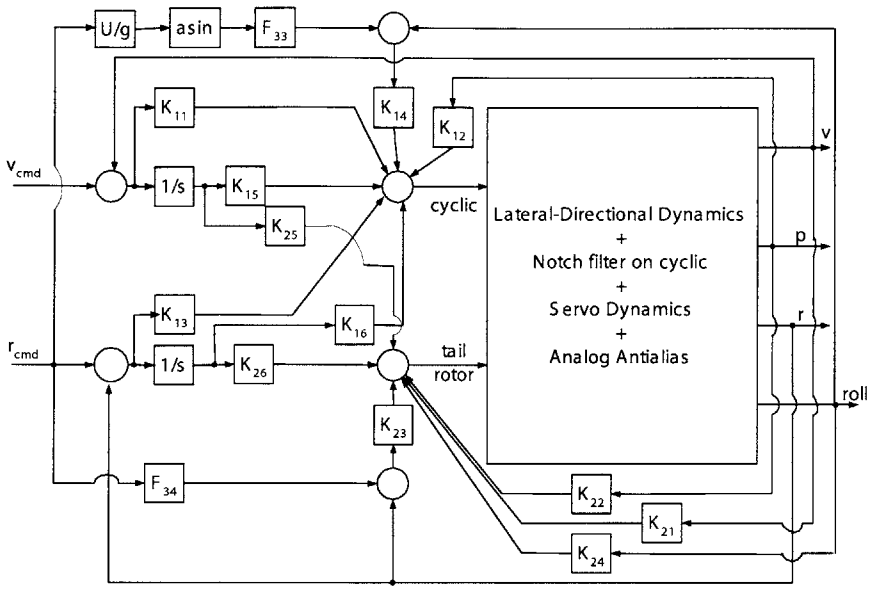

Figure 4-8: Lateral-directional controller structure

4.3.1 Linear model and control design

X-Cell's lateral-directional dynamics are adequately described by a linear model with five states and two inputs. The state vector is $x = \begin{bmatrix} v & b & p & r & \phi \end{bmatrix}^T$, where v is the side velocity, b is the lateral rotor flapping, p is the roll rate, r is the yaw rate, and ϕ is the roll angle. The control inputs are the lateral cyclic δ_a and the tail rotor pitch δ_r. The rotor torque variation due to collective pitch deflection δ_{col} leads to a change in yawing moment, and is treated as a disturbance. Another source of disturbance is wind side velocity v_w. The equations of motion are

$$\begin{aligned} \dot{v} &= Y_v (v - v_w) + g \cdot b + W_e p + (Y_r - U_e) r + g \cos(\Theta_e)\phi + Y_{\delta_r}\delta_r \\ \dot{b} &= -\frac{1}{\tau_e} b - p - B_\mu \frac{v - v_w}{\Omega R_{mr}} + \frac{B_{lat}}{\tau_e}\delta_a \\ \dot{p} &= L_b b + L_v^e (v - v_w) + L_r r + L_{\delta_r}\delta_r \\ \dot{r} &= N_v (v - v_w) + N_p p + N_r r + N_{\delta_r}\delta_r + N_{\delta_{col}}\delta_{col} \\ \dot{\phi} &= p + \tan(\Theta_e) r \end{aligned} \tag{4.6}$$

As in the longitudinal case, a notch filter on the lateral cyclic was applied to alleviate potential gain margin problems due to the lightly damped fuselage-rotor mode [38], and allowed the use of the rigid-body approximation for the design. Integrators were appended on the command variable tracking errors; LQ gains were computed for the resulting 6×2 system. The gains were designed for seven forward speed values from -3 to 15 m/sec.

The gain scheduling problem for the helicopter lateral-directional control system is challenging because several gains change drastically between the design points to accomodate the change in dynamics. At hover, it is natural to use the tail rotor pitch to effect the

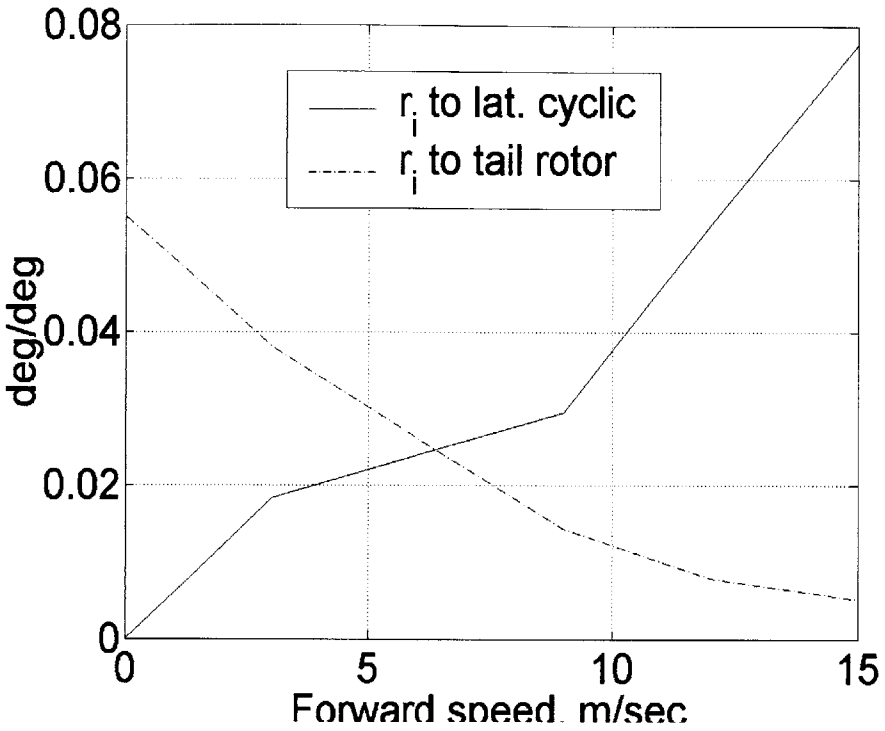

Figure 4-9: Lateral-directional gain variation with forward speed

change in turn rate, whereas in forward flight the lateral cyclic is used to achieve coordinated banked turn. This is reflected in the gain tables. At hover the feedback gain K_{26} (see Fig. 4-8 for controller diagram) from the integral of the yaw rate error (r_i) to the tail rotor pitch is large, while in forward flight this gain is small and the gain K_{16} from r_i to the lateral cyclic is large. If linear interpolation were used for gain scheduling, the look-up tables for these gains would be like the ones depicted in Figure 4-9.

Let us consider the effect of the rapid gain variation on lateral-directional response during a fast speed-up from hover. At hover, the integral of the yaw rate error (r_i) determines the trim offset of the tail rotor pitch (after multiplication by tail rotor pitch gain K_{26}). Since the cyclic gain (K_{16}) is small at hover, this state does not contribute appreciably to the cyclic trim offset. However when the helicopter accelerates, the cyclic gain grows very rapidly, which will lead to an undesired banking of the helicopter. Similarly, during a fast stop the helicopter will experience an unwanted yawing. These effects were observed both in simulation and in flight, when a linear interpolation was used for the gain scheduling.

To mitigate the undesired responses, we implemented a different gain-scheduling scheme. The controller gains were kept constant until a new design point velocity was reached; hysteresis logic was used to prevent limit-cycling. Continuity of the control surface commands during the gain switching (as well as during switching between different controller modes) was ensured by resetting the integrator states to appropriate values. This is possible when the control system has at least as many integrators as control surface inputs (equal number in this case). Let the vector of control surface commands be computed according to:

$$u = G_p x_p + G_i x_i \tag{4.7}$$

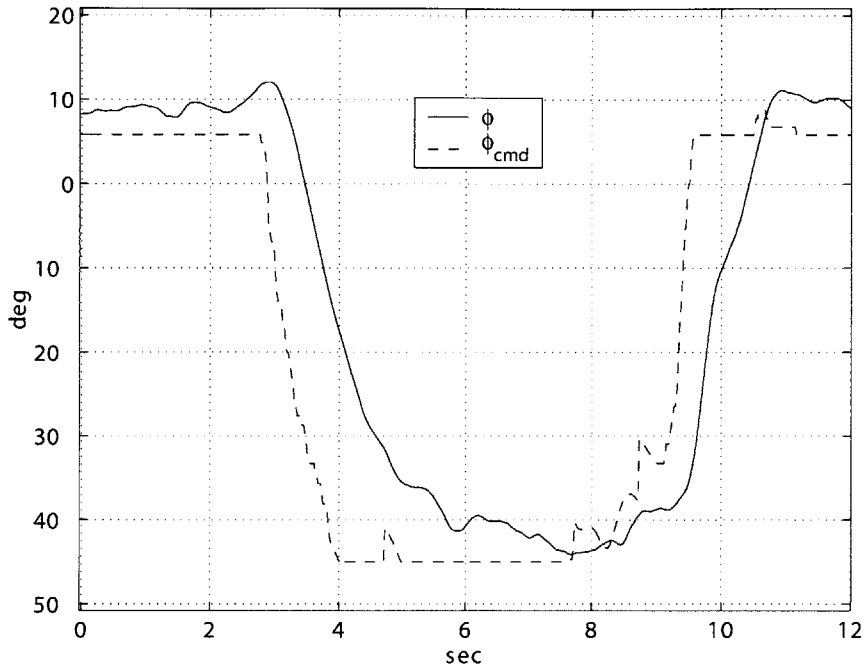

Figure 4-10: Bank angle response

where x_p are physical states, x_i are integrator states, G_p and G_i are the corresponding gain matrices. Then during the initialization of the control mode (or gain switching), the integrator states can be initialized as:

$$x_i = G_i^{-1}\left(u - G_p x_p\right) \tag{4.8}$$

where u is the last control input used by the previous control law before the switching. The discrete gain scheduling logic with hysteresis proved superior to a linear gain interpolation for rapid transitions between hover and forward flight, when several lateral-directional gains change by an order of magnitude or more to compensate for the change in plant dynamics. This makes the helicopter use appropriate control effectors for changing heading both in hover and in forward flight without any explicit mode switching required from the pilot. It is interesting to determine theoretical stability bounds for systems with such a gain-scheduling scheme.

The turn rate command was artificially limited to preclude a commanded bank angle above 45 degrees. The control laws were tested from hover to 15 m/sec forward flight; the pilot performed a number of 45 degree banks. Figure 4-10 shows recorded bank angle response to a commanded 45 degree turn. The controller is trying to minimize the yaw rate tracking error with an integral term, and drives the helicopter to a trim bank angle consistent with the demanded yaw rate, therefore this control structure does not require a highly accurate bank angle estimate, 5 degree errors proved acceptable.

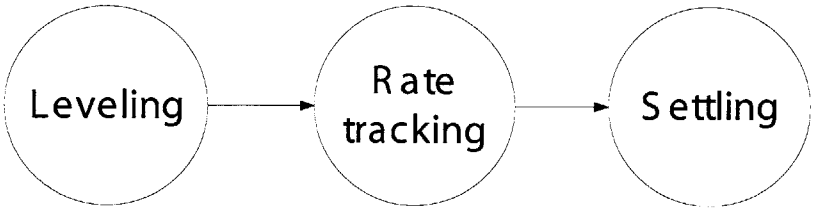

Figure 4-11: Phases of an autonomous aerobatic maneuver

4.4 Human-inspired logic for automatic maneuvering

The sequence for an autonomous maneuver execution, described in Section 4.1, requires switching from the trim trajectory tracking controllers to the maneuver control laws and back. In both cases the controllers have as many integrator states as control surfaces, therefore it is possible to initialize the integrator states such that the surface deflections are continuous, as described in Eq. (4.8). This logic enables smooth transitions between the modes.

Maneuver entrance and recovery are critical for successful implementation. To ensure similar entry conditions for maneuvers, we introduced a leveling phase, where decoupled proportional attitude controllers with inner loop rate feedback are used to bring the helicopter to an almost level attitude (within 3 degrees in roll and pitch by our choice). During this mode the yaw rate feedback is maintained, and collective angle is kept constant. Since attitude response is fast, this phase lasts for a short amount of time (less than half a second; for additional safety a timeout is used as well). Furthermore, the logic checks if the helicopter has sufficient speed and altitude to perform a maneuver.

To facilitate a safe recovery from the maneuver, the helicopter is allocated a settling time (chosen to be 2 seconds) in the trim-trajectory mode before it is allowed to proceed with another maneuver. It is interesting to investigate whether the state vector at the time of the exit belongs to the region of attraction of the trim trajectory tracking controller. Construction of a Lyapunov function for a simplified model with feedback controllers could provide an analytical assessment of safe exit states [12, 36].

Each maneuver is therefore defined as a sequence of three phases: leveling, following piecewise linear rate trajectories, and settling, as shown in Figure 4-11. This allows us to sequence one maneuver after another, as long as there is sufficient speed and altitude at the end of each settling phase. This capability was demonstrated in an autonomous airshow routine by performing a hammerhead maneuver immediately after a split-S. The duration of the settling phases can be evaluated in the simulation, and most likely can be reduced. This may be required for applications where a rapid sequence of the maneuvers is necessary.

Below we present the design of the reference trajectories for the axial roll and split-S maneuvers, and resulting flight test data for an autonomous execution of the maneuvers. In addition we describe a fully autonomous airshow routine, implemented as a state machine to demonstrate automatic transitions between various modes.

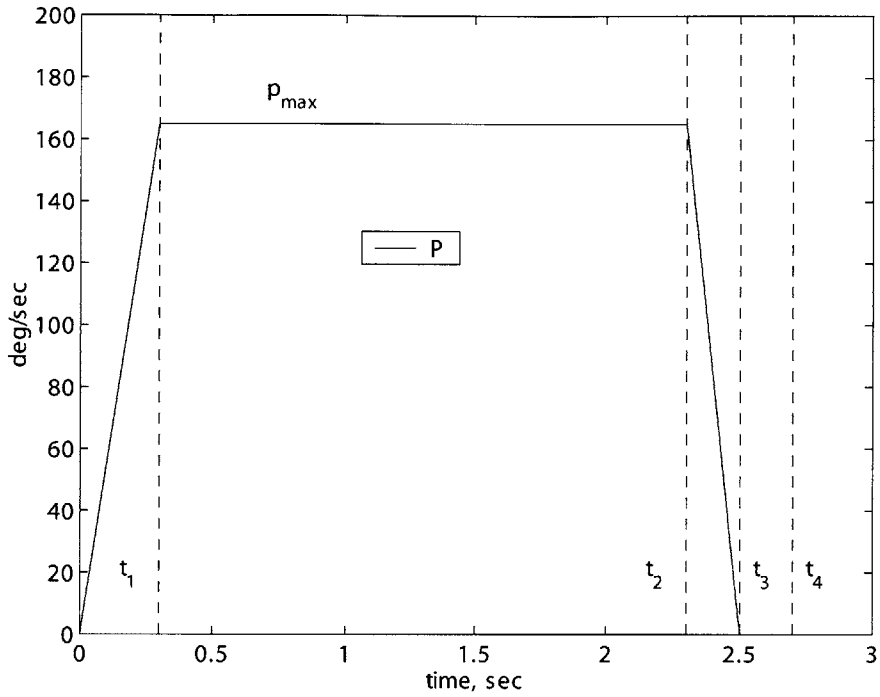

Figure 4-12: Reference roll rate trajectory for axial roll maneuver

4.4.1 Axial roll maneuver

The pilot's strategy for implementing the axial roll can be described as follows [14, 8]. Usually just prior to the maneuver the pilot slightly pitches up the helicopter to make use of the translational lift while inverted (note that the leveling phase during a fully autonomous execution plays the same role). To initiate the roll the pilot briskly ramps up the lateral cyclic to a full deflection, and modulates the collective roughly as a piece-wise linear approximation of a cosine of the bank angle; this keeps the thrust pointing up when the helicopter is upside down, and generates zero thrust when the main rotor disk is perpendicular to the horizon. When the helicopter reaches a specific attitude (≈ -50 degrees), the pilot brings the cyclic to neutral.

Based on these results, we generated reference trajectories for the angular rates. The pitch and yaw rate commands were set to zero throughout the maneuver. The roll rate trajectory, shown in Figure 4-12, approximated an actual trajectory during manual axial rolls: $t_1 = 0.3$ second linear ramp up to a maximum commanded value $p_{max} = 165$ deg/sec, next a constant command until the helicopter rotated by 310 degrees at time t_2, next a 0.2 sec linear ramp-down to zero commanded roll rate at t_3, followed by 0.2 seconds coasting time at zero roll rate command to stop the rolling motion after the maneuver (t_4). We decided not to use the Euler attitude angles during aerobatic maneuvers because of known singularities of this attitude representation in case the helicopter reached +90 or -90 degree pitch angle during a maneuver. We used an approximate roll angle obtained by integrating the body axis roll rate after the maneuver initiation. This approximate roll angle was used to determine the time of the ramp-down start, as described above. Alternatively, the condition for switching can be also defined as reaching proximity of a certain attitude. One

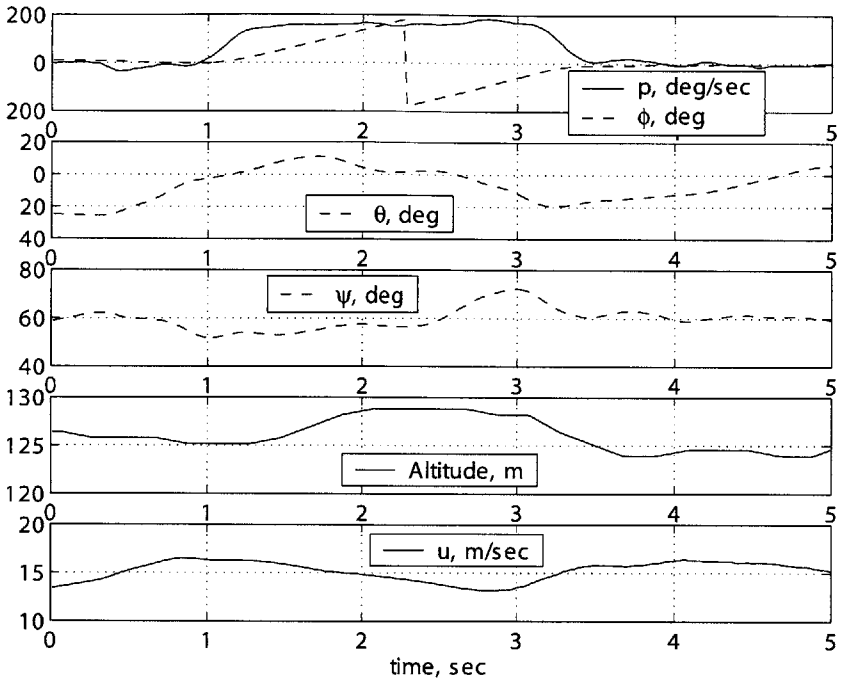

Figure 4-13: Recorded state trajectory during an autonomous axial roll

can utilize a measure of distance between the current and the target attitudes used by Bullo [4] and Frazzoli [12].

The collective pitch angle, which largely determines the rotor thrust, was modulated as cosine of the angle between the local vertical and body Z-axis. This strategy results in a profile that is close to the pilot's actions during the roll:

$$\delta_{col} = \max\left(\delta_{col}^{trim} \cdot \cos\phi\cos\theta, \delta_{col}^{\min}\right) \tag{4.9}$$

where δ_{col}^{trim} is the trim collective angle in forward flight. We limited the negative collective angle to $\delta_{col}^{\min} = -3$ deg (full travel is from -10.5 deg to 10.5 deg) to retain sufficient control authority during portions of the flight with negative rotor loading; this approach is also used by pilots.

Figure 4-13 shows the flight test data for an autonomous axial roll, which was part of the autonomous airshow sequence described below. Note that the changes of heading angle, speed, and altitude are small between the maneuver entrance and exit. These are the desired features for the axial roll maneuver.

4.4.2 Split-S maneuver

The same approach was used for an autonomous execution of an advanced aerobatic maneuver, a split-S, which consists of a half a roll immediately followed by half a loop. The yaw rate command is kept at zero during the entire maneuver. The roll and pitch rate commands are shown in Figure 4-14. Here the start of the roll rate ramp down t_2 and the pitch rate ramp down t_4 are determined by achieving predefined pseudoattitude angles ϕ_d

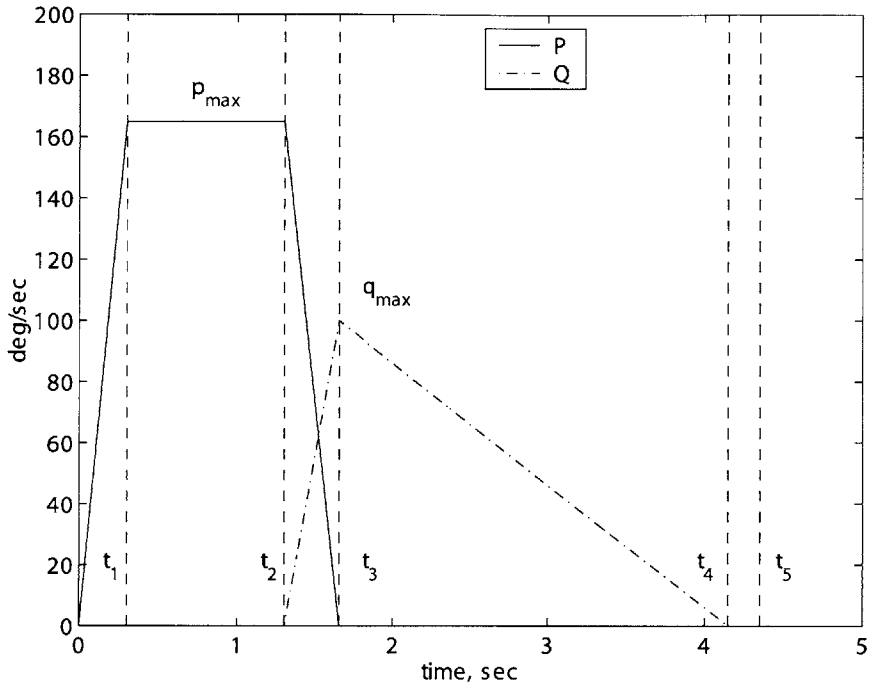

Figure 4-14: Pitch and roll rate reference trajectories for split-S maneuver

and θ_d.

$$t_2 \quad : \quad \int_0^{t_2} pdt = \phi_d \tag{4.10}$$

$$t_4 \quad : \quad \int_{t_3}^{t_4} qdt = \theta_d \tag{4.11}$$

The collective pitch command is given by Eq. 4.9.

Figure 4-15 shows the recorded state trajectories during an autonomous split-S maneuver. The helicopter dropped 30 meters and reached 18 m/sec forward speed in a dive, which was well predicted in the simulation. The total heading change from the entry until the exit of the maneuver was very close to 180 degrees (within 5 degrees).

4.4.3 Autonomous airshow routine

To demonstrate transitions between trim trajectory modes and maneuvers, and sequencing of the maneuvers, we developed a fully autonomous airshow routine. The helicopter follows a figure-8 route defined by four waypoints (see Figure 4-16 for schematic location of the waypoints), and performs maneuvers and maneuver sequences on pre-defined laps. The waypoint guidance logic is performed with a conventional algorithm which aims to minimize the cross-track error. The logic for the routine was implemented as a state machine, shown in Figure 4-17. When the routine is engaged, the helicopter climbs vertically to 50 meter altitude above ground level (AGL), upon which it transitions into waypoint navigation flight while continuing to climb to 120 meters AGL. When this altitude is reached, the helicopter continues waypoint navigation while holding the altitude. When it is on the way

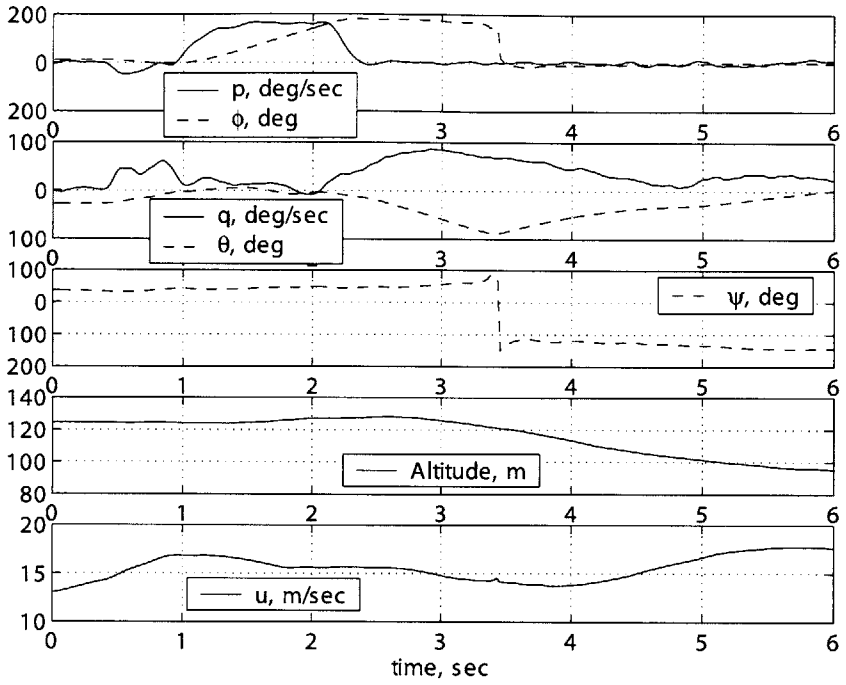

Figure 4-15: Recorded state trajectory during an autonomous split-S

from waypoint 0 to waypoint 1, and certain distance away from waypoint 1 (100 meters), it initiates the axial roll maneuver. Upon the exit from the axial roll, the helicopter heads toward waypoint 2 holding the exit altitude, and continues waypoint navigation until it is again on the way from waypoint 0 to waypoint 1, 100 meters away from reaching it. At this point a split-S is initiated. Upon the exit from split-S the helicopter heads toward waypoint 3, then 0, and performs a hammerhead maneuver at roughly the same region of the sky where previous maneuvers were performed. After the hammerhead maneuver the helicopter continues waypoint navigation starting from waypoint 3, while climbing back to 120 meters AGL. Upon reaching the target altitude, the helicopter continues waypoint navigation in altitude hold until it is back in the region selected for maneuver entrance, and initiates a split-S. At the end of the two-second settling phase of the split-S maneuver, the helicopter immediately performs a hammerhead. After this, the helicopter goes back to the point where the airshow sequence was engaged, and transitions to hover, waiting for further commands.

Figure 4-18 shows flight data for the split-S - hammerhead maneuver sequence. The minimum entry speed for the hammerhead maneuver was defined as 14 m/sec; at the exit of the split-S maneuver the helicopter has sufficient speed to perform it.

4.5 Simplified hybrid model for motion planning

The demonstrated ability to transition from trim trajectory tracking to a maneuver and back, and from one maneuver to another, calls for a simplified state-machine-like repre-

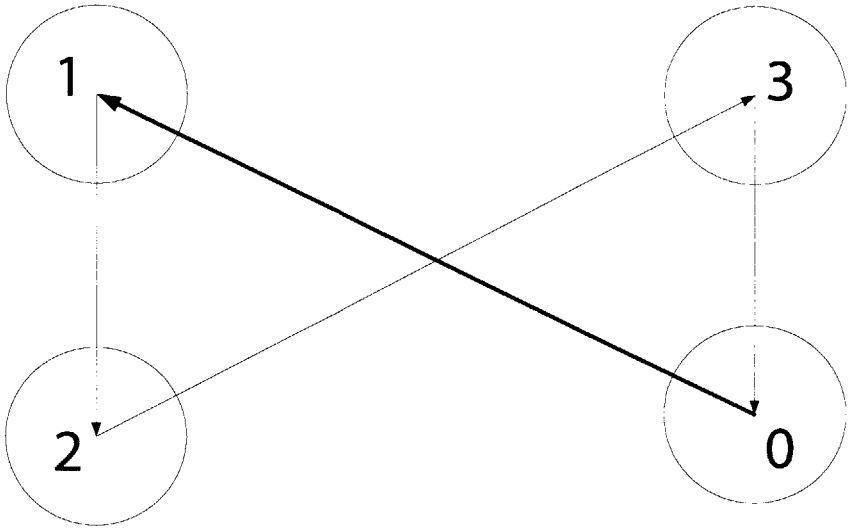

Figure 4-16: Figure-8 waypoint route for the autonomous airshow routine

sentation of helicopter behavior, which can then be used for motion-planning algorithms. Figure 4-19 gives a schematic for such a state machine with three maneuvers.

In trim trajectory phase the helicopter can be described by simplified continuous-time equations that approximate closed-loop dynamics. Assume that the sideslip command is always equal to zero, and for now neglect the tracking error. Furthermore, by design closed-loop response to forward velocity, vertical velocity and turn rate commands exhibit characteristics of second-order systems with small overshoot (5-10 percent). Ideally, the amount of cross-coupling in the closed loop response should be small, let us neglect it to simplify the model. Next, let us approximate these closed loop responses by decoupled first-order systems.

Figure 4-20 shows the comparison of the actual closed-loop response and its first order approximation for forward velocity.

Figure 4-21 shows the comparison for the yaw rate (which is close to turn rate). The yaw rate signal is noisy due to a number of reasons (residual vibration, non-smooth operation of the engine producing torque transients, and coarse quantization of the tail rotor actuator, which leads to a limit-cycle pattern). Nevertheless, one can see that the low-frequency trend is captured well by the first-order approximation.

Finally, Figure 4-22 shows the comparison for the altitude rate. Poor match in the beginning of the segment is due to cross-coupling with the lateral-directional response - the helicopter performed a banking turn. This shows that the approximate model is far from ideal, however it represents a reasonably realistic representation of the dynamics with a very low number of states.

Using the above approximations for the closed-loop dynamics, we can write the following simplified model, which includes heading and 3D position states:

$$\dot{u} = -\frac{1}{\tau_u}u + \frac{1}{\tau_u}u_c \, , \tau_u = 1.3 \text{ sec}$$

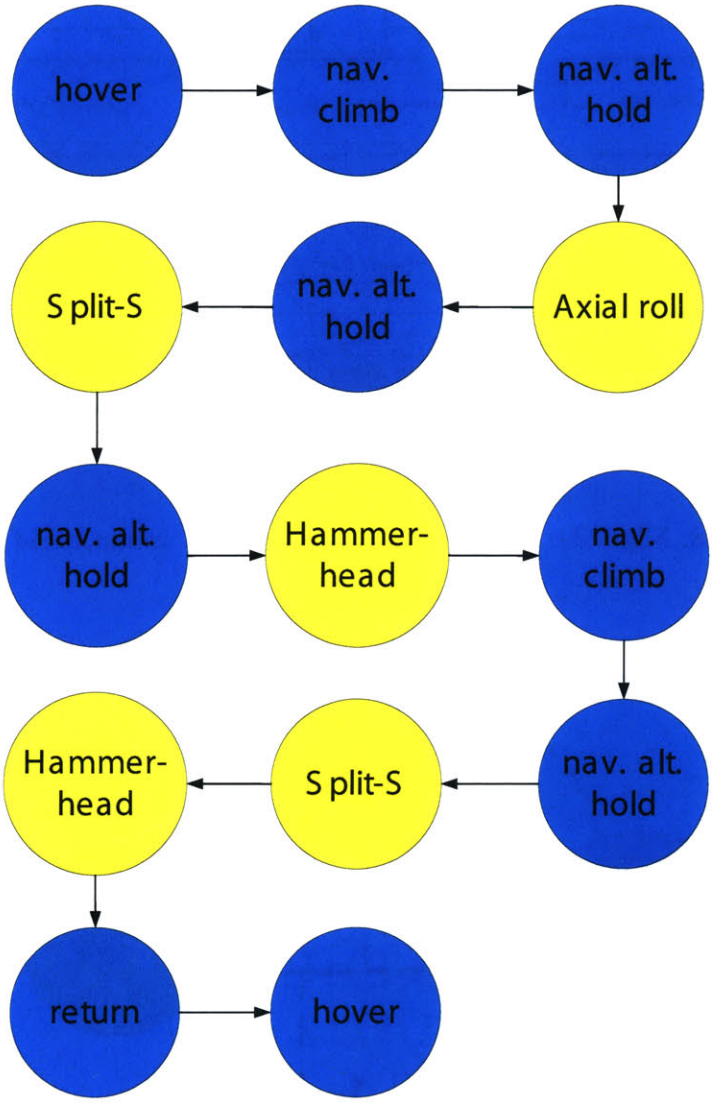

Figure 4-17: A state machine for the autonomous airshow routine

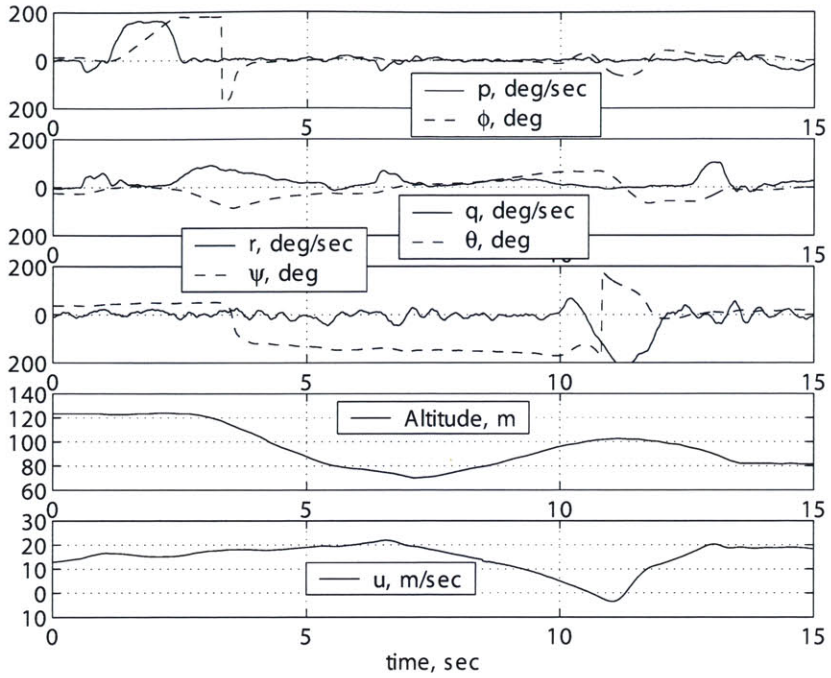

Figure 4-18: Flight data for the autonomous split-S - hammerhead sequence

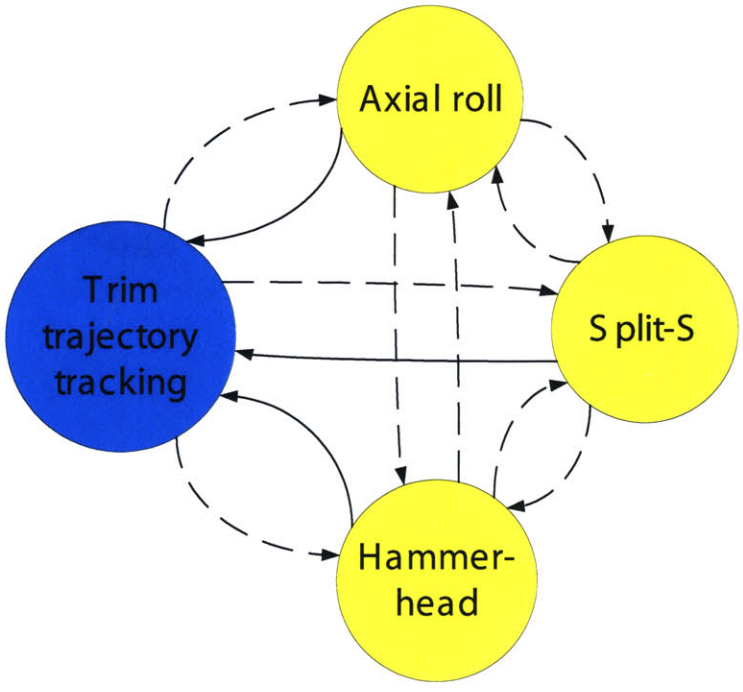

Figure 4-19: A state machine representation of helicopter behavior. Dashed lines are used to indicate that certain transitions may not be allowed depending on vehicle state

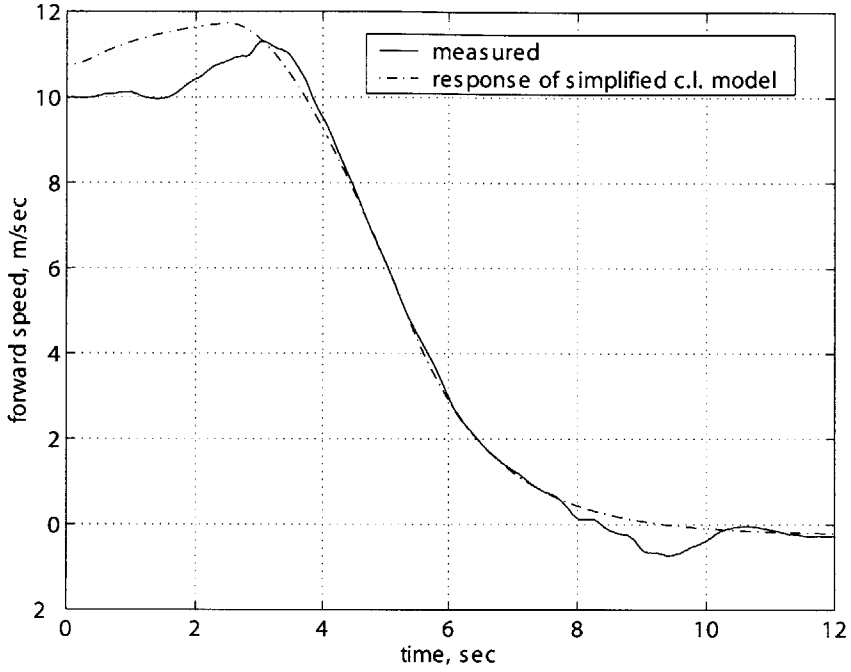

Figure 4-20: First-order approximation of the closed-loop velocity response

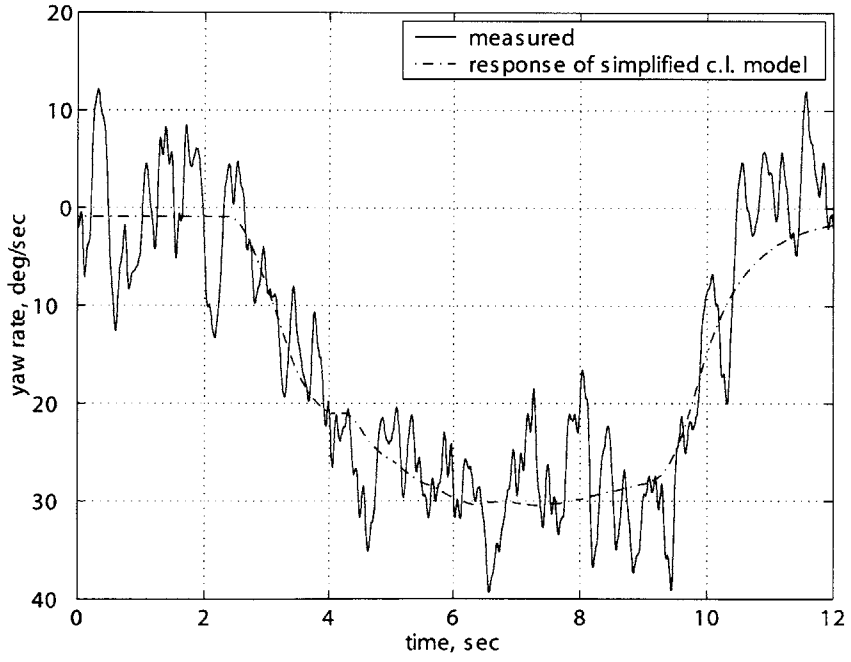

Figure 4-21: First-order approximation of the closed-loop yaw rate response

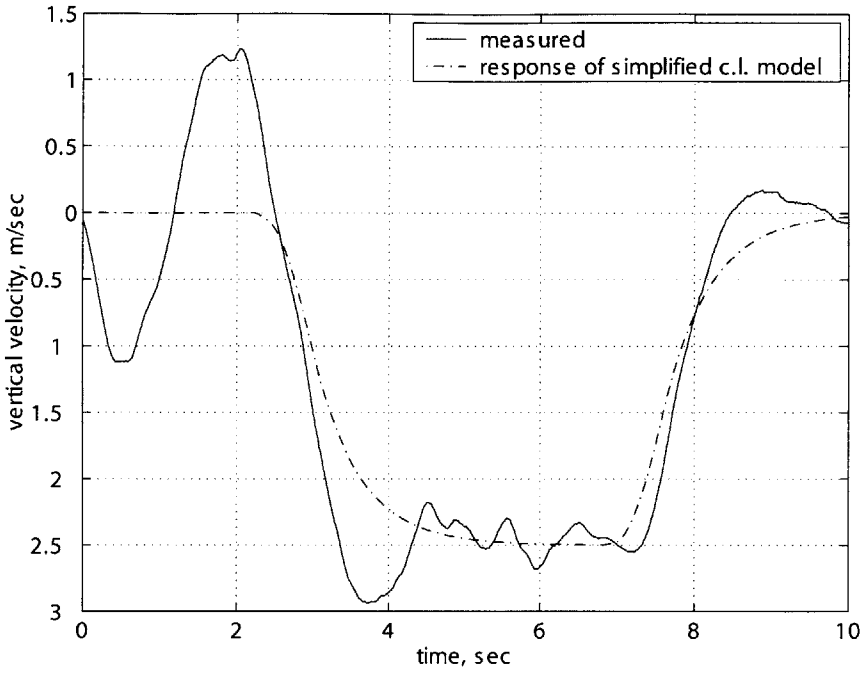

Figure 4-22: First-order approximation of the closed-loop altitude rate response

$$
\begin{aligned}
\dot{r} &= -\frac{1}{\tau_r} r + \frac{1}{\tau_r} r_c \ , \tau_r = 0.7 \text{ sec} \\
\dot{V}^h &= -\frac{1}{\tau_h} V^h + \frac{1}{\tau_h} V_c^h \ , \tau_h = 0.6 \text{ sec} \\
\dot{\psi} &= r \\
\dot{p}_N &= u \cos\psi \\
\dot{p}_E &= u \sin\psi \\
\dot{h} &= V^h
\end{aligned}
$$

A beneficial feature of this representations is that while the open-loop dynamics changes drastically from hover to forward flight, the time constants in the approximations of the closed-loop responses can be assumed constant.

The maneuvers can be represented as discrete changes in the states, which occur in a given time. Monte-Carlo simulations and flight experiments can provide an estimate of the variation of the exit states for a particular maneuver. Since the maneuver execution logic is based on tracking of the rate trajectories, this uncertainty can become large in the presence of strong winds. It is interesting to investigate if there is an alternative control structure, which can ensure a more repeatable change in the states associated with each maneuver in the presence of disturbances.

Chapter 5

Conclusions and future work

5.1 Summary

In this thesis we have developed and experimentally validated a set of tools, which enabled a fully autonomous execution of aerobatic maneuvers with an agile unmanned aerial vehicle, namely a miniature hingeless rotor helicopter. The main contributions are:

- A simplified framework for modeling the dynamics of miniature hingeless rotor helicopters. The resulting model was experimentally shown to provide adequate description of helicopter dynamics in a wide range of flight conditions, including aerobatics.
- An analysis and mathematical modeling of the human pilot's strategies for execution of aerobatic maneuvers, based on recorded flight data. These strategies provided an essential part of the logic for an autonomous execution of the maneuvers.
- A methodology for designing model-based control laws for an autonomous execution of aggressive maneuvers. The resulting control laws were validated with a consistent autonomous execution of several aerobatic maneuvers with a miniature helicopter.
- A simplified hybrid model of helicopter dynamics under feedback control, suitable for use in guidance or motion-planning algorithms.
- An experimental testbed, which includes an avionics package custom-designed for aerobatic flight, and a realistic hardware-in-the-loop simulation.
- A numerically efficient implementation of the state estimation algorithm (Extended Kalman Filter), based on the recently developed attitude error representation, which offers more accurate handling of large initialization errors.

The basis for a simplified modeling framework comes from the fact that the dynamics of miniature helicopters is dominated by the rotor response. A relatively low speed flight envelope, characteristic of these machines, makes modeling still easier. Building upon recent work by Mettler [37], based on frequency-domain analysis of linearized helicopter dynamics around equilibrium conditions, we showed that a first-order flapping dynamics coupled with the rigid body dynamics is sufficient for an accurate description of attitude dynamics in aerobatic flight. Simple analytical methods were used to model aerodynamic forces acting on the fuselage and empennage. The framework relies on direct measurement of the majority of physical parameters, and flight data from a set of simple responses, like step

inputs. Expensive and time consuming system identification or wind-tunnel testing were avoided in the process, nevertheless the resulting model proved adequate for the design of high bandwidth control systems necessary for autonomous aerobatics.

The control laws consist of two separate modes, and a bumpless transfer logic for switching between the modes. First type of controllers guide the helicopter along the equilibrium, or trim trajectories. These controllers are designed by adapting a linear quadratic regulator method to a reduced order helicopter model, appended with integrators on the control variable tracking errors. A novel gain-scheduling scheme, based on discrete switching of gain tables with hysteresis and bumpless transfer logic, was used to accommodate rapid changes in gain values with the scheduling parameter (forward speed). The resulting closed loop control system was experimentally shown to possess the following key features: quick recovery from aerobatic maneuvers to the commanded trim conditions, as well as robustness to gust disturbances and sensor errors. We have also shown that the closed loop dynamics under trim trajectory controllers can be approximated by a set of decoupled first-order models (velocity, turn rate, and altitude command following systems). Motion planning algorithms can use this simplified representation to significantly reduce computation time, while still retaining realistic response and agility.

The second type of controllers were designed specifically for an execution of aerobatic maneuvers. To develop this part of the logic, we studied maneuver execution strategies of R/C pilots with an expertise in aerobatics. Based on the recorded pilot inputs and vehicle state time histories, we came to the following conclusions: the commands and trajectories during maneuvers are highly repeatable, the pilot actions can be closely approximated by piece-wise linear functions, the switching times for which are determined by either neuromuscular response time, or by reaching a certain repeatable attitude. Another key observation comes from the dynamics of the hingeless rotor helicopters: they behave like rate-command systems in response to cyclic inputs. We replaced the open-loop control with tight proportional-integral angular-rate tracking controllers, which feature response times comparable to the neuromuscular response of a well-trained pilot (≈ 0.2 sec). Predictably, the pilot's execution strategies did not change. Due to fast hingeless rotor response to cyclic actuation, and small moments of inertia characteristic of miniature helicopters, the angular rate tracking controllers were designed with a fairly high crossover frequency, which enabled excellent command following and disturbance rejection. Pilot commands during the maneuvers served as a basis for piece-wise linear angular rate command profiles, which were followed during the autonomous execution of the maneuvers.

In order to be able to perform one maneuver after another, we redefine the maneuver as a sequence of three phases: leveling, rate-trajectory following (aerobatic maneuver itself), and settling in the trim-trajectory mode. During the leveling phase the helicopter attitude is brought to within 3 degrees of horizon in pitch and roll. This phase is typically short due to fast attitude response of the helicopter (less than 0.5 seconds), which means that the velocity will not change substantially during this phase. As a result, we can provide common starting conditions for the maneuvers.

Using a library of maneuvers, and a simplified representation of closed-loop dynamics under trim-trajectory controllers, we propose a hybrid model of helicopter dynamics. The helicopter state is described by its forward velocity, turn rate, altitude rate, 3D position and heading. While in trim trajectory mode, these states develop according to simplified dynamic equations, which approximate actual closed-loop responses. Each maneuver represents a discrete change in the states, which occurs in a given time. Naturally, the state change during a maneuver is affected by atmospheric disturbances. The helicopter can

undergo a maneuver from trim trajectory mode or immediately upon exit from another maneuver, provided that the entry conditions are satisfied (i.e. minimum speed and altitude). This model, based on responses determined from flight data, provides a simple and realistic description of agile helicopter dynamics under the feedback control system developed in this thesis.

The work presented in the thesis relied heavily on the experimental setup, which was developed concurrently. A multisensor avionics system was designed and built mostly from off-the-shelf components, with a small number of custom electronic components. A passive suspension system was designed to protect the avionics from the harsh vibration environment onboard the helicopter. The suspension system featured decoupled translational and rotational modes. It was flexible enough to provide excellent attenuation of vibratory inputs, and at the same time stiff enough not to interfere with the helicopter dynamics and sustain loads experienced in aerobatic flight. Flight control software was developed with multiple processes with different priorities, all working under a real-time operating system. Multiple-process design ensured modularity, resulting in rapid development and testing of the software. Finally, the hardware-in-the-loop simulation proved to be an indispensable tool for testing the system in the conditions maximally resembling the real world.

As a byproduct of the work on the avionics system, we developed a fast numerical implementation of the Extended Kalman Filter, based on the attitude error representation, suggested by Frazzoli [12]. While the attitude is normally expressed with a 4-parameter quaternion method, the attitude error is commonly represented by a 3-parameter vector, which represents angular errors around body axes. During the measurement update step, the attitude error vector is estimated, and the quaternion is updated. Most of the quaternion update methods lead to the loss of the unit norm property, and require an explicit normalization step, which leads to additional errors. We suggest using a previously developed quaternion update method, which retains the unit norm, and show that it is consistent with the attitude error representation suggested by Frazzoli [12]. The advantage of the suggested measurement update algorithm compared to the commonly used algorithms will be noticeable for such cases when the attitude initialization errors are large, for example for an in-flight alignment.

The ability to perform autonomous aerobatic maneuvers, developed in this thesis, showed that there is no inherent tradeoff between agility and autonomy. This work is applicable in a number of areas, ranging from urban warfare to filming agile aerial sequences in confined spaces, for example for use in action movies. Nevertheless, a number of research topics arise to improve the current algorithms, and to augment the utility of agile aerial robots. We explore them in the next section.

5.2 Future research

In some applications, where space is severely confined, accurate tracking of 2-dimensional, or even 3-dimensional position during agile maneuvers may be required. Current implementation relies on accurate tracking of angular rate profiles, but can not guarantee position tracking, especially in the presence of strong wind. Repeatable position tracking during agile maneuvers can be also beneficial in filming, since movie sequences frequently require several repetitive takes.

On the instrumentation side, accurate tracking of position in aerobatic flight in the presence of winds will probably require an airspeed sensor, and vanes to measure angles of

attack and sideslip. Such devices are commonly used on full-scale helicopters equipped with avionics systems. Recently light-weight miniature air-data systems were developed for use in UAVs as well.

A much harder challenge comes on the algorithmic side. Since human pilots are unlikely to be able to track a position trajectory (due to lack of accurate position perception as opposed to attitude perception, and bandwidth limitations), an entirely different approach (not inspired by human pilots) will have to invented. Obviously, position tracking will require much higher bandwidth than rate tracking, and any proposed algorithms have to pay special attention to available actuator bandwidth. The mathematical model of aerobatic helicopter dynamics, developed in this thesis, can be used for evaluation of future algorithms.

Fast miniaturization of avionic components makes it possible to perform aerobatic experiments on even smaller platforms, such as miniature helicopters powered by an electric motor. These very light machines will have yet smaller moments of inertia, and with a stiff enough rotorhead will be even more agile. Potentially, such vehicles can be also more useful, being able to penetrate extremely confined environments, and being much quieter than miniature helicopters powered by a piston engine.

It is interesting to explore if the proposed simplified modeling techniques, coupled with the suggested control design methods, are applicable to small full-scale helicopters with hingeless rotors for at least a part of their envelope. It is likely that future unmanned combat rotorcraft will have similar size to modern attack helicopters, and will undoubtedly have to be agile to increase survival rates in hostile environments.

Another research venue is to determine how to use the newly created capability for autonomous agile flight. Should this capability be incorporated into motion planning algorithms, or should a human operator have access to a library of maneuvers from which to choose at his discretion?

Finally, in order to use these vehicles in a cluttered urban environment, an alternative to GPS updates for a state estimator will have to be found. In addition, reliable sensors and algorithms for collision avoidance will have to be developed. A city represents a rich and highly structured environment for visual odometry. In the future, imaging sensors will probably be used for collision avoidance, along with such devices as a sonar or a miniature laser range finder.

In conclusion, we hope that the work presented in this thesis brings us one step closer to creating a truly capable aerial robot, which will have the agility of a falcon, and will be able to use it to accomplish a complex mission.

Bibliography

[1] B. Anderson and J. Moore. *Optimal Control: Linear Quadratic Methods.* Prentice Hall, New York, NY, 1990.

[2] A.R.S. Bramwell. *Bramwell's Helicopter Dynamics.* AIAA, Reston VA, 2001.

[3] A. Bryson. *Control of Aircraft and Spacecraft.* Princeton University Press, Princeton, NJ, 1994.

[4] F. Bullo. *Nonlinear Control of Mechanical Systems: a Riemannian Geometry Approach.* PhD thesis, California Institute of Technology, Pasadena, CA, 1998.

[5] N. Carlson. Fast triangular formulation of the square root filter. *AIAA Journal*, 11(9):1259–1265, September 1973.

[6] R.T. Chen. A simplified rotor system mathematical model for piloted flight dynamics simulation. Technical Memorandum 78575, NASA, 1979.

[7] J. Colbourne, C. Frost, M. Tischler, K. Cheung, D. Hiranaka, and D. Biezad. Control law design and optimization for rotorcraft handling qualities criteria using CONDUIT. Montreal, Quebec, Canada, May 1999. AHS 55th Annual Forum.

[8] R. Deakin. *Model Helicopter Aerobatics.* Traplet Publications, Worcestershire, UK, 2000.

[9] J. Dryfoos and P. Gold. Design and pilot evaluation of the RAH-66 Comanche selectable control modes. Monterey, CA, 1993. American Helicopter Society Specialist Meeting.

[10] edited by C. Harris. *Shock and vibration handbook.* McGraw-Hill, New York, 1996.

[11] E. Feron, M. Brenner, J. Paduano, and A. Turevskiy. Time-frequency analysis for transfer function estimation and application to flutter clearance. *AIAA Journal of Guidance, Control and Dynamics*, 21(3):375–382, 1998.

[12] E. Frazzoli. *Robust Hybrid Control for Autonomous Vehicle Motion Planning.* PhD thesis, Massachusetts Institute of Technology, Cambridge, MA, 2001.

[13] E. Frazzoli, M. Dahleh, and E. Feron. Real-time motion planning for agile autonomous vehicles. *AIAA Journal of Guidance, Control and Dynamics*, 25(1):116–129, 2002.

[14] V. Gavrilets, E. Frazzoli, B. Mettler, M. Piedmonte, and E. Feron. Aggressive maneuvering of small autonomous helicopters: A human-centered approach. *International Journal of Robotics Research*, pages 795–807, October 2001.

[15] V. Gavrilets, M. Martinos, B. Mettler, and E. Feron. Control logic for automated aerobatic flight of miniature helicopter. In *Proceedings of the AIAA Guidance, Navigation, and Control Conference*, Monterey, CA, August 2002.

[16] V. Gavrilets, B. Mettler, and E. Feron. Nonlinear model for a small-size acrobatic helicopter. Number AIAA 2001-4333, Montreal, Canada, August 2001. Proceedings of the AIAA Guidance, Navigation, and Control Conference.

[17] V. Gavrilets, B. Mettler, and E. Feron. Dynamic model for X-Cell 60 helicopter in low advance ratio flight. Technical Report P-2543, MIT Laboratory for Information and Decision Systems, December 2002.

[18] V. Gavrilets, A. Shterenberg, I. Martinos, K. Sprague, M.A. Dahleh, and E. Feron. Avionics system for aggressive maneuvering. *IEEE Aerospace and Electronic Systems Magazine*, pages 38–43, September 2001.

[19] A. Gelb. *Applied Optimal Estimation.* The Analytical Sciences Corporation, 1974.

[20] J. Gibbs. *Scientific papers*, volume 2. Dover, New York, 1961.

[21] F. D. Harris. Articulated rotor blade flapping motion at low advance ratio. *J. Amer. Helicopter Soc.*, January 1972.

[22] R. Heffley and M. Mnich. Minimum-complexity helicopter simulation mathematical model. Technical Report 87-A-7, NASA, Moffett Field, CA, 1987.

[23] Inertial Science, Inc., Newbury Park, CA. *Inertial Measurement Unit ISIS-IMU*, 2000.

[24] S. Kannan and E. Johnson. Adaptive trajectory based control for autonomous helicopters. Irvine, CA, October 2002. Proceedings of the 21st Digital Avionics Systems Conference.

[25] Frank Kolnick. *QNX 4 Real-Time Operating System.* Basis Computer Systems, Canada, 1998.

[26] A.M. Kuethe and C. Y. Chow. *Foundations of Aerodynamics.* Wiley and Sons, New York, 1986.

[27] M. LaCivita, T. Kanade, G. Papageorgiou, and W. Messner. Design and flight testing of a high-bandwidth h-infinity loop shaping controller for a robotic helicopter. Monterey, CA, August 2002. Proceedings of the AIAA Guidance, Navigation, and Control Conference.

[28] M. LaCivita, W. Messner, and T. Kanade. Modeling of small-scale helicopters with integrated first-principles and integrated system identification techniques. Montreal, Canada, June 2002. Presented at 58th Forum of American Helicopter Society.

[29] E. Lefferts, F. Markley, and M. Shuster. Kalman filtering for spacecraft attitude determination. *AIAA Journal of Guidance, Control and Dynamics*, 5(5):417–429, 1982.

[30] J. G. Leishman. *Principles of helicopter aerodynamics.* Cambridge University Press, New York, 2000.

[31] L. Ljung. *System Identification: Theory for the User.* Prentice Hall, Upper Saddle River, N.J., 1999.

[32] L. Lublin and M. Athans. Linear quadratic regulator control. In W. Levine, editor, *The Control Handbook.* IEEE Press, New York, NY, 1996.

[33] F. Markley. Attitude error representations for kalman filtering. *AIAA Journal of Guidance, Control and Dynamics*, 26(2):311–317, March 2003.

[34] P. Maybeck. *Stochastic Models, Estimation and Control.* Academic Press, New York, NY, 1979.

[35] M. McConley. Draper small autonomous aerial vehicle dynamic model. Technical Report E41-98-091, Draper Laboratory, August 1998.

[36] M. McConley, B. Appleby, M. Dahleh, and E. Feron. A computationally efficient Lyapunov-based scheduling procedure for control of nonlinear systems with stability guarantees. *IEEE Transactions on Automatic Control*, January 2000.

[37] B. Mettler. *Identification, Modeling and Characteristics of Miniature Rotorcraft.* Kluver Academic Publishers, Boston, MA, 2002.

[38] B. Mettler, V. Gavrilets, E. Feron, and T. Kanade. Dynamic compensation for high-bandwidth control of small-scale helicopter. San Francisco, CA, January 2002. American Helicopter Society Specialist Meeting.

[39] B. Mettler, M. Tischler, T. Kanade, and W. Messner. Attitude control optimization for a small-scale unmanned helicopter. Denver, CO, August 2000. AIAA Guidance, Navigation and Control Conference.

[40] B. Mettler, M.B. Tischler, and T. Kanade. System identification modeling of a small-scale unmanned rotorcraft for control design. *Journal of the American Helicopter Society*, 47(1):50–63, January 2002.

[41] Miniature Aircraft USA, Orlando, FLa. *X-Cell .60 graphite SE Helicopter Kit (Special Edition) Instruction Manual*, 1999.

[42] J. Murphy, H. Walker, and A. Kaufman. An integrated low altitude flight control system for helicopters. Number 86, Konstanz, Germany, June 1971. AGARD Conference Proceedings.

[43] NASA Ames Research Center, Moffet Field, CA. *Comprehensive Identification from Frequency Responses: an interactive facility for system identification and verification*, 2000.

[44] G.D. Padfield. *Helicopter Flight Dynamics: The Theory and Application of Flying Qualities and Simulation Modeling.* AIAA Education Series, Reston, VA, 1996.

[45] R. Rogers. *Applied mathematics in integrated navigation systems.* AIAA Education Series, Reston, VA, 2000.

[46] J. M. Rolfe and K. J. Staples. *Flight Simulation.* Cambridge University Press, UK, 1986.

[47] K. Sprague, V. Gavrilets, D. Dugail, B. Mettler, and E. Feron. Design and applications of an avionics system for a miniature acrobatic helicopter. Daytona Beach, FL, 2001. AIAA Digital Avionics Systems Conference.

[48] B. Stevens and F. Lewis. *Aircraft Control and Simulation.* Wiley, New York, NY, 1992.

[49] T. D. Talbot, B. E. Tingling, W. A. Decker, and R.T. Chen. A mathematical model of a single main rotor helicopter for piloted simulation. Technical Memorandum 84281, NASA, 1982.

[50] M. Tischler, editor. *Advances in Aircraft Flight Control.* Taylor and Francis, Cornwall, England, 1996.

[51] D. Titterton and J. Weston. *Strapdown Inertial Navigation Technology.* Lavenham Press, Lavenham, UK, 1997.

[52] W. von Grunhagen, G. Bouwer, H.-J. Pausder, F. Henchel, and J. Kaletka. A high bandwidth control system for the helicopter in-flight simulator ATTHeS - modelling, performance and applications. In M. Tischler, editor, *Advances in Aircraft Flight Control.* Taylor and Francis, Cornwall, England, 1996.